8-2014

Atomic and Molecular Laser-induced Breakdown Spectroscopy Above a Titanium Target

Alexander Charles Woods
University of Tennessee - Knoxville, awoods9@vols.utk.edu

To the Graduate Council:

I am submitting herewith a dissertation written by Alexander Charles Woods entitled "Atomic and Molecular Laser-induced Breakdown Spectroscopy Above a Titanium Target." I have examined the final electronic copy of this dissertation for form and content and recommend that it be accepted in partial fulfillment of the requirements for the degree of Doctor of Philosophy, with a major in Physics.

Christian G. Parigger, Major Professor

We have read this dissertation and recommend its acceptance:

Lloyd M. Davis, Horace W. Crater, Trevor M. Moeller

Accepted for the Council:

Carolyn R. Hodges

Vice Provost and Dean of the Graduate School

(Original signatures are on file with official student records.)

8-2014

Atomic and Molecular Laser-induced Breakdown Spectroscopy Above a Titanium Target

Alexander Charles Woods
University of Tennessee - Knoxville, awoods9@vols.utk.edu

To the Graduate Council:

I am submitting herewith a dissertation written by Alexander Charles Woods entitled "Atomic and Molecular Laser-induced Breakdown Spectroscopy Above a Titanium Target." I have examined the final electronic copy of this dissertation for form and content and recommend that it be accepted in partial fulfillment of the requirements for the degree of Doctor of Philosophy, with a major in Physics.

Christian G. Parigger, Major Professor

We have read this dissertation and recommend its acceptance:

Lloyd M. Davis, Horace W. Crater, Trevor M. Moeller

Accepted for the Council:
Carolyn R. Hodges

Vice Provost and Dean of the Graduate School

(Original signatures are on file with official student records.)

Atomic and Molecular Laser-induced Breakdown Spectroscopy Above a Titanium Target

A Dissertation Presented for the

Doctor of Philosophy

Degree

The University of Tennessee, Knoxville

Alexander Charles Woods

August 2014

Acknowledgements

I would like to thank my committee for their continued support and encouragement: Dr. Christian Parigger, my committee chair; Dr. Horace Crater; Dr. Lloyd Davis; and Dr. Trevor Moeller. I offer my sincere appreciation for the learning opportunities you provided me.

Special thanks are due to my advisor, Chris Parigger. Without your guidance and enthusiasm none of this would have been possible.

Additionally, I would like to thank Jim Hornkohl. Our Tuesday meetings and the extra help you provided were instrumental in my understanding of the physics and computations that make this research possible.

I would also like to thank my classmates, David Surmick, Michael Witte, and Lauren Swafford. You each have been wonderful additions to the lab, and your contributions both expedited and enhanced this research.

Finally, I would like to thank my parents, Betsy and Larry Woods; my fiancée, Bailey; along with her parents, Glenda and Dennis Berry. Each of you have provided tremendous love and support, not to mention food, which has sustained me throughout my studies.

There are only two ways to live your life. One is as though nothing is a miracle. The other is as though everything is a miracle.

–Albert Einstein

Abstract

The goal of this research is to use optical emission spectroscopy to investigate the processes occurring subsequent to laser ablation of a titanium sample. Laser-induced breakdown spectroscopy provides a procedure for atomic and molecular identification for particular constituents of a laser-induced plasma. Atomic spectral line shapes provide a diagnostic tool for characterizing laser induced plasma, particularly within the first hundreds of nanoseconds. Molecular recombination and/or excitation of selected molecules can lead to simultaneous detection of atomic and molecular species via spectral analysis. Nonlinear fitting of synthetic molecular spectra, calculated via diatomic quantum theory, provides tools for identification, temperature measurement, and further analysis of the diatomic molecules present. By computing accurate line strength values for the TiO molecule, synthetic spectra for the TiO transitions are used to analyze plasma emissions at delay times within the first hundreds of microseconds. In obtaining and analyzing results, numerical methods are implemented. Specifically, use of a Monte-Carlo simulation is studied, as a tool for error analysis. The resulting analysis characterizes the temperature and electron density as a function of time within the first hundreds of nanoseconds. Investigations of TiO spectral transitions along the height of the ablation plume, at time delays of tens of microseconds, reveal two distinct luminescent regions within the plasma with starkly different temperatures.

Table of Contents

List of Tables

List of Figures

Chapter 1

Introduction

1.1 Laser Induced Breakdown Spectroscopy

The analytical approach of laser-induced breakdown spectroscopy (LIBS) dates back to 1960 and the invention of the first laser by Maimon (84). Published accounts of laser ablation appeared in 1962, first by F. Beech and L. Cross (11) and shortly thereafter by W.I. Linlor (74). Then in 1963, the first of many experiments involving the measurement of laser-induced photoemission of electrons was conducted by Muray (91). Of particular interest is the work of J.A. Howe, who demonstrated the capability to measure the temperature of ablation plumes via vibrationally and rotationally resolved molecular emission bands (57).

A notable early experimental application of plasma diagnostics using LIBS was performed in gaseous H_2 (79; 80). Various groups took advantage of the relatively large Stark broadening of the hydrogen atom to determine electron number density (50; 157; 32; 4; 9; 143). From these early investigations to more recent studies, plasma diagnostics using LIBS has made use of Stark broadening tables to infer micro-plasma parameters from spectral line shapes. Using the impact approximation and the assumption of no coupling between ion and electron microfields (7; 6), Griem compiled the earliest Stark broadening tables (43; 44). Gigosos, Cardeñoso, and

Gonzáles later published Stark broadening tables by allowing ion dynamics and some couplings between the ion and electron microfields (37; 38). Most recently, Oks generated Stark broadening tables using a more accurate analytical treatment of ion dynamics and incorporated all possible couplings between microfields (93; 95).

Aided not only by advances in theory but as well as by the advances in computational analysis, LIBS has demonstrated the capability to distinguish the principal components, which make up complex materials (88). Thus, LIBS has become a powerful tool in analytical chemistry, and in general, the focus of ongoing research has shifted from a fundamental physics perspective to one of remote detection applications. As a method of elemental component analysis, LIBS is especially attractive because it may be used to analyze solids, liquids, and gases with little to no sample preparation. This particular advantage has allowed LIBS to infiltrate various disciplines normally not associated with laser technology. These include the analysis of geological samples, historical artifacts, explosive materials, and crime scene investigation.

However, the success and growth of these and future applications require a deeper fundamental understanding of the processes occurring and what is being observed. To this extent much of the ongoing fundamental research utilizing LIBS, seeks to observe and analyze specific atomic and molecular species present in the laser-induced plasma (101; 99; 105; 55; 31). By closely examining the properties of spectra from specific atoms and molecules along the plasma, as it evolves in time, a more complete description of the characteristic processes going on throughout the plasma can be obtained. Such resulting information would enlighten us as to the time frame of when molecular recombination overcomes electron collisions as the dominant process occurring in the plasma. In order to successfully accomplish this, diatomic quantum theory must be utilized in computing synthetic spectra. The experimentally collected spectra is then fit with the computed spectra.

1.1.1 Characteristic Experiments

One strength of LIBS as an experimental technique is the simplicity of the required equipment. While charged particle detection and laser excitation techniques provide arguably the best results for stand-off analysis of laser-induced plasma (LIP), optical emission spectroscopy provides the most available technique to investigate the brightest zone of the LIP. Because optical emission spectroscopy relies on the intrinsic light emission of the LIP, no additional excitation source or intrusive system is necessary. This simplicity lends LIBS systems for remote detection and automation (65; 22; 131).

The average LIBS apparatus consists of Nd:YAG laser serving as the excitation source, a focusing lens for the laser beam, and a spectrograph equipped with a detector (116). The Nd:YAG laser is most commonly operated with nominal 10 nanosecond bursts at its fundamental wavelength of 1064 nm. Assuming a near TEM_{00} Gaussian mode, with an energy around 100 mJ per pulse, f/10 focusing will provide on the order of 10,000 GW/cm^2 at the minimum beam waist. At such intensities in gases at atmospheric pressures, electron excitation temperatures can reach on the order of 100,000 K with electron densities on the order of 20^{25} m^{-3}.

While the Nd:YAG laser is well regarded as the standard for LIBS experiments, several other lasers have been historically used as excitation sources (23). Recent investigations in LIBS have shown preference to dual- and multi-pulse laser excitations (144; 62; 21; 82; 86). Multi-pulse excitations serve to increase the plasma volume by effectively reheating the plasma. This can provide a signal enhancement providing a factor of 10 to 100 times the detection limits of a single pulsed excitation LIBS experiment (120).

Recent work at UTSI has investigated the hydrogen Balmer series subsequent to laser-induced optical breakdown (LIOB) of an expanding methane flow, as pictured in Figure 1.1 (101; 99; 105; 94; 98; 162; 169; 107; 110; 113). In previous experiments (106), a pressure cell was filled with gaseous hydrogen to a pressure of 810 $\pm$ 25

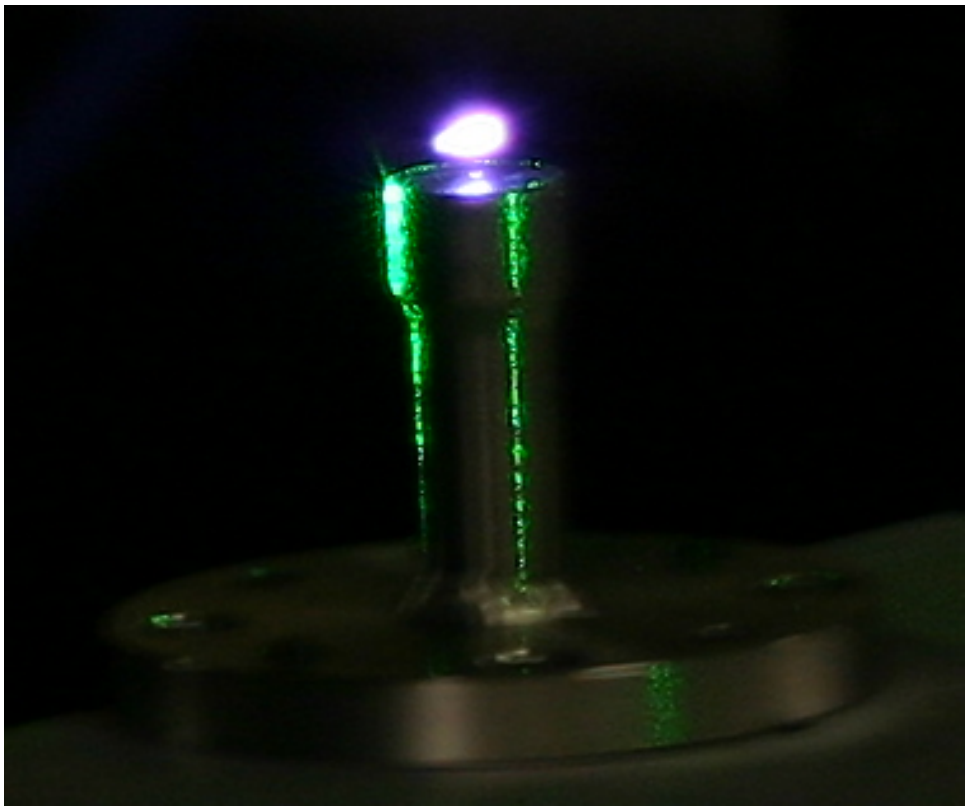

Figure 1.1: Laser-induced optical breakdown above nozzle used for expanding methane flow.

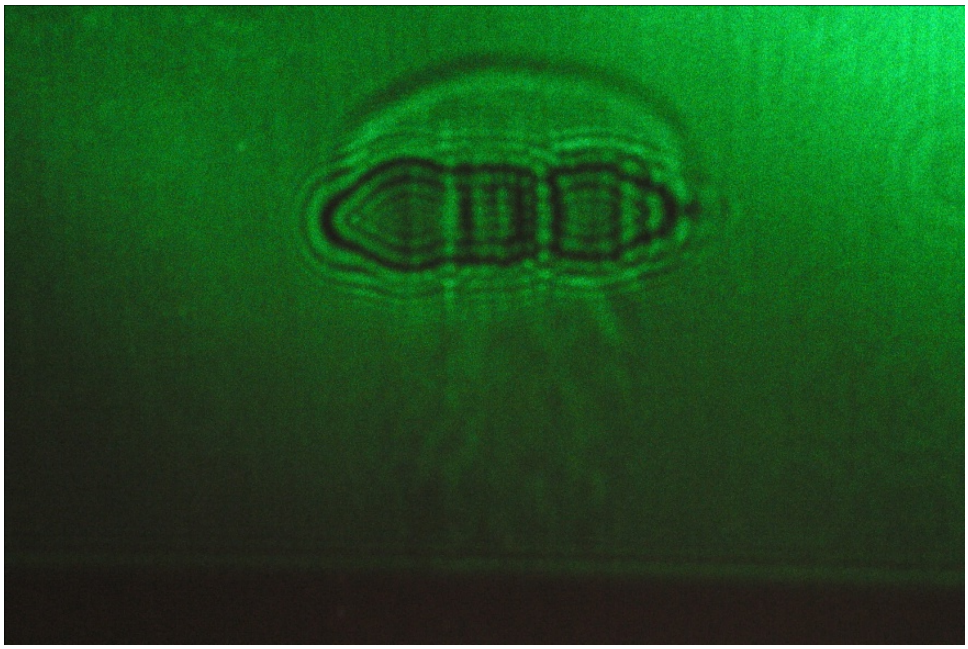

Figure 1.2: Shadow graph of laser-induced plasma of an expanding methane flow (142).

Torr (1.07×10^5 Pa) and later to 1010 ± 25 Torr (1.35×10^5 Pa). After the cell was evacuated by use of a diffusion pump, a Continuum YG680S-10 Nd:YAG with 150 mJ energy per pulse and 7.5 ns pulse duration was focused to approximately 1,400 GW/cm^2 in the gas. This process created the micro-plasma, which was to be analyzed. In addition, a Coherent Infinity 40-100 Nd:YAG laser with 50 mJ and 300 mJ pulse energy and 3.5 ns pulse width was focused in laboratory air to an irradiance of typically 10,000 GW/cm^2. By using 308 nm pulses from a 6 ns pulsed excimer laser, shadowgraph images could then be taken of the laser-induced plasma, as seen in Fig. 1.2 (142). "The scanning spectrometer (Jobin-Yvon 0.64 m Czerny-Turner) and photomultiplier (RCA C41034A) arrangement, together with the Boxcar (EG&G Model 4402) allows one to record the broad hydrogen Balmer-alpha early in the plasma decay, with a spectral resolution of 0.02-nm, and with a 2 ns temporal resolution. The alternative arrangement includes an intensified diode array detector (Princeton Applied Research Corporation EG&G Model 1530-CUV) to record H_α, H_β, or H_γ emission lines with a 6 ns gate for the intensifier. Synchronization is usually

achieved with several delay generators (Stanford Research Systems Model DG535)." (105)

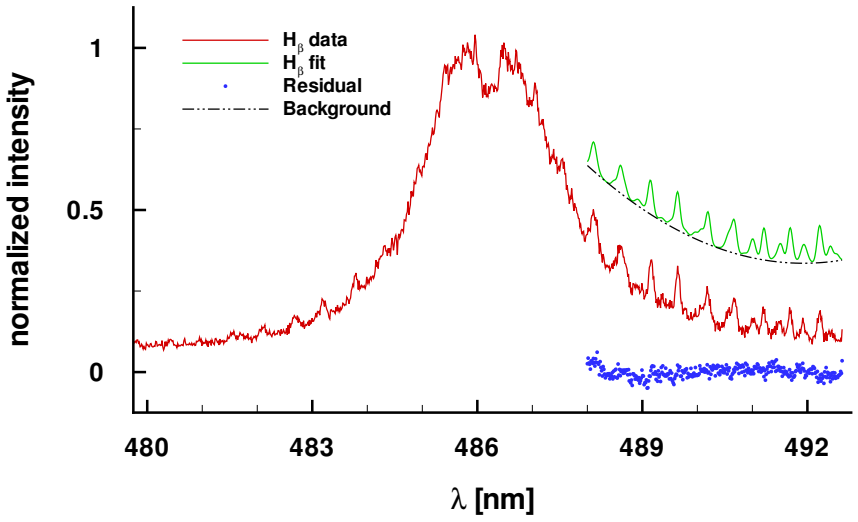

Figure 1.3: Measured H_β and fitted C_2 Swan Band emissions. $\Delta\tau = 2.0$ μs, $p = 6.5 \times 10^5$ Pa. Fitted molecular emission temperature: 0.54×10^4 K, electron excitation temperature: 1.3×10^4 K (110).

In a similar experiment also conducted at the UTSI Center for Laser Applications (101; 99), a laser beam of 8 ns pulse duration and typically 75 mJ energy per pulse is focused into the expanding plume of a pulsed methane gas flow approximately 2 mm above the 2 mm exit aperture of a custom-built nozzle. The resulting irradiance was typically 700 GW/cm^2. The beam consists of 1064 nm infrared radiation from a Q-switched Continuum YG680S-10 Nd:YAG laser, operated at 10 Hz. The data acquisition utilized intensified detection equipment coupled to a spectrometer. Specifically, this consisted of an "intensified EG&G linear diode array, UV-enhanced detector, Model 1460 Princeton Applied Research detector/controller optical multichannel analyzer. A 1/2 meter Model 500 SpectraPro Acton Research Corporation spectrometer was used with a 2400-groves/mm grating, blazed for 240

nm."(101) Spectral resolutions of 0.12 nm, 0.11 nm, and 0.07 nm were achieved for H_α, H_β, and H_γ, respectively, by setting the entrance slit to 125 μm.

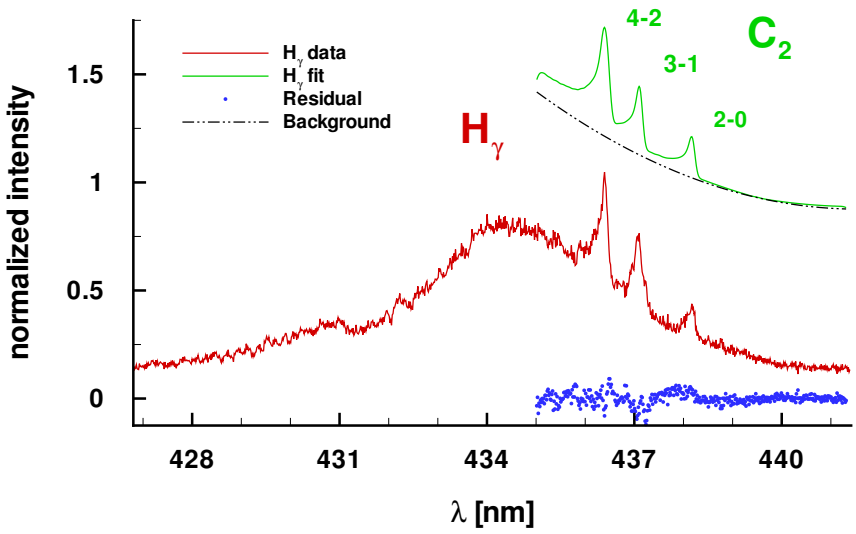

Figure 1.4: Measured H_γ and C_2 Swan Band emissions, $\Delta\tau = 2.0$ μs, $p = 6.5 \times 10^5$ Pa. Fitted molecular emission temperature: 0.48×10^4 K, electron excitation temperature: 1.3×10^4 K (110).

These two techniques allowed for the spectral profiles of hydrogen Balmer series to be collected. Temperature and electron density may be inferred from analyzing the intensity and shape of the profiles. This is accomplished by using the area of the H_α, H_β, and H_γ profiles to construct Boltzmann plots (39; 102). In these calculations use of the full-width at half-maximum is preferred to the full-width at half-area (99). However, the inferred temperatures, T_e, are slightly skewed here by significant background radiation and high electron density, N_e, early in the plasma decay, along with overlapping molecular spectra later in the plasma decay. Nearly identical results were obtained for both the 2.7×10^5 Pa and 6.5×10^5 Pa gas pressures for the expanding methane flow. For H_α and H_β, the inferred T_e range from 10,000 K (time delay 2.1 μs) to 20,000 K (time delay of 0.4 μs), while the inferred N_e range from 10^{19} cm^{-3} (H_α) to 6×10^{16} cm^{-3}(H_β).

In the analysis of collected spectra resulting from this experiment, C_2 molecular Swan bands are seen superposed to the H_β and H_γ profiles (110; 107). Figures 1.3 and 1.4 display experimental results for H_β and H_γ atomic lines along with fitted molecular spectra. This specific molecular spectra accounts for much of the background previously mentioned. Using computed line-strength tables for the C_2 Swan band system, synthetic spectra for the diatomic carbon molecule was then fit to the data using a Nelder-Mead algorithm (92). The result of this fitting allowed for the determination of the temperature of both the hydrogen species and the C_2 in the plasma. Since the majority of information gained from these types of experiments relies on the matching of synthetic spectra with experimental data, it is necessary to elaborate on the generation of computed spectra.

1.2 Diatomic Spectral Predictions

While quantities like Einstein coefficients, oscillator strength, and cross section are very familiar, it is the line-strength which carries great significance in calculating spectra. The line strength is significant because it is the term in which some of the more familiar terms are defined (53; 55). One such example being the Einstein A coefficient,

$$A_{ul} = \frac{2\omega_{ul}^3}{3\varepsilon_0 h c^3 g_u} S_{ul}, \tag{1.1}$$

where ω_{ul} is the transition frequency ($\omega_{ul} = 2\pi\nu_{ul}$), g_u is the upper level degeneracy, h is Planck's constant, c is the speed of light, ε_0 is the vacuum permittivity, and S_{ul} is the line-strength defined as

$$S_{ul} = \sum_u \sum_l |\langle u|T_\kappa^{(q)}|l\rangle|^2. \tag{1.2}$$

Here, $T_\kappa^{(q)}$ is the κ^{th} component of the irreducible tensor of order q responsible for the transition, and the summations account for all upper (u) and lower (l) states that

produce that particular spectral line. Computed spectra consists of line-strength files. These line-strengths are defined by the unitless Hönl-London factors (104),

$$S(J',J) = \frac{1}{2J+1}\left|\sum_{a'}\sum_{a}\langle nvJM|a\,\rangle\,\langle J\Omega q\kappa|J'\Omega'\rangle\,\langle a'|n'v'J'M'\rangle\right|^2 \delta_{S'S}\delta_{\Sigma'\,\Sigma}, \quad (1.3)$$

and the electronic-vibration strength,

$$S(n'v',nv) = \sum_{\kappa=-q}^{q}\left|\langle nv|\hat{T}_{\kappa}^{(q)}|n'v\rangle\right|^2, \quad (1.4)$$

which has units of line-strength. In the above equation providing the Hönl-London factors, ν represents the vibrational quantum number, J the total angular momentum, M the magnetic quantum number for the laboratory z-component of the total angular momentum, Ω is for the z'-component of the total angular momentum, n represents all other necessary quantum numbers, S the spin, Σ the spin for the z'-component, and a represents the Hund's case (a) basis. Now, the electronic-vibrational strength, $S(n'v',nv)$, consists of the electronic transition moment. To compute this, it becomes necessary to separate the electronic and nuclear vibrational and rotational elements. In other words, we make the Born-Oppenheimer approximation,

$$\langle n'v'|\hat{T}_{\kappa}^{(q)}|nv\rangle \approx \langle n'|\hat{T}_{\kappa}^{q}|n\rangle\,\langle v'|v\rangle = \mathcal{R}_{n'\,n}(\mathbf{r})\,\langle v'|v\rangle. \quad (1.5)$$

This allows for the electronic transition moment, $\mathcal{R}_{n'\,n}(\mathbf{r})$, to become separated from the overlap integral, $\langle v'|v\rangle$. In order to analytically calculate the electronic-vibrational strength for each allowed transition, the electronic transition moment is expanded using a Taylor's series,

$$\mathcal{R}_{n'\,n}(\mathbf{r}) = a_0 + a_1\mathbf{r} + a_2\mathbf{r}^2 + \ldots \quad (1.6)$$

Adding the Franck-Condon factors,

$$q(v', v) = \langle v'|v\rangle^2 = \left| \int_0^\infty \psi_{v'}(\mathbf{r})\, \psi_v(\mathbf{r})\, d\mathbf{r} \right|^2, \tag{1.7}$$

and r-centroids,

$$\bar{\mathbf{r}}^{(k)}(v', v) = \frac{\langle v'|\mathbf{r}^k|v\rangle}{\langle v'|v\rangle} = \int_0^\infty \psi_{v'}(\mathbf{r})\, \mathbf{r}^k\, \psi_v(\mathbf{r})\, d\mathbf{r} \Big/ \int_0^\infty \psi_{v'}(\mathbf{r})\, \psi_v(\mathbf{r})\, d\mathbf{r}. \tag{1.8}$$

the electronic-vibrational strength becomes

$$S(n'v', nv) = \left[a_0 + a_1 \bar{\mathbf{r}}^{(1)}(v', v) + a_2 \bar{\mathbf{r}}^{(2)}(v', v) \ldots\right]^2 q(v', v). \tag{1.9}$$

Of course, the line-strength file is not the only information needed to calculate a spectrum. One must also assume a model for the population density of states. To this end, a thermal distribution of states is appropriate. In terms of the wavenumber ($\tilde{\nu}_{u\ell} = F_u - F_\ell$) and with line strength in units of $e_{\text{esu}}^2\, a_0^2$, the equation for free spontaneous emission reads (104)

$$I_{u\ell} = \frac{64\pi^4\, e_{\text{esu}}^2\, a_0^2\, c\, N_0}{3\, Q}\, \tilde{\nu}_{u\ell}^4\, e^{-hcF_u/k_BT}\, S_{u\ell}, \tag{1.10}$$

where e_{esu} is the electronic charge in electrostatic units and a_0 is the Bohr radius in cm. Thus, accurate spectrum predictions require, at least, a temperature for Boltzmann factors and may also include spectral resolution, electron density, reaction rates, collision rates, and pressure. Figure 1.5 shows a computed C_2 spectrum for a temperature of 3000 K.

1.2.1 Commercially Available Predictions

Programs are available, which compute synthetic spectra for popular diatomic molecules, such as C_2, N_2, NO, and others. One such program, SPECAIR, allows one to evaluate spectra for different translational, electronic, vibrational and rotational

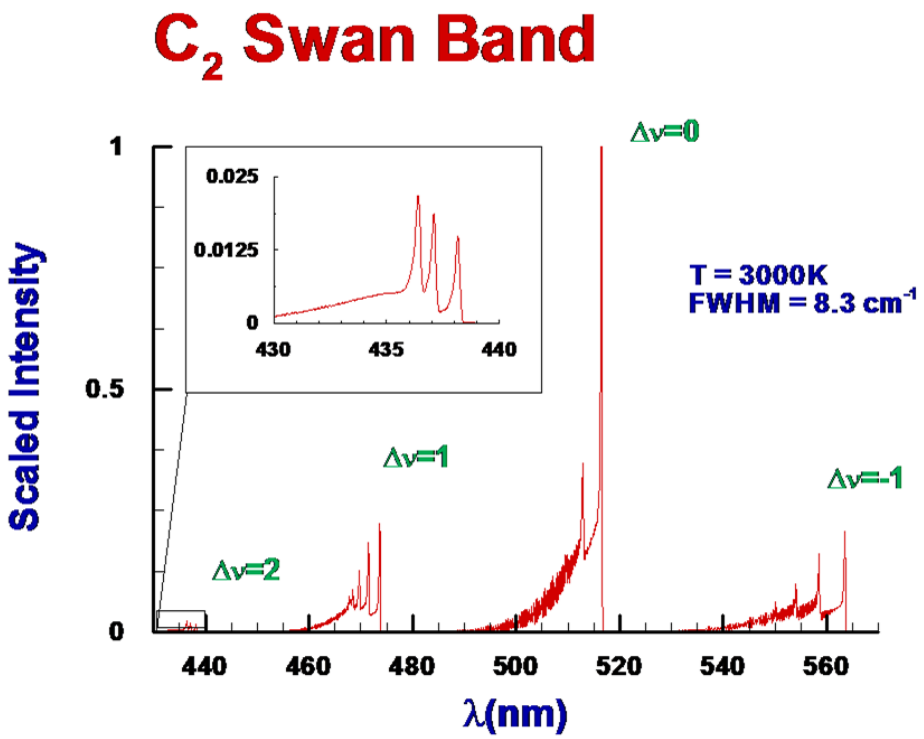

Figure 1.5: Synthetic emission spectrum progression of C_2 Swan band for a spectral resolution of FWHM = 8.3 cm^{-1} and for T = 3000 K.

temperatures individually (72). The code utilizes Boltzmann distribution factors at the electronic, vibrational, and rotational temperature to determine the population of the internal energy levels. It also allows one to evaluate effects of absorption by room air between the emitting gas or plasma and the detector. However, in comparing the stick spectrum computed with SPECAIR for C_2 with our line-strength file for C_2, subtle differences become apparent (110). Figure 1.6 provides a comparison of SPECAIR and line strength file predictions. These subtle differences usually result in noticeable differences in computing synthetic spectra, especially in the investigation of superposition spectra. Despite this, SPECAIR remains useful in gaining a quick overview of a molecule's spectrum for various parameters at lower resolution.

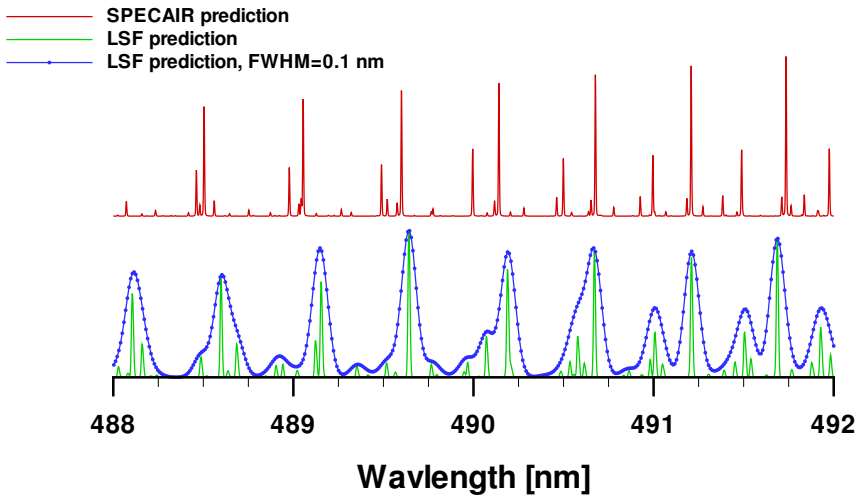

Figure 1.6: Line-positions computed using SPECAIR (top) and line-strength files for C_2 (bottom) for an equilibrium temperature of T = 5000 K. The broadened profile (bottom) is computed for FWHM = 0.1 nm (110).

1.3 Diagnostics Utilizing Diatomic Emissions

1.3.1 Aluminum Monoxide

Similar computations regarding the molecular spectra of aluminum monoxide (AlO) have also been performed at UTSI (104). These calculations have resulted in detailed synthetic spectra for the AlO molecule (31), as demonstrated by Figure 1.7. A recent collaboration with Fire and Aerosol Sciences at Sandia National Laboratory studied the presence and temperature of AlO as a function of height along a vertical flame plume (49; 98; 169; 162; 107; 111; 149; 109; 114).

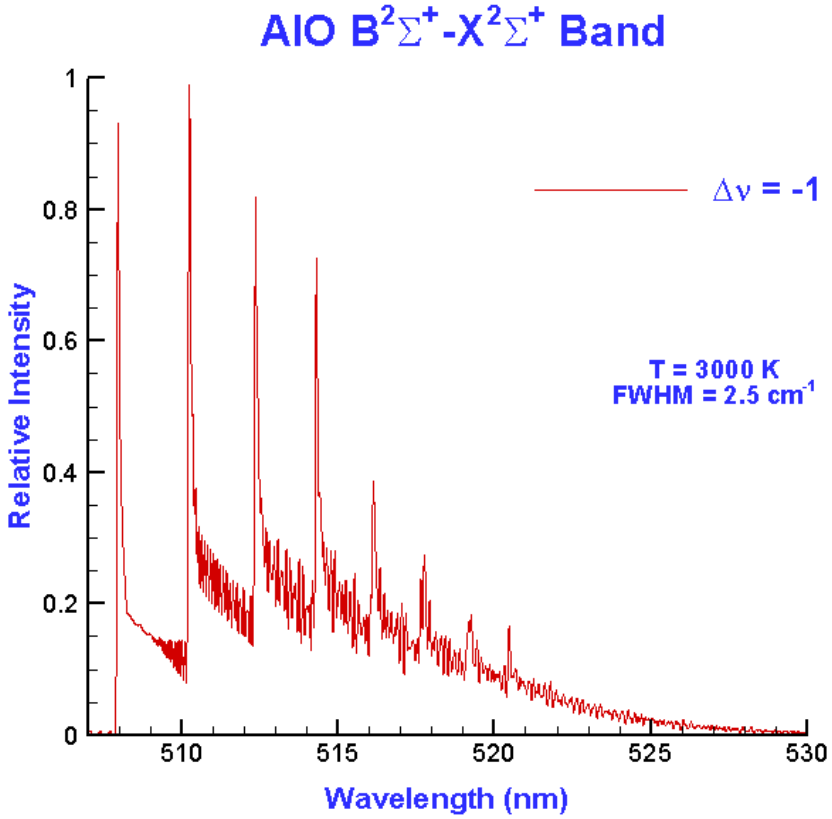

Figure 1.7: Computed AlO $B^2\Sigma^+ \rightarrow X^2\Sigma^+$ $\Delta\nu$ = -1 transition band corresponding to a temperature of 3000 K at a spectral resolution of 2.5 cm^{-1} (111).

The propellant testing included a vertical scan of the propellant plume in an upwards burn. The scan took pyrometer and spectrometer samples at specified time

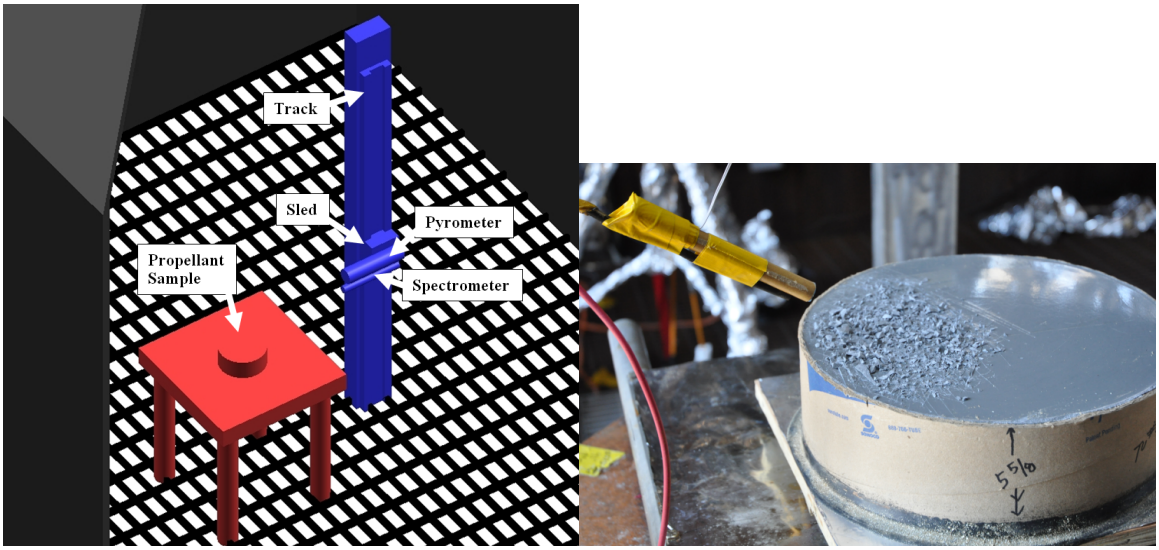

(a) (b)

Figure 1.8: Schematic of test set-up (left) with propellant on table next to track (right) (162; 111). Grated floor allows for ventilation and purge of smoke.

intervals, as a stepper motor carried the optics alongside the plume for various tests. An eight-foot vertical stepper motor was placed 4 feet away from each of the propellant tests. This stepper motor was oriented so that the optics faced the center of the plume, and lasers were used to align the optics and ensure they were oriented along a horizontal plane. A schematic image of the apparatus is provided by Figure 1.8a, while Figure 1.8b shows the propellant prior to ignition. The light emitted from a propellant plume was analyzed by both a spectrometer and a pyrometer. The stepper motor was set to travel about 0.56 inches/second, and took a single reading once per second, as the sled travelled up the track. Once at the top, the sled travelled back down the track and continued to take readings. To further correct for the position of each measurement, the burn height of the propellant was noted before each test. Assuming a constant burn rate, the height of the burning surface could be calculated at any point in the test knowing the test interval and initial height.

The observed AlO spectra is seen superposed to what is to be considered a background spectrum. For flame emission spectroscopy, this background is expected to be characterized by one of the black body radiation functions (148). For emissivity,

ε=1, the background would be expected to resemble a pure black body curve. However, typical emissivity will be a function of wavelength, $\varepsilon(\lambda)$. In the flame plume, it is possible for AlO particles to be smaller than the wavelength of light. If this is the case, the light emission cross-section will follow the Rayleigh limit and decrease as $1/\lambda$. In the wavelength range of interest, molten bulk AlO will have an absorption index also decreasing as $1/\lambda$. Thus, the observed background might be inversely dependent on λ^2 (40; 150).

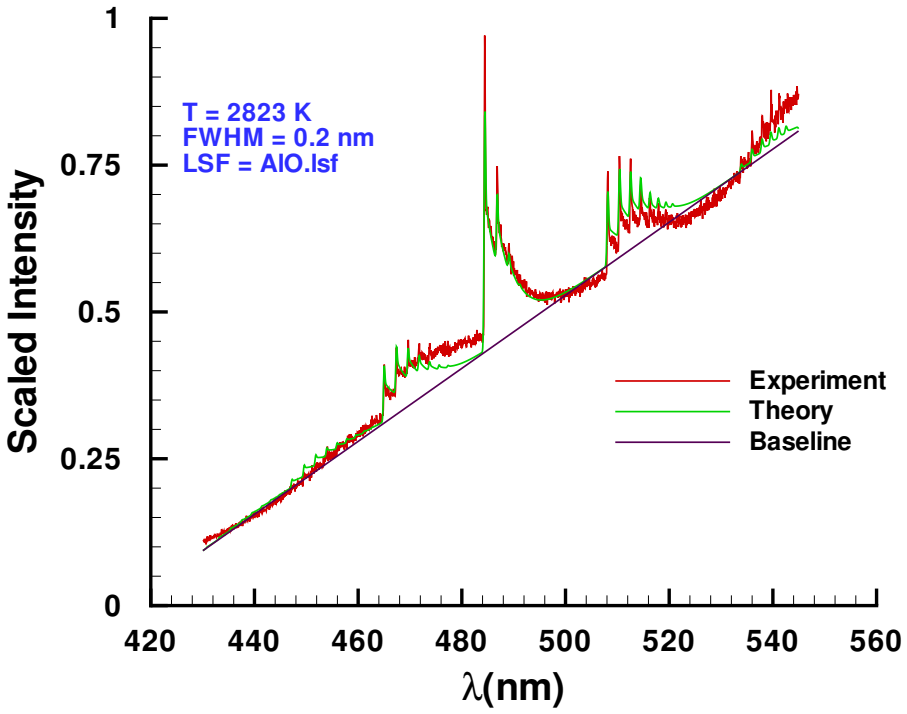

Figure 1.9: Propellant plume: Measured and synthetic emission spectra for AlO $B\,^2\Sigma^+ \rightarrow X\,^2\Sigma^+$ (98).

The collected spectra are fit with the predicted AlO spectra using a Nelder-Mead algorithm (92). Figure 1.9 provides an example of a measured spectrum with AlO contributions fit with a computed AlO spectrum. One strength of the Nelder-Mead method is that it provides a multi-variable fit. This enables one to determine several

best fitting micro-plasma parameters of the molecule, simultaneously. For the current experiment, all variables excluding temperature are to be held at fixed values. The best fitting temperature value becomes our inferred temperature for the molecular transitions. The algorithm also allows for a constant, linear, or quadratic baseline offset to the theoretical spectra. This provides a tool to fit diatomic spectra even when the black body or grey body background contributions are not well known.

Further analysis of the background contributions is beneficial. By fitting the background with various black body and grey body curves, not only may a temperature of the other particles in the combustion plume be inferred, but also the wavelength dependence of the emissivity will be determined. Knowing how the emissivity changes as a function of wavelength provides insight into the average particle size for that portion of the plume.

Figure 1.10 displays the intensity calibrated spectra gathered from the plume, while Figure 1.11 shows the intensity calibrated broadband spectra measured. The various line colors represent each of the 18 data sets outlined in Table 1.1. The measurements were collected at a height of 47, 59.7, and 72.4 cm above the propellant surface for data sets 1-6, 7-12, and 13-18, respectively. Table 1.1 provides the inferred temperature for each measurement shown in Fig. 1.10 and Fig. 1.11.

The inferred temperature is a result of a Nelder-Mead fit of the data with computed AlO spectra. As can be seen in Fig. 1.10 and Fig. 1.11, the signal to noise ratio for the AlO and background spectra is quite low for certain data sets. Also, Fig. 1.11 contains atomic peaks characteristic of Na and K, along with other unidentified line shapes.

For measurements near the propellant surface, there may be a $1/\lambda$ dependence and also a $1/\lambda^2$ dependence in the background. A $1/\lambda$ dependency indicates emissivity from particles on the order of less than 0.1 μm, while a $1/\lambda^2$ dependency is characteristic of molten bulk aluminum (40; 150). For measurements along the plume, there appears to be a higher temperature in the background contributions.

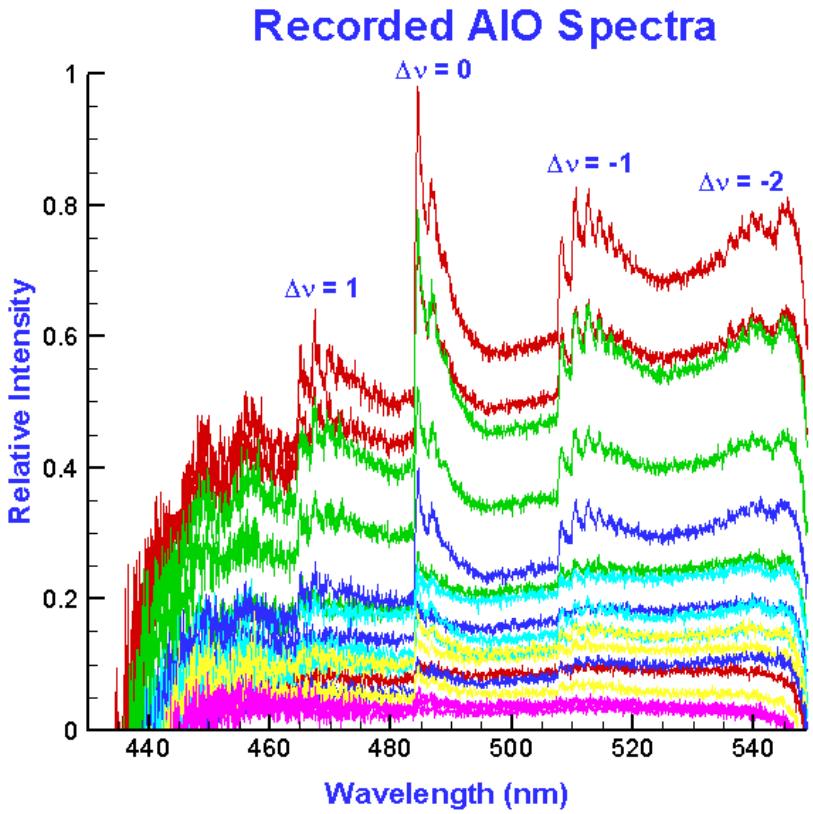

Figure 1.10: AlO molecular spectra were used to infer temperature from this calibrated data set, given in Table 1.1. The $\Delta\nu$ = 1, 0, -1, and -2 transitions are clearly visible for the $B^2\Sigma^+ \rightarrow X^2\Sigma^+$ band (111).

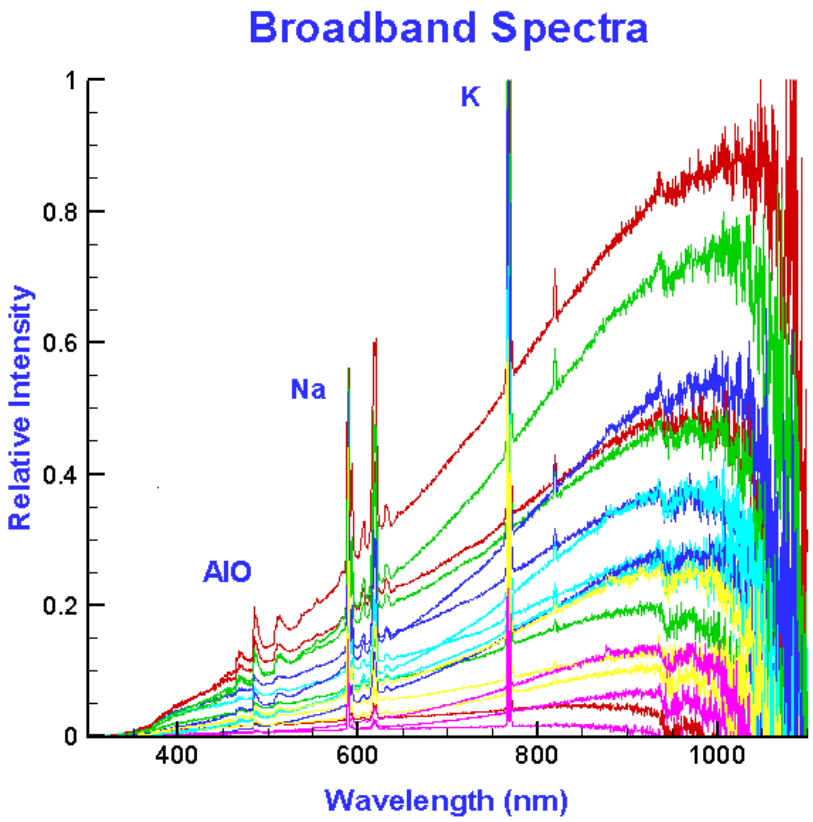

Figure 1.11: AlO molecular spectra were used to infer temperature from this broadband calibrated data set. The measured spectra contains atomic peaks for Na and K, along with not yet identified peaks. Notice the location of the background maximum (111).

Table 1.1: Inferred AlO temperature for Figures 1.10 and 1.11. Data sets 1-6, 7-12, and 13-18 were collected at a height of 47, 59.7, and 72.4 cm above the propellant surface, respectively (111). An asterisk denotes low signal and/or noisy data.

$DataSet$	$Horizontal(cm)$	$Fig.4$ $T(K)$	$Fig.5$ $T(K)$
1	57.8	2543*	2601
2	60.3	2713*	2461
3	62.9	2714*	2327
4	65.4	2668*	2384
5	68.0	2688*	2486
6	70.5	—*	3024*
7	57.8	2933	2743
8	60.3	2979	2740
9	62.9	3085	2837
10	65.4	3059	2739
11	68.0	2676*	2688
12	70.5	2539*	2767
13	57.8	3037	2871
14	60.3	3061	2889
15	62.9	2991	2890
16	65.4	2875	2809
17	68.0	2788	2752
18	70.5	—*	—*

This is indicated by the background maximum occurring at longer wavelengths. This feature closely resembles a black body, meaning there is near constant emissivity.

1.3.2 Nitric Oxide

Investigations into nitric oxide (NO) have been recently conducted at UTSI utilizing LIBS in laboratory air as well as in a vacuum cell (34). A goal was to observe the NO gamma transition band around the spectral region at 240 nm. The observed spectra are then fit with synthetic spectra computed from theory for the diatomic molecule in order to infer the temperature of the observed NO. Results are compared to a previous investigation using a similar technique (108). The previous experimental studies included the analysis of the spectra with a well-known NASA program based on the Gordon-McBride code called NEQAIR (Nonequilibrium Air Radiation) (117; 73), which is widely used in the field of combustion and chemical propulsion.

The illustration provided in Figure 1.12 generally describes the LIBS approach used to gather data for analysis with both NEQAIR and the computed line strength tables. The earlier experiments, analyzed with NEQAIR, consisted of LIBS in a cell containing a 1:1 mixture of N_2 and O_2, as well as plasma in air. Data analysis with NEQAIR allows for the consideration of the concentration of species present in the plasma. While Figure 1.13 allows for a general overview of the species concentrations found in laboratory air for a range of temperatures, Table 1.2 and Table 1.3 provide concentration values for neutral and ionic species, respectively. The temperatures of 6700 K and 6000 K represent the result of temperature analysis using NEQAIR at 25 and 50 μs following laser-induced optical breakdown, respectively.

Table 1.2: Neutral species number densities (cm^{-3}) for T=6000K and T=6700K.

T(K)	N	O	Ar	N_2	O_2	NO
6000	2.3×10^{17}	3.9×10^{17}	8.5×10^{15}	6.6×10^{17}	3.3×10^{14}	1.0×10^{16}
6700	4.6×10^{17}	3.1×10^{17}	6.8×10^{15}	3.6×10^{17}	7.8×10^{13}	4.5×10^{15}

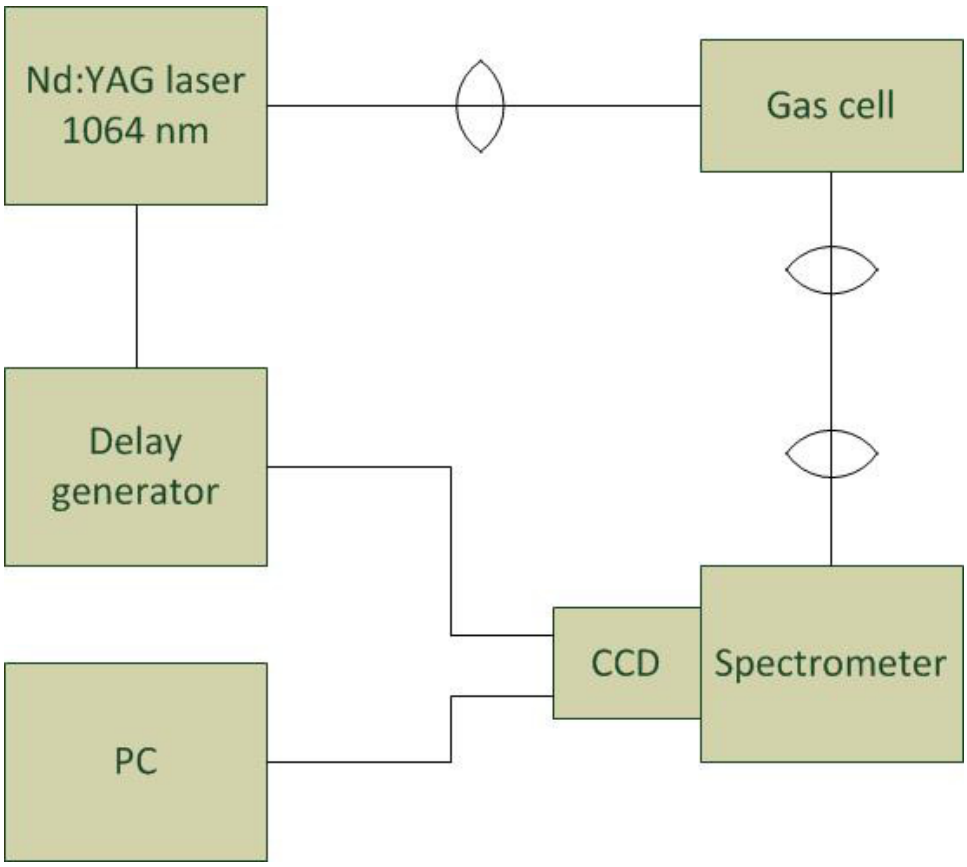

Figure 1.12: Diagram of the laser-induced breakdown experimental apparatus.

Table 1.3: Ionized species and free electron number densities (cm^{-3}) for T=6000K and T=6700K.

T(K)	N^+	O^+	Ar^+	N_2^+	O_2^+	NO^+	e
6000	0	0	0	0	0	2.7×10^{14}	2.7×10^{14}
6700	4.7×10^{13}	4.8×10^{13}	0	0	0	4.4×10^{14}	5.4×10^{14}

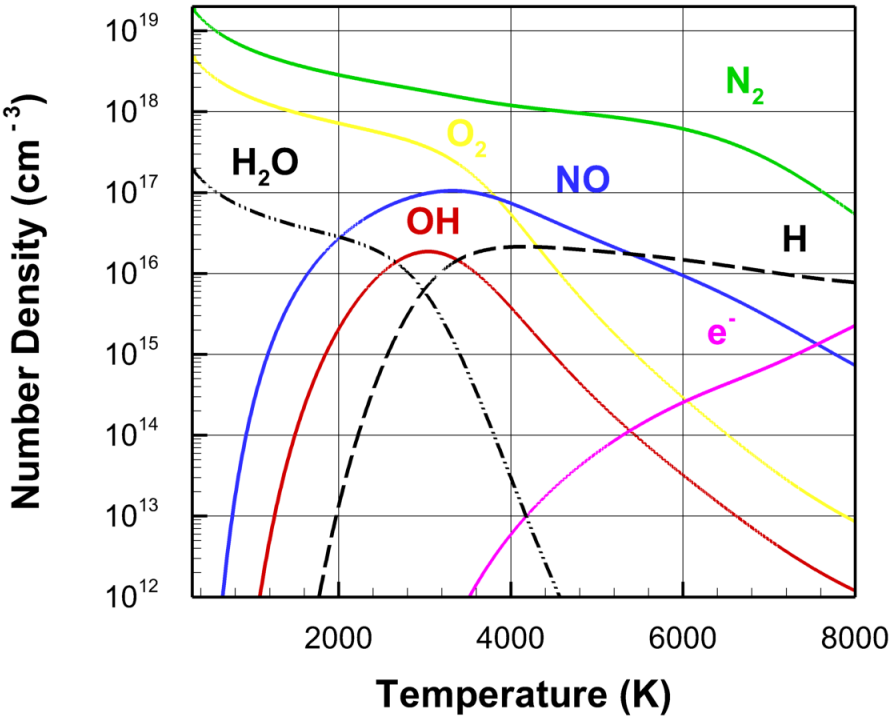

Figure 1.13: Species concentration in air as a function of temperature.

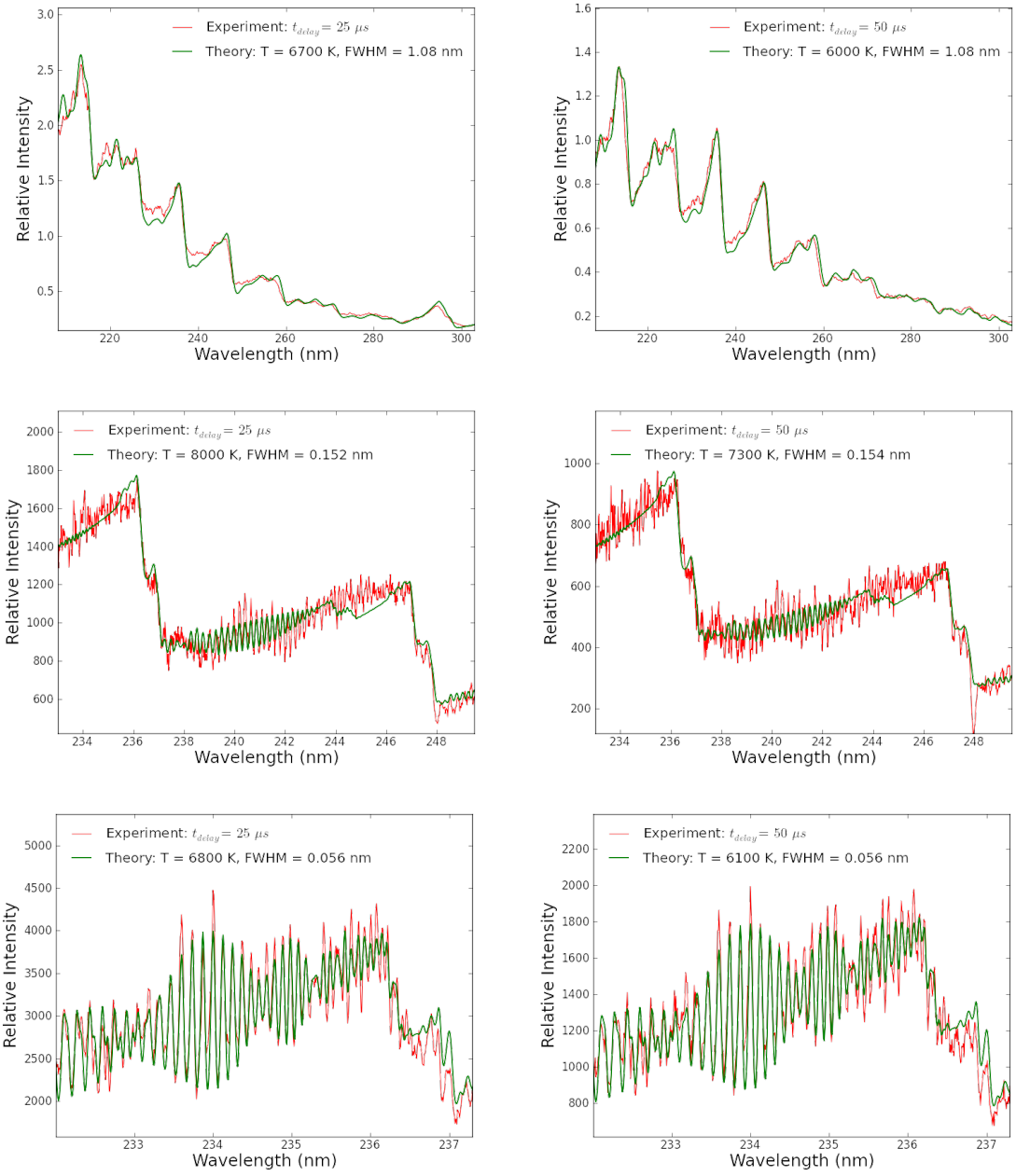

(a) NO at $t_{delay} = 25\mu s$ **(b)** NO at $t_{delay} = 50\mu s$

Figure 1.14: NO spectra gathered at $t_{delay} = 25\mu s$ (left) and $t_{delay} = 50\mu s$ (right) using gratings of (from top) 600, 1800, and 3600 grooves/mm with theoretically computed spectra from NEQAIR (top) and UTSI line strength tables (middle,bottom).

Temperature inferences made by analyzing the emissions of laser-induced plasma by means of NEQAIR and spectra computed from calculated line strengths demonstrate remarkable agreement, as seen in Figure 1.14. Fig. 1.14a and Fig. 1.14b each provide spectra collected at three different resolutions for delay times of 25 μs and 50 μs, respectively. For broadband wavelength spectra, NEQAIR is a useful tool for temperature analysis. For more resolved observed spectra (<0.1nm FWHM), diatomic spectra generated from accurately computed line strengths provide an excellent means for inferring temperature. This is attributed to the accuracy of computed line strengths. Such analysis utilizing calculated line strengths lends itself to investigations concerning laser-induced fluorescence (LIF) (48). LIF spectra often portray a characteristic 'comb' like structure, which can readily be compared to highly resolved spectral intensities generated from line strengths. In particular, this approach is applicable for analysis of combustion processes in high temperature flames (140).

1.4 Laser Ablation of Titanium

The scope of this dissertation concerns the diagnostics and characterization of laser-induced plasma resulting from laser ablation of a titanium sample. Traditional methods for the diagnostics of LIP include beam deflection (33), mass spectrometry (67), laser probing (3), laser absorption, laser-induced fluorescence (52), and optical emission spectroscopy (156). The experimental investigations reported in this dissertation utilized optical emission spectroscopy exclusively as a means of gathering data. Furthermore, the laser ablation of the titanium sample is performed in laboratory air at standard laboratory conditions. The experimental apparatus applied for this research is the topic of Chapter 2.

In comparison with the previous work discussed in this chapter, the current research concerning laser ablation of titanium contains very many similarities. However, there are some notable differences. While the previous work concerning AlO focused on observing diatomic spectra in a continuous flame pool, the current research

observes TiO in a laser-induced plasma. The experimental spectra is collected at typically shorter windows, and at the time delays when TiO spectral lines are noticeable there is not a continuous emission background. Thus, the TiO emissions are typically not superposed to a blackbody or grey-body slope.

The previous research discussed concerning C_2 resulted in data containing C_2 spectral transitions as well as hydrogen Balmer series lines. In parallel to how the AlO research allows for inferences from the diatomic spectra as well as the background it is superposed upon, the C_2 research provided inferences from the diatomic spectra as well as from the hydrogen spectral lines the C_2 lines were superposed upon. In contrast, the laser ablation of Ti experiments are designed such that the background contributions to which the spectral lines of interest are superposed are minimized. Unlike the NO experiments, considerations for the various species not containing Ti present in the plasma are neglected. This is justified by the luminosity and multitude of Ti atomic lines present in the observed spectra through much of the delay times of interest and the luminosity of the TiO transitions observed at delay times beyond 60 μs (166; 165; 163; 167).

For the purposes of plasma diagnostics at time delays within the first hundreds of nanoseconds subsequent to laser plasma formation, atomic spectral line shapes are investigated. Such analysis provides inferences for electron density n_e and temperature T_e. While the hydrogen Balmer series has been well documented as preferred line shapes for such analysis, at the earliest delay times studied in this research, the Balmer lines are too broad to be useful. This broadening is mostly attributed to Stark broadening associated with the electron density at such time delays. Therefore at these earliest time delays, a nitrogen spectral line is observed as well as the titanium lines available in the spectra. The study of such atomic spectra not only allows for the refinement of analytic techniques used to infer micro-plasma parameters, but also provides a medium to study the effects of the spectral line-width and self-absorption, which may be noticeable for molecular spectra as well. Since molecular spectra may sometimes appear superposed to atomic emission

spectra, atomic spectra are often treated as background, when studying the molecular spectra (98; 162; 110; 169; 111). Accurate analysis of such atomic spectra allows for more precise background identification and thus more precise molecular predictions. Inferences made from gathered spectra contain atomic and/or diatomic species is the topic of Chapter 4. While a complete understanding of the evolution of a LIP of an ablation plume requires comprehensive knowledge of the processes occurring within the first few nanoseconds, the main focus of the research reported here is the identification and analysis of the titanium monoxide molecule in the plasma.

1.4.1 Titanium Monoxide

Bands of the TiO molecular transitions have long been observed in stellar spectra (83; 16; 160; 17; 129). Despite its relatively low abundance in stars, TiO dominates from the infrared to the blue part of the spectrum for late type stars (60). The temperature sensitivity of molecular band intensities for diatomic molecules have provided a useful tool in determination of excitation temperatures (121; 87; 155). Electronic band systems of TiO are so prominent in the visible spectrum of M-type stars, that in establishing spectral types, the band systems are the primary criterion (68; 85; 81; 59; 63). Of particular interest is the effect of TiO opacity on stellar atmospheres (19; 70; 60; 1). TiO bands have even been used to determine the oxygen abundance of late-K and early-M dwarf stars (139).

Due to the significance of the TiO molecule in stellar observations, much work has been devoted to experimental investigations and theoretical development of the electronic transition band systems of TiO (121; 155; 71; 76; 78; 146; 26; 138; 147; 119; 8; 127; 2; 30). By gathering spectra at opportune delay times following laser-induced optical breakdown (LIOB), LIBS offers a rapid and reliable procedure for determining micro-plasma parameters (105). For spectral data containing contributions from diatomic transitions, the collected spectra may then be fitted with synthetic spectra (31) calculated with varying mirco-plasma parameters, such as temperature and

electron density (103). As evident in the Section 1.3, in finding the best fit the numerical value of these very parameters for the atom and/or molecule being observed may be inferred. The effectiveness and reliability of this particular technique for analyzing diatomic molecules is heavily dependent upon the accuracy and precision of the line-strength files for the synthetic spectra computed. Not only is an understanding of diatomic quantum theory necessary, but also careful attention must be paid to subtle details in the computation process, which may produce appreciable effects.

1.4.2 Theoretical Approach

The theoretical models used throughout this research are the topic of Chapter 3. Discussed are the various LIP assumptions typical of LIBS, such as local-thermodynamic equilibrium and self-absorption. A general overview of the evolution of laser ablation plasma is also provided. Also, this chapter contains further discussion on the models applicable in diatomic quantum theory.

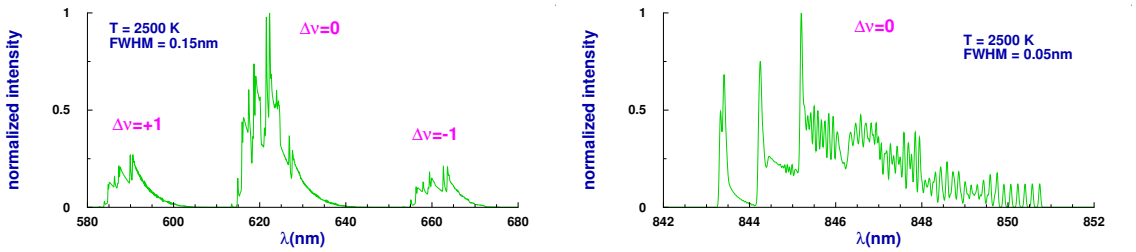

(a) TiO γ', $B^3\Pi \rightarrow X^3\Delta$ **(b)** TiO E→X $\Delta\nu = 0$

Figure 1.15: Left: TiO γ', $B^3\Pi \rightarrow X^3\Delta$, sequences and progressions, T = 2,500 Kelvin, FWHM = 0.15 nm. Right: TiO E→X $\Delta\nu = 0$ band, T = 2,500 Kelvin, FWHM = 0.05 nm (112).

As a part of this research new, accurate line-strength values for the TiO molecule are computed. Focus has been placed on the TiO γ, γ', and E-X transition systems. Figure 1.15 displays the γ' band system alongside the E→X $\Delta\nu = 0$ band (112), while Figure 1.16 shows the fit of a synthetic TiO gamma-band computation and a

measured emission spectrum in laser ablation plumes (28). These band systems have been chosen due to the availability of tabulated angular momentum transition values, which were experimentally obtained (122; 123; 124; 125; 126). A computer program was then implemented, calculating the upper and lower Hamiltonian matrix values. This allows for the generation of line-strength files, which can be plotted for various temperatures and spectroscopic parameters. However, TiO has many band systems, and interestingly these band systems overlap one another across the TiO spectrum. This presents a greater challenge in properly identifying and characterizing the TiO molecule in a micro-plasma. However, spectral regions where there are significant contributions from different transition bands may also provide information on relative prominence of specific transitions occurring. As a result of the many different TiO transition bands and their overlapping, a great deal more computational work is necessary to fully understand the TiO spectrum.

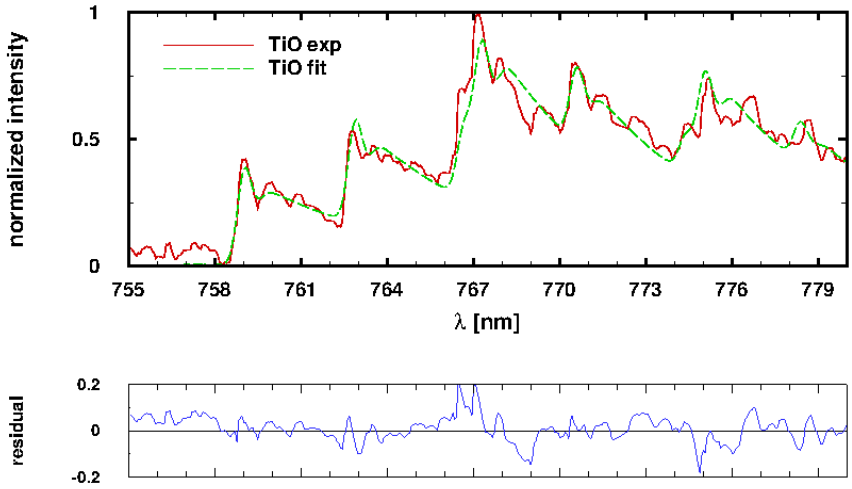

Figure 1.16: Comparison of measured (28) and synthetic emission spectra for TiO, $A^3\Phi \rightarrow X^3\Delta$ electronic transition, γ-system. The synthetic spectra corresponds to FWHM = 0.5 nm and T = 2,170±60 K.

1.4.3 Numerical Analysis

Numerical techniques are an underlying theme throughout the work discussed in this dissertation. As methods of fitting synthetic spectra to collected spectra are key to inferring plasma parameters, knowledge of numerical techniques is necessary. However, numerical analysis is not limited to fitting and generating synthetic spectra, but also includes error analysis. Such techniques as repeated Monte Carlo simulations are utilized and investigated in predicting error present in results. Monte Carlo simulations are appropriate for determining the error in a temperature measurement and likely other inferred parameters, such as background and line-width (102; 112; 166).

This research utilizes two forms of Monte Carlo-like analysis for temperature inferences from diatomic spectra. The most often used approach involves randomly adjusting the assumed spectral baseline, while fitting a collected diatomic spectrum to make an inference. In this procedure, a single spectrum will be repeatedly fit assuming a spectral baseline at random within a specified threshold. The resulting temperatures inferred from the routine provide a range of temperatures for statistical analysis. Likewise, intensity across a spectrum may be randomly adjusted within a specified threshold to simulate shot-to-shot variation in LIBS measurements. Repeated fitting of such a randomly altered spectrum will also provide a range of temperature values for statistical analysis.

Due to the computational demands of performing a Nelder-Mead fitting routine over thousands of iterations for even just a single gathered spectrum, batch processing is used throughout this research. Furthermore, the Newton High Performance Computing cluster at the University of Tennessee in Knoxville is utilized for parallel batch processing of experimental data. Such techniques are the topic of Appendix C.

Chapter 2

Experiment

This research consisted of many experimental investigations designed to examine the LIP from laser ablation of titanium (112; 168; 166; 165; 163; 167; 161; 164; 115). These experiments took place over a couple years ranging from the Fall of 2011 to the Winter of 2013. While in general similar procedures were implemented for each experimental measurement (116), certain equipment used in the laboratory did vary between some experiments. Such equipment includes calibration lamps, spectrometers, and detection devices. Because much of this research is aimed at addressing the temporal evolution of LIP, the delay times subsequent to laser ablation and the temporal gate widths used vary from experiment to experiment. The current chapter will serve to provide an overview of the experiments concerning titanium spectral emissions from plasma performed to advance this research. The following descriptions are limited to include all experimental measurements producing data and results contained in this dissertation.

Initial investigations concerning titanium spectral emissions from plasma began with the computation of the line-strengths of selected TiO transition bands (112). Before studies into titanium LIP began in earnest, exploratory measurements were carried out with two distinct purposes. The first goal of these exploratory measurements was to determine if the spectra computed from our newly calculated

line-strengths were accurate enough for micro-plasma inferences. The second goal was to determine if we can in fact use the computed spectra to analyze optical emissions from a LIP in our lab.

In order to test whether the computed spectra from the newly calculated line-strengths were accurate, two collaborations occurred. The first of which included the fitting of our computed spectra for the $A^3\Phi \rightarrow X^3\Delta$ electronic transition to experimental data obtained by De Giacomo et al. (28) as illustrated in Figure 1.16. The second involved observing TiO transitions from a radio-frequency thermal plasma experiment at the Chemical Research Center of the Hungarian Academy of Science (112). Figure 2.1 displays the experimental apparatus, while Figure 2.2 provides a characteristic result.

In order to determine whether our computed spectra could be used to identify TiO optical emissions in our lab, experiments commenced by performing laser ablation of what was advertised as a titanium golf club head. The decision to use a golf club head was influenced by the thought that the resulting spectra should contain a multitude of elements beyond titanium and those present in laboratory air. Thus, if one could use our computed spectra to distinguish and analyze TiO spectral transitions from the many other transitions present, then titanium is indeed an excellent choice for our laser ablation experiments.

An important aspect of measuring molecular spectra in a laser-induced plasma is knowing when to look (163; 161; 164). Molecular structure typically becomes discernable on the order of microseconds after optical breakdown (110; 166). In order to make measurements of the TiO spectra in the laser-induced micro-plasma at various time delays, the laser as well as the spectrometer must be synchronized accordingly (163; 116). For our initial experimental apparatus as illustrated in Figure 2.3, this goal is initialized by setting a Wavetek FG3C wave generator to $\sim$50 Hz. This signal is sent to an optical multichannel analyzer (OMA) synchronization box. The synchronization box then sends the signal to event and sync inputs on an OMA EG&G. The synchronization box also sends a 'divide by five' signal from the "Laser"

output to the delay generator. The delay generator, now triggered by the wave generator at 10 Hz, then relays the signal to trigger our laser's flash lamp. Another output of this delay generator is then sent to the back of the OMA EG&G and connected to the "Trigger In". Via a T-connector, this "Trigger In" is also connected to the Event of the "TTL Trigger Input" on the back of the OMA. The "Sync" for the "TTL Trigger Input" on the back of the OMA is connected to the "Sync" of the OMA synchronization box. This setup allows for control of when the OMA begins reading data by adjusting a delay on the delay generator. If the "start" button on the OMA display screen is pushed and it begins reading data with too much of a delay, a step will appear on the count vs. pixel read out. By adjusting the delay with the delay generator, this step can be moved across the screen until it is at the very edge. Our event is now also set to occur on the first of five readings. Thus, we take one good reading and then four readings, which will be ignored. This serves to 'flush' the detector of any residuals. Once the computed spectra was successfully used to identify the TiO $B^3\Pi \rightarrow X^3\Delta$, $\Delta\nu = 0$ transition in the laser ablation plume of the golf club head, experiments concerning laser ablation of a pure titanium sample were performed.

2.1 Thermal Plasma Experiment

In the plasma chemistry group at the Chemical Research Center of the Hungarian Academy of Science, synthesis is of interest of non-oxide, ceramic powders in thermal plasma. For the experimental studies, a radio-frequency (RF) plasma reactor was employed at atmospheric pressure. The RF power is produced by a generator operating at 3-5 MHz. The plate power of 20 to 30 kW is inductively coupled to a TEKNA PL-35 torch that is connected to a water-cooled plasma reactor, cyclone, filter unit and a vacuum pump. The precursor powders are injected axially into the plasma flame through a water-cooled probe by a PRAXAIR powder feeder. Figure

2.1 illustrates the experimental schematic, and it also shows a photograph of the experimental arrangement in the laboratory.

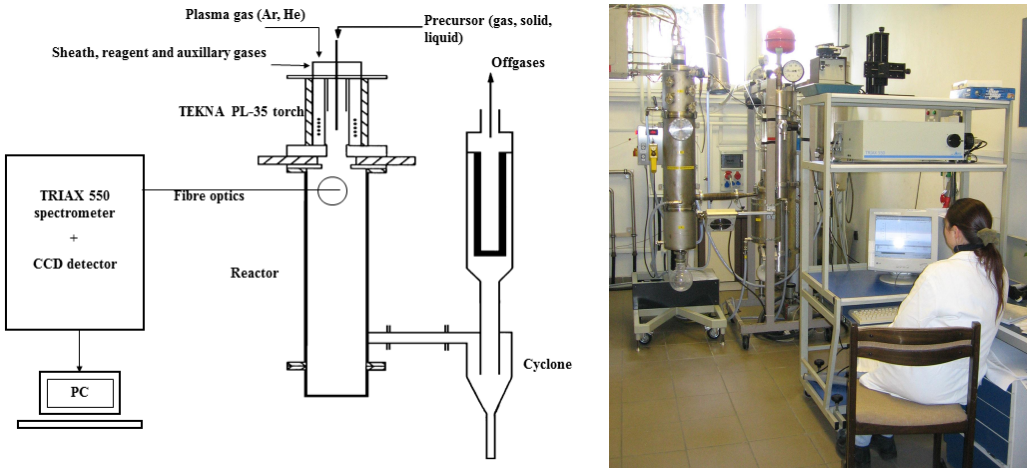

Figure 2.1: Experimental schematic (left) and photograph of the laboratory arrangement (right) (112).

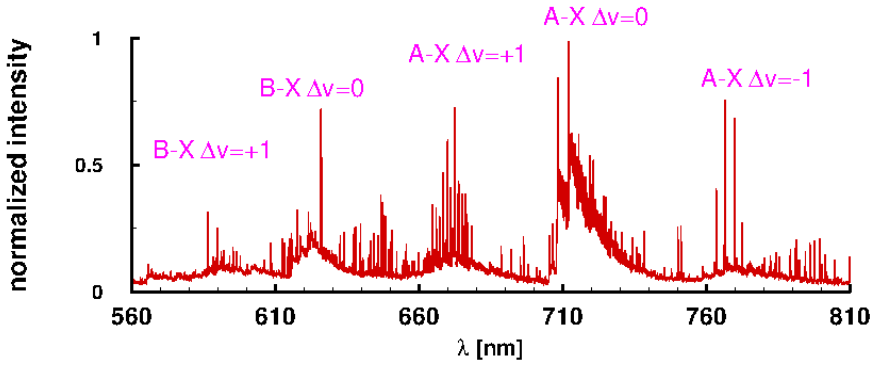

Figure 2.2: Continuously recorded emission spectra RF plasma reactor (112).

Plasma emissions are detected perpendicularly to the axis of the plasma flame, through a quartz glass window at distance of 0.1 m from the bottom of the plasma nozzle. The radiation is dispersed by a 0.55 m focal length monochromator (TRIAX 550 Jobin-Yvon), using a grating with 1200 grooves/mm showing a reciprocal

dispersion of 1.55 nm/mm. Light is collected and imaged to the entrance slit with the aid of a fiber optic bundle (6 fibers, but due to intense plasma emission we usually cover 4 fibers). Plasma emission is recorded with a optical multi-channel analyzer (CCD-3000). The available spectral range is 200-1000 nm. Figure 2.2, displays a recorded spectrum in the range 560-810 nm when feeding TiO_2 into the plasma. Feeding of the TiO_2 into the flame was rather difficult and non-uniform.

2.2 Laser Ablation Experiments

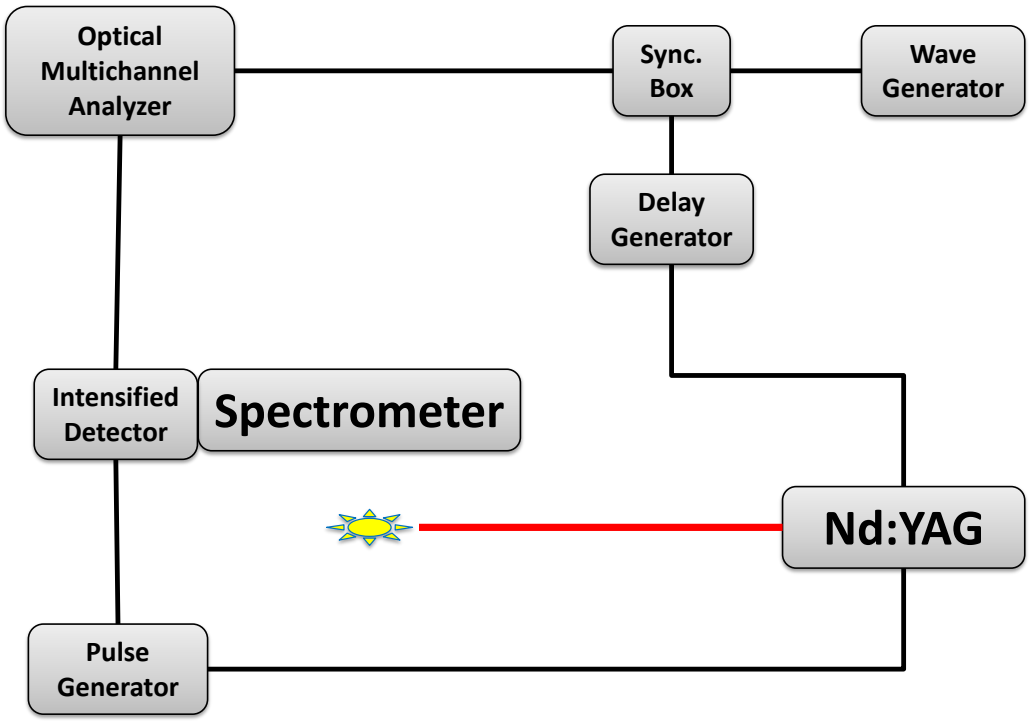

Figure 2.3: Experimental arrangement for measurement of TiO spectra following LIB of metallic titanium in laboratory air.

2.2.1 Measuring the TiO γ' Band

A typical LIBS set up was implemented for this experiment, see Figure 2.3. This consisted of a 13 ns Q-switched Nd:YAG Quanta-Ray DCR-2A(10) laser, as seen in Figure 2.4, operating at its fundamental wavelength of 1064 nm with 90 mJ per pulse. The spectrometer and detector used were the 0.5 m model 500 SpectraPro Acton Research Corporation spectrometer equipped with a 1200 groove/mm grating and an intensified linear diode array (model 1460 Princeton Applied Research detector/controller optical multichannel analyzer). The detector then provides a 1024 pixel spectrum of the observed event. In Figure 2.5b, the pulse generator, resting on top of the spectrometer, provides a high-voltage pulse triggering the intensified linear diode array, attached to the right-side of the spectrometer. The output of the linear diode array detector is then displayed by the optical multichannel analyzer to the right of the spectrometer in Fig. 2.5b.

Figure 2.4: Nd:YAG Quanta-Ray DCR-2A(10) laser used in laboratory.

At the exit of the laser cavity, the 532 nm wavelength portion of the beam was deflected to a beam stop, while the 1064 nm wavelength was focused vertically downward on the flat surface of a titanium sample to approximately a 1 mm spot size, as seen in Figure 2.5a. The ablation plume is imaged onto the spectrometer's slit by two field lenses which are chosen to match the $f\sharp$ of the spectrometer. The titanium sample was rotated as data was collected. This was done to reduce the effects of craters from previous shots caused by laser ablation. The experiment is conducted without the use of a chamber. The oxygen component of the observed TiO is assumed to be provided by the laboratory air.

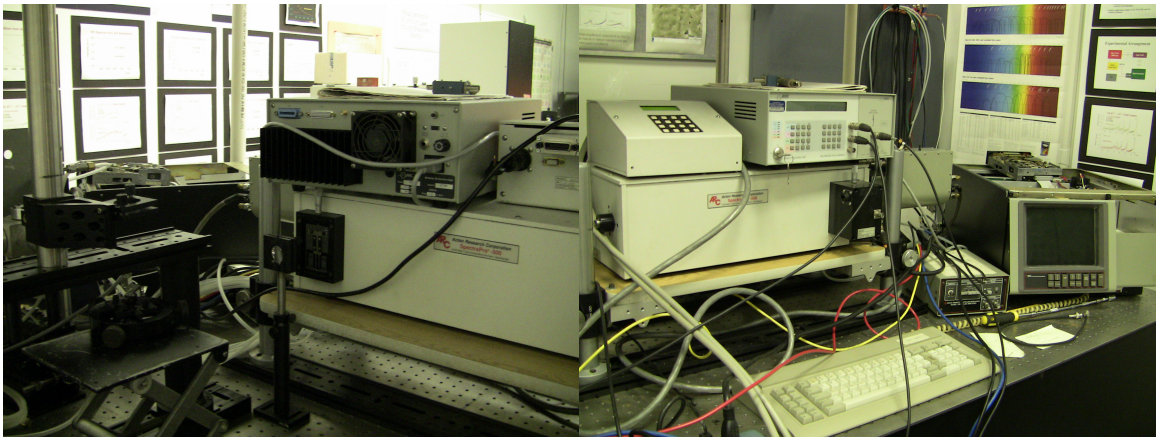

(a) **(b)**

Figure 2.5: Titanium sample at rest below focusing lens (left) on the aperture side of the spectrometer and detection equipment as viewed from the opposite side of spectrometer (right).

For satisfactory measurements, the spectrometer and optical multichannel analyzer were wavelength calibrated by use of a hydrogen lamp to locate the H_α Balmer series peak. The equipment was also intensity calibrated. This was accomplished by use of a tungsten lamp. A Leeds and Northrup Co. optical pyrometer was then used to measure the temperature of the active lamp. A blackbody curve was then calculated, and the measured spectral intensity of the lamp was compared to the curve for each wavelength range measured. This provided an intensity calibration factor for each pixel corresponding to every wavelength measured. These calibration factors

were then applied to the collected spectra. In the LIBS community, these sorts of calibrations are often neglected, as chemometrics is mainly used to identify principle components from the spectral 'fingerprint' observed. However, for this research such calibrations are essential for obtaining reliable results.

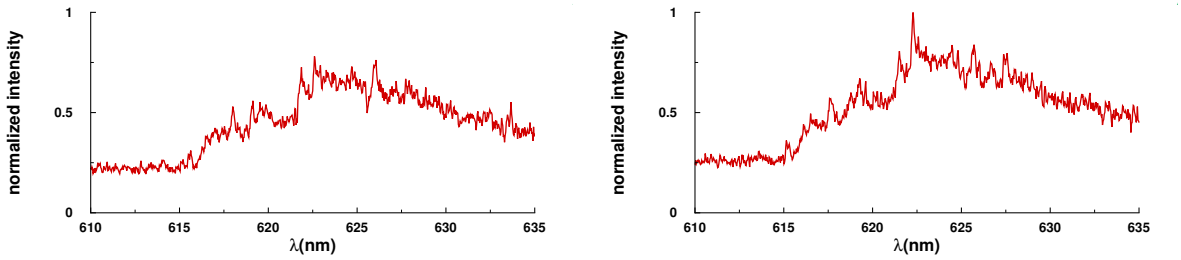

Figure 2.6: Recorded data following metallic titanium LIB in laboratory air (112). Delay time: $\Delta\tau = 75$ μs, gate width: 32 μs. Notice the difference between the two single-shot measurements.

As this was the first experimental investigation observing LIP from our pure titanium sample, the spectrometer was adjusted to observe a rather expansive wavelength range. The crux of these measurements observed the wavelengths of 555-640 nm. Primitive analysis of this data began by visually inspecting the measured spectra against computed spectra. An interesting initial finding occurred on the wavelength interval of 580-610 nm. Our measurements here indicate the presence of two different TiO transition band profiles. Figure 2.6 illustrates recorded data from single-shot laser ablation in the 610 to 635-nm wavelength range. Fig. 2.7 displays computed spectra in range of 580 to 610 nm, and 610 to 640 nm. For the latter, both the TiO γ and $\gamma\,'$ systems contribute. While both are present in the measured spectra, matching of the computed spectra of each band system shows minimal overlap. In principle, the relative intensities of the two systems may be used to determine the relative prominence in the plasma.

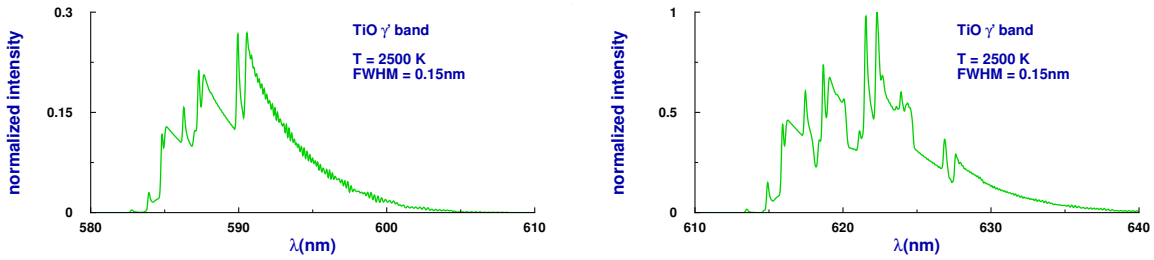

Figure 2.7: Computed spectra of TiO $\gamma\,'$ system for wavelength range 580 to 610 nm (left) and 610 to 640 nm (right), compare Fig. 2.6 (112).

2.2.2 Measuring the TiO γ Band

The experimental set up used to observe the TiO $A^3\Phi \rightarrow X^3\Delta$ transition band is identical to that of Fig. 2.3. However, there are subtle differences in the equipment used. The 13 ns Q-switched Nd:YAG Quanta-Ray DCR-2A(10) laser provided 160 mJ per pulse to the surface of the Ti 6-4 sample, whereas the excitation source only provided 90 mJ per pulse when observing the $B^3\Pi \rightarrow X^3\Delta$ transition. This was accomplished by adjusting the alignment of the aperture to the harmonic generator on the laser responsible for producing the frequency doubled component of the beam. Additionally, a Jobin Yvon HR 640 spectrometer equipped with a 1800 groove/mm grating was used instead of the Acton Research SpectraPro. Also in this experiment, a low-pass filter at 400 nm is positioned between the two field lenses, eliminating second order Ti atomic lines from the measurement.

While the experiment investigating the TiO γ' band was more exploratory, this experiment observing the γ band was designed to gain a perspective on the temporal evolution of the inferred temperature of the TiO transitions. Measurements observing the TiO γ, $\Delta\nu = 0$ transition band were collected at delay times ranging from 20 to 60 μs with a gate width of 5 μs. These measurements were gathered by incrementally increasing the delay time with 5 μs intervals. Then, another set of measurements were collected at time delays ranging from 26 to 60 μs with a 2 μs gate width measured at 2 μs intervals. A third experimental run gathered measurements of the γ bands at delay times ranging from 26 to 86 μs with a 2 μs gate width at intervals of 4 μs. For

the third experimental run a different Ti slab, which had not previously experienced laser ablation, was used to produce the plasma. Two additional measurements were also taken with this Ti sample at 90 μs and 95 μs delay times using a 2 μs gate width. At each time interval, the spectra gathered successively are added such that each measurement is an accumulation of 100 individual laser events.

2.2.3 Measuring Ultra-violet Ti Lines

In order to investigate titanium atomic transitions at earlier delay times in the plasma, the equipment used in the experimental apparatus was again slightly modified. The same spectrometer and grating were used as in the previous investigation into the TiO γ band only the detection is gated such that spectra are gathered with a 6 ns gate width. The 6 ns gate is provided by a Model 1302 Fast Pulser (EG& G Princeton Applied Research). The goal was to investigate various Ti II and Ti III emission lines located between 237 and 245 nm, as observed no later than 500 ns after plasma formation. So, the low-pass filter at 400 nm was removed from the apparatus. Again, all of the collected data were wavelength and sensitivity corrected. Now however, the sensitivity correction utilized an Ocean Optics (DH-2000-BAL) deuterium-halogen light source.

Thus, spectra from the ablation plume of the titanium sample in the wavelength region of 237 to 245 nm were collected to infer temperature by means of the Boltzmann plot method. These measurements were gathered at 10 ns intervals at delay times ranging from 20 to 100 ns after the laser event. The same spectral region was then examined at 20 ns intervals from 100 to 200 ns. Three additional measurements were then taken at 300, 400, and 500 ns times delays. Just as before, the spectra gathered successively are added such that each measurement is an accumulation of 100 individual laser events.

The spectrometer was then adjusted in order to observe the N II line at 399.5 nm. The N II transition was observed in the titanium ablation plume at the same

time intervals as before, ranging from 20 to 200 ns. The N II line was then fit with a Lorentzian profile. The full-width at half maximum (FWHM) was then used to infer the electron density, n_e, of the plasma.

2.2.4 Measuring TiO Along the Ablation Plume

So far, the experimental techniques described have provided glimpses into the temporal evolution of the emissions from atomic titanium and molecular TiO particles in a laser ablation plume. However, these investigations have not provided a proper means of analyzing the particle dynamics occurring along the plume. In order to observe such phenomena, the intensified linear diode array and OMA of the previous experiments is replaced with an Andor iStar ICCD camera. This camera provides two-dimensional images consisting of 1024 $\times$ 1024 pixels. The ICCD communicates to a computer operating the Andor iStar software dedicated to both controlling the ICCD and organizing the output from the ICCD via a USB cable. The software provides data acquisition features which eliminate the need for the synchronization equipment described earlier in the chapter. Thus, the Wavetek FG3C wave generator is used to trigger the laser just as before, and a laser output signal is used for synchronization within the iStar's software.

The experimental procedures of Sections 2.2.2 and 2.2.3 were performed again, now providing two-dimensional images. This time, the TiO γ band was observed at delay times ranging from 20-200 μs utilizing a 2 μs gate width, and the ultra-violet Ti III and Ti II lines were observed at a time delay of 200 ns with a 6 ns gate width.

Chapter 3

Models

Due to the growing interest in laser-induced breakdown spectroscopy as an analytical technique and the applications of laser-induced plasma for the production of thin films, numerous theoretical models have been applied in order to improve the basic knowledge and determine the optimal experimental conditions for laser-induced plasma processes. A complete discussion on laser-induced plasma would require volumes of theoretical and experimental results. Therefore, the goal of the research reported here is to consider only theoretical and experimental efforts made to describe the processes occurring during the expansion of the plasma plume above a laser ablated sample. The focus of this research is further limited to the luminous plasma produced by nanosecond laser ablation of a titanium surface. The dependence of ablation processes on laser parameters as well as the laser solid interaction are considered beyond the scope of this research.

3.1 Plasma Evolution

The processes associated with laser-induced plasma center around the interaction of high power laser radiation with matter. Here, the laser power is such that the surface layers of the material will experience vaporization, leading to the formation of an expanding plasma (52). When considering a nanosecond laser as an excitation

source, ablation can lead to ionization and heating by inverse Bremsstrahlung and photoionization processes producing an induced plasma with electron densities on the order of 10^{18}-$10^{23} cm^{-3}$ and temperatures of 30,000-100,000 K (100). The induced plasma experiences rapid expansion. During this time, inelastic collisions of electrons with heavy particles acts as the main mechanism for the transition of bound electrons from lower levels to upper levels. During the initial stages of plume expansion, the concentration of charged particles is determined by the electron impact ionization and three-body recombination of electrons with ions. In three-body recombination a single electron combines with an ion and another nearby electron or ion carries away the resulting energy. Thus, three-body recombination is seen as the inverse of impact ionization. Experimental investigations concerning the concentration of emitting levels rely on radiative processes occurring in the plasma such as spontaneous and stimulated emission along with reabsorption.

An initial LIBS spectrum, typically within the first tens of nanoseconds, is dominated by the spectral continuum contribution. This continuum is attributed to mechanisms involving free electrons such as inverse Bremsstrahlung and radiative recombination. Little if any information concerning atoms or ions can be inferred from the spectra of this time domain. As the plasma evolves, ionic spectral line transitions begin to appear in the plasma emissions along with the continuum contribution. The more highly ionized species will become prominent first followed by the lesser ionized species and ultimately the neutral atomic transition lines (13). Three-body recombination occurring with plasma expansion causes a rapid decrease of the electron density in the plasma. As a consequence of the decreasing electron density in the plasma, each emission line will become progressively more narrow during the plasma expansion.

After a characteristic time, depending on both the electron density and the elements in the plasma, emissions from radiative molecular transitions will become discernible as the prominence of atomic spectral lines observed in the plasma decreases. Of particular interest for this research is the diatomic molecular

radiative transitions of the plasma. Typically, this phenomenon is attributed to the recombination of atoms to form molecules. However, the detection of diatomic transitions of certain species at far earlier stages of plasma evolution when compared to other diatomic transitions in similar conditions leads to the conclusion that not all diatomic transitions are a product of recombination. In these scenarios, it is hypothesized that the molecule was present prior to plasma formation. However, many diatomic molecules observed in laser-induced plasma are unstable in typical laboratory environments. For such molecules, LIBS offers a suitable method for observation. The spectral transitions of such molecules can be collected typically for tens of microseconds. Often times, these emissions are quite luminous and present from the ultra-violet to the infrared.

3.2 Radiation Transfer

In general, the radiation transfer equation may be written as

$$\frac{1}{c}\frac{\partial}{\partial t}I_\lambda + \hat{\Omega}\cdot\nabla I_\lambda + \left(\sigma_{\lambda,r}+\alpha_{\lambda,r}\right)I_\lambda = \epsilon_{\lambda,r} + \frac{1}{4\pi c}\sigma_{\lambda,r}\int_\Omega I_\lambda d\Omega. \tag{3.1}$$

Here, c is the speed of light, I_λ is the spectral radiance, $\sigma_{\lambda,r}$ is the scattering cross section, $\alpha_{\lambda,r}$ is the absorption coefficient, $\epsilon_{\lambda,r}$ is the emission coefficient, and $d\Omega$ is the solid angle of propagation. Equation 3.1 provides spectral radiance, accounting for energy redistribution by scattering, energy loss by absorption, and energy gain by emission. If scattering is ignored, the incremental change of directional spectral intensity can be expressed as

$$dI\left(\lambda,\Omega\right) = \left[\epsilon\left(\lambda,\Omega\right) - \alpha\left(\lambda,\Omega\right)I\left(\lambda,\Omega\right)\right]dr, \tag{3.2}$$

where dr follows the line of sight (45). Using Kirchhoff's radiation law, $\epsilon_\lambda = \alpha_\lambda U_{\lambda,k_BT_e}$ with U_{λ,k_BT} representing the black body spectral intensity, Equation 3.2 can be

integrated along the line of sight from r_0 to r such that

$$I_\lambda = \int_{r_0}^{r} \alpha_\lambda U_{\lambda,k_BT} \exp\left(\int_{r'}^{r} \alpha_\lambda dr''\right) dr'. \tag{3.3}$$

If the path of the photon in the plasma is homogeneous ($\alpha_\lambda(r) = \alpha_\lambda$) and isothermal ($T(r) = T$), assuming the photons are able to escape the plasma, Equation 3.3 can be integrated in a straightforward manner. With R being the distance between r_0 and r,

$$I(\lambda, k_BT_e) = U(\lambda, k_BT_e)\left(1 - e^{-\alpha(\lambda,k_BT_e)R}\right), \tag{3.4}$$

provides the intensity emitted from a uniform plasma in local thermodynamic equilibrium (LTE) at a wavelength λ and electronic temperature T_e. The spectral absorption coefficient may be represented as

$$\alpha(\lambda, k_BT_e) = \pi r_0 \lambda^2 f_{ul} N^l P(\lambda_0, \lambda)\left[1 - e^{-\frac{hc}{\lambda k_B T_e}}\right], \tag{3.5}$$

where $r_0 = 2.818 \times 10^{-13}$ cm is the classical electron radius, f_{ul} is the absorption oscillator strength, N^l the lower level population density of the transition, $P(\lambda_0, \lambda)$ is the normalized line profile, and h is Planck's constant (51). For a laser-induced plasma, the spectral line profile, $P(\lambda_0, \lambda)$, is a convolution of a Lorentz function attributed to the effect of Stark broadening, a Gauss function due to the Doppler effect, and the apparatus function of the spectroscopic system. In application, the width associated with the Doppler effect is considered negligible. The experimental function introduced by the apparatus must be accounted for, but is also typically negligible.

3.2.1 Optical Thickness

If all of the emitted photons escape from the plasma, the plasma is considered to be optically thin. Under this assumption, the spectral line intensity for atomic transitions from an upper level u to a lower level l can be written as

$$I_{ul} = N^u h\nu_{ul} A_{ul} P\left(\nu_{ul}, \nu\right), \tag{3.6}$$

where N^u represents the population density of the upper level, ν_{ul} is the transition frequency, and A_{ul} is the transition probability from upper level to lower level. Equation 3.6 can be derived by substitution of Eq. 3.5 and the black body distribution into Eq. 3.4 assuming optical thinness $\alpha R \ll 1$.

If $\alpha R \gg 1$, the plasma is considered to be optically thick. In this case, Equation 3.6 must be rewritten to include terms accounting for self-absorption and induced emission. By defining the dimensionless optical thickness as $\tau_{\nu,k_BT_e} = \alpha R$, the spectral line intensity of Eq. 3.6 becomes

$$I_{ul} = \frac{I_{ul}^{thin}}{\tau_{\nu,k_BT_e}} \left(1 - e^{-\tau_{\nu,k_BT_e}}\right). \tag{3.7}$$

Typically in laser-induced plasma $\exp(h\nu/k_BT_e) \gg 1$ (13), and the contribution due to induced emission on a spectral line can be neglected. In the spectral range near the resonance, ν_0, Equation 3.4 gives $I_{\nu,k_BT_e} = U_{\nu,k_BT_e}$. This would result in a plateau in the form of a black body at the line center of strongly self-absorbed spectral lines emitted from a homogeneous plasma. In practice, the observed spectral line will often display a dip near the resonance wavelength and asymmetric wings with respect to the resonance wavelength.

3.3 Atomic and Ionic State Distribution

Much of the progress made in the analysis of laser-induced plasma has utilized Maxwell-Boltzmann statistics. However, the regime where such an assumption is valid is quite restrictive. It is valid only for LTE conditions and treats the plasma as a non-interacting ideal gas. Furthermore, Maxwell-Boltzmann statistics are meant to describe a collection of distinguishable particles, ultimately leading to the Gibbs paradox. The Gibbs paradox arises from considering quantum mechanical particles, such as atoms, as being distinguishable, when in fact they are inherently indistinguishable particles (42).

3.3.1 Boltzmann Plot Method

Assuming Maxwell-Boltzmann statistics, the distribution over states of an atom or ion obeys

$$\frac{N_i}{N} = \frac{g_i}{Q\left(T\right)} e^{\frac{-E_i}{k_B T}} \tag{3.8}$$

where $N = \sum_i N_i$ and

$$Q\left(T\right) = \sum_i g_i e^{\frac{-E_i}{k_B T}} \tag{3.9}$$

is the partition function, g_i is the statistical weight, and E_i the energy of the i^{th} state. Thus, Equation 3.6 representing the intensity of a spectral line from a homogeneous, optically thin may be expressed as

$$I_{ul} = h\nu_{ul} N^u R \frac{g_u A_{ul}}{Q\left(T\right)} e^{\frac{-E_u}{k_B T}}. \tag{3.10}$$

The ability to make the necessary assumptions resulting in Equation 3.10 is so coveted by experimentalists because this relation provides a tool to infer temperature from spectral lines. Known as the Boltzmann plot method (39), this technique

involves rewriting Eq. 3.10 in the form of a line such that

$$\ln\left(\frac{I_{ul}\lambda_{ul}}{g_u A_{ul}}\right) = \left(\frac{-1}{k_B T}\right) E_u + \ln\left(\frac{hcRN^u}{Q\left(T\right)}\right). \tag{3.11}$$

Given measured intensities of lines from various upper levels along with a measure of the density of the upper level, the left hand side of the equation can be plotted as a function of E_u. The resulting slope can be used to determine the temperature of the emitting species in the plasma.

3.3.2 Saha-Boltzmann Plot Method

Moreover, Equation 3.8 can be extended to describe the ratios of any two bound states i and j of an atom or ion such that

$$\frac{N_i}{N_j} = \frac{g_i}{g_j} e^{-\frac{E_i - E_j}{k_B T}}. \tag{3.12}$$

If the system in question is an electron-proton pair (45), Equation 3.12 would represent the relative probability for the pair to be in two bound states i and j. Generalizing this to continuum states with wave number k and energy E_k can be accomplished by replacing N_i with dN_k and g_i with dg_k. Here, dN_k and dg_k are the number density of free electron-ion pairs with electrons in the interval k to $k + dk$ and the number of free electron states in the same interval. Assuming a cubic normalization volume V, the number of modes in the wave number interval can be written

$$dN_k = \frac{V}{\pi^2} k^2 dk, \tag{3.13}$$

leading to

$$\frac{dN_k}{N_j} = \frac{V g_{ion}}{\pi^2 g_j} e^{-\frac{E_k - E_j}{k_B T}} k^2 dk. \tag{3.14}$$

Here, g_{ion} represents the possible degeneracy of the resulting ion. Integrating Eq. 3.14 over k and using $E_k = \hbar^2 k^2 / 2m_e$

$$\frac{N_e}{N_j} = \frac{V g_{ion}}{\pi^2 g_j} e^{-\frac{E_j}{k_B T}} \int_0^\infty k^2 e^{-\frac{\hbar^2 k^2}{2 m_e k_B T}} dk, \tag{3.15}$$

where $N_e = \int dN_k$ gives

$$\frac{N_e}{N_j} = V \frac{2 g_{ion}}{g_j} \left(\frac{m_e k_B T}{2\pi\hbar^2} \right)^{\frac{3}{2}} e^{\frac{E_j}{k_B T}}. \tag{3.16}$$

Choosing $V = 1/N_{ion}$ and combining constants into the ionization energy of hydrogen E_H and the Bohr radius a_0, Eq. 3.16 becomes what is known as the Saha equation (135; 136),

$$\frac{N_e N_{ion}}{N_j} = \frac{2 g_{ion}}{g_j a_0^3} \left(\frac{k_B T}{4\pi E_H} \right)^{\frac{3}{2}} e^{-\frac{E_{ion} - \Delta E_j}{k_B T}}, \tag{3.17}$$

where ΔE_j is the ionization energy of state j or in terms of atom N and ion N_{ion} densities

$$\frac{N_e N_{ion}}{N} = \frac{2 Q_{ion}(T)}{Q_{atom}(T) a_0^3} \left(\frac{k_B T}{4\pi E_H} \right)^{\frac{3}{2}} e^{\frac{-E_\infty}{k_B T}}, \tag{3.18}$$

where E_∞ is the ionization energy of the atom. Just as for the Boltzmann plot method, equations such as Eq. 3.18 may be rewritten to be used for the so-called Saha-Boltzmann plot technique. The advantage of the Saha-Boltzmann plot technique is that it tends to make more points available for plotting, and the available points are normally over a wider range of energy levels (154). Each of these factors serve to increase the precision of the temperature inference.

3.4 The Diatomic Line-strength

As the main focus of this research involves inferences made from computed diatomic spectra, it is important to discuss the diatomic eigenfunction used and the assumptions that go along with using it. As matter of fact, the relative simplicity and symmetry associated with diatomic molecules lead there to actually be minimal assumptions involved. Born and Oppenheimer (10) were the first to give the details of the exact separation of two of the Euler angles, θ and ϕ, describing rotation of the two nuclei. The angular momentum part of Born-Oppenheimer diatomic eigenfunction contained the spherical harmonic $Y_{\ell m}(\theta, \phi)$. Then, Wigner and Witmer (158) replaced the spherical harmonic $Y_{\ell m}(\theta, \phi)$ in the diatomic eigenfunction with the Wigner D-function $D^{J^*}_{M\Omega}(\phi, \theta, \chi)$.

Several theoretical advances followed concerning separation of linear and angular momentum coordinates using the D-function with no specific reference to the diatomic molecule (54; 24) before Davydov (27) used the D-function in the description of diatomic theory. Similarly, Rubin (132) utilized it for calculations of Hönl-London factors. Park and Hirschfelder (118) then used the D-function to separate two angular rotational coordinates in the diatomic eigenfunction but stopped short of using their Eq. (2.35) for all values of the third Euler angle. While Judd (61) and Mizushima (89) evaluated D-function's mathematical properties in terms of diatomic molecules, Zare et al. (171) explicitly used the D-function in the case (a) basis function.

3.4.1 The Wigner-Witmer Diatomic Eigenfunction

In this section, the Wigner-Witmer diatomic eigenfunction will be described based upon three fundamental symmetries and the geometrical symmetry of a molecule possessing precisely two nuclei. The system considered is free and conservative with respect to energy, linear momentum, and angular momentum. Thus, the time evolution operator $U(t, t_0)$ is a continuous unitary operator, and the total energy is a constant of the motion. If the time origin, t_0, can be associated with a physical

event, then the dependence of the eigenfunction on the physical variable t will be exactly separable. The spatial translation operator, $\mathcal{T}(\mathbf{R}, \mathbf{R}_0)$, is also a continuous unitary operator. $\mathcal{T}(\mathbf{R}, \mathbf{R}_0)$ represents the linear momentum, as the generator of translations in space. Now, in this conservative system, the total linear momentum is a constant of the motion. if the coordinates $\mathbf{R}_{\mathrm{CM}}$ of the center of mass can be introduced as physical variables of the system, then the total linear momentum is exactly separable. The rotation operator $\mathcal{R}(\alpha, \beta, \gamma)$, representing angular momentum as the generator of rotations, is a continuous unitary operator, and the total angular momentum is a constant of motion in our conservative system. However, the total angular momentum $\mathbf{J}(\phi, \theta, \chi)$ is not necessary exactly separable. $\mathbf{J}(\phi, \theta, \chi)$ would only be exactly separable if the system can be described by physical rotations ϕ, θ, and χ duplicating the angles of coordinate rotation α, β, and γ. Conveniently, for the diatomic molecule, the Euler angles of coordinate rotation α, β, and γ are also the angles of physical rotation describing the total angular momentum $\mathbf{J}$.

Beginning with the eigenfunction

$$\Psi_{nvJM}(\mathbf{R}_1, \mathbf{R}_2, \ldots, \mathbf{R}_N, \mathbf{R}_{\mathrm{a}}, \mathbf{R}_b, t) \equiv \langle \mathbf{R}_1, \mathbf{R}_2, \ldots, \mathbf{R}_N, \mathbf{R}_{\mathrm{a}}, \mathbf{R}_b, t \,|nvJM\rangle \qquad (3.19)$$

in which $\mathbf{R}_1, \mathbf{R}_2, \ldots, \mathbf{R}_N$ are the spatial coordinates of the N electrons and $\mathbf{R}_{\mathrm{a}}$ and $\mathbf{R}_b$ are those of the nuclei. J and M are the total angular momentum quantum numbers. In spectroscopic nomenclature, J and M are often replaced by F and M_F. The symbol n represents all other required quantum numbers except the vibrational quantum number v.

Now, symmetries between translation in time and space allow for the separation of t and the spatial coordinates of the center of mass $\mathbf{R}_{\mathrm{CM}}$. A two-body reduction of the motion of the nuclei requires placement of the coordinate origin a the center of mass of the nuclei, and then replaces $\mathbf{R}_{\mathrm{a}}$ and $\mathbf{R}_b$ with the internuclear vector $\mathbf{r}$. Of the $3N+7$ dynamical variables in the total eigenfunction of Eq. 3.19, the internal eigenfunction $\langle \mathbf{r}_1, \mathbf{r}_2, \ldots, \mathbf{r}_N, \mathbf{r} \,|nvJM\rangle$ will retain $3N+3$. Additionally, the axes of the translated

coordinates $\mathbf{r}_1, \mathbf{r}_2, \ldots, \mathbf{r}_N, \mathbf{r}$ are parallel to those of the original laboratory coordinates $\mathbf{R}_1, \mathbf{R}_2, \ldots, \mathbf{R}_N, \mathbf{R}_a, \mathbf{R}_b$.

Operation of the rotation operator $\mathcal{R}(\alpha, \beta, \gamma)$ on the internal eigenfunction yields

$$\langle \mathbf{r}_1, \mathbf{r}_2, \ldots, \mathbf{r}_N, \mathbf{r} \,|\mathcal{R}(\alpha, \beta, \gamma)|nvJM\rangle = \langle \mathbf{r}'_1, \mathbf{r}'_2, \ldots, \mathbf{r}'_N, \mathbf{r}' \,|nvJM\rangle \tag{3.20}$$

where primes denote rotated coordinates given by

$$\mathcal{D}(\alpha, \beta, \gamma) = \begin{bmatrix} \cos\alpha\cos\beta\cos\gamma - \sin\alpha\sin\gamma & \sin\alpha\cos\beta\cos\gamma + \cos\alpha\sin\gamma & -\sin\beta\cos\gamma \\ -\cos\alpha\cos\beta\sin\gamma - \sin\alpha\cos\gamma & -\sin\alpha\cos\beta\sin\gamma + \cos\alpha\cos\gamma & \sin\beta\sin\gamma \\ \cos\alpha\sin\beta & \sin\alpha\sin\beta & \cos\beta \end{bmatrix}. \tag{3.21}$$

$$\begin{bmatrix} x' \\ y' \\ z' \end{bmatrix} = \mathcal{D}(\alpha, \beta, \gamma) \begin{bmatrix} x \\ y \\ z \end{bmatrix}. \tag{3.22}$$

The effect of $\mathcal{R}(\alpha, \beta, \gamma)$ on the eigenfunction can be rewritten as

$$\langle \mathbf{r}_1, \mathbf{r}_2, \ldots, \mathbf{r}_N, \mathbf{r} \,|nvJM\rangle = \langle \mathbf{r}'_1, \mathbf{r}'_2, \ldots, \mathbf{r}'_N, \mathbf{r}' \,|\mathcal{R}^\dagger(\alpha, \beta, \gamma)|nvJM\rangle \tag{3.23}$$

$$= \sum_{\Omega=-J}^{J} \langle \mathbf{r}'_1, \mathbf{r}'_2, \ldots, \mathbf{r}'_N, \mathbf{r}' \,|nvJ\Omega\rangle \,\langle J\Omega \,|\mathcal{R}^\dagger(\alpha, \beta, \gamma) \,|JM\rangle \tag{3.24}$$

$$= \sum_{\Omega=-J}^{J} \langle \mathbf{r}'_1, \mathbf{r}'_2, \ldots, \mathbf{r}'_N, \mathbf{r}' \,|nvJ\Omega\rangle \, D^{J*}_{M\Omega}(\alpha, \beta, \gamma). \tag{3.25}$$

When the spherical coordinates of the internuclear vector $\mathbf{r} = \mathbf{r}(r, \theta, \phi)$ are introduced, the equation becomes

$$\langle \mathbf{r}_1, \mathbf{r}_2, \ldots, \mathbf{r}_N, r, \theta, \phi \,|nvJM\rangle = \sum_{\Omega=-J}^{J} \langle \mathbf{r}'_1, \mathbf{r}'_2, \ldots, \mathbf{r}'_N, r, \theta', \phi' \,|nvJ\Omega\rangle \, D^{J*}_{M\Omega}(\alpha, \beta, \gamma). \tag{3.26}$$

The internuclear distance r is unprimed on the right because it is a scalar. Because physical rotation ϕ and coordinate rotation α are both counter-clockwise rotations about the z axis, the physical angles ϕ' is given by

$$\phi' = \phi - \alpha. \tag{3.27}$$

Similarly, physical rotation θ and coordinate rotation β are counter-clockwise rotations about the first intermediate y axis of the total coordinate rotation.

$$\theta' = \theta - \beta. \tag{3.28}$$

Rotational symmetry gives us the option to view the molecule at any orientation. We will choose $\alpha = \phi$ and $\beta = \theta$.

$$\langle \mathbf{r}_1, \mathbf{r}_2, \ldots, \mathbf{r}_N, r, \theta, \phi \,|nvJM\rangle = \sum_{\Omega=-J}^{J} \langle \mathbf{r}'_1, \mathbf{r}'_2, \ldots, \mathbf{r}'_N, r \,|nvJ\Omega\rangle \, D^{J*}_{M\Omega}(\phi, \theta, \gamma). \tag{3.29}$$

The rotated coordinates of one of the electrons, we arbitrarily select the electron labeled 1, are expressed in cylindrical coordinates ρ'_1, ζ'_1, and χ'_1.

$$\langle \mathbf{r}_1, \mathbf{r}_2, \ldots, \mathbf{r}_N, r, \theta, \phi \,|nvJM\rangle = \sum_{\Omega=-J}^{J} \langle \rho'_1, \zeta'_1, \chi'_1, \mathbf{r}'_2, \ldots, \mathbf{r}'_N, r \,|nvJ\Omega\rangle \, D^{J*}_{M\Omega}(\phi, \theta, \gamma). \tag{3.30}$$

The chosen electron is distance ρ'_1 from the internuclear vector and signed distance ζ'_1 above or below the plane perpendicular to the internuclear vector and passing through the coordinate origin. The angle χ' describes rotation of this electron about the internuclear distance. Like the internuclear distance r, primes on ρ'_1 and ζ'_1 are unnecessary because they are scalars whose values are unchanged by coordinate rotation. Because χ'_1 and γ are rotations about the same axis, coordinate rotation changes, of course, the value of χ'_1, but this also means that this angle has a value χ_1 in laboratory coordinates. The coordinate rotation angle γ is chosen to make χ'_1

zero,

$$\chi_1' = \chi_1 - \gamma \tag{3.31}$$

The equation for the eigenfunction now reads

$$\langle \rho, \zeta, \chi, \mathbf{r}_2, \ldots, \mathbf{r}_N, r, \theta, \phi \, | nvJM \rangle = \sum_{\Omega=-J}^{J} \langle \rho, \zeta, \mathbf{r}_2', \ldots, \mathbf{r}_N', r \, | nv \rangle \, D^{J*}_{M\Omega}(\phi, \theta, \chi). \tag{3.32}$$

after the subscripts on ρ_1, ζ_1, and χ_1 have been dropped. Equation 3.32 now represents our Wigner-Witmer diatomic eigenfunction. The sum of $2J+1$ products of electronic-vibrational basis functions $\langle \rho, \zeta, \mathbf{r}_2', \ldots, \mathbf{r}_N', r \, | nv \rangle$ and total angular momentum basis functions $D^{J*}_{M\Omega}(\phi, \theta, \chi)$ give the total diatomic eigenfunction. The Born-Oppenheimer approximation separates the electronic-vibrational basis into the product electronic and vibrational basis functions. However, the separation of $D^{J*}_{M\Omega}(\phi, \theta, \chi)$ from the electronic-vibrational basis is exact. Thus, the Born and Oppenheimer (10) diatomic eigenfunction,

$$\langle \rho, \zeta, \chi, \mathbf{r}_2, \ldots, \mathbf{r}_N, r, \theta, \phi \, | nvJM \rangle \approx \sqrt{\frac{2J+1}{8\pi^2}} \langle \rho, \chi, \zeta, \mathbf{r}_2', \ldots, \mathbf{r}_N', r \, | nv \rangle \, D^{J*}_{M\Omega}(\phi, \theta, 0) \tag{3.33}$$

and the Wigner and Witmer (158) diatomic eigenfunction

$$\langle \rho, \zeta, \chi, \mathbf{r}_2, \ldots, \mathbf{r}_N, r, \theta, \phi \, | nvJM \rangle = \sum_{\Omega=-J}^{J} \langle \rho, \zeta, \mathbf{r}_2', \ldots, \mathbf{r}_N', r \, | nv \rangle \, D^{J*}_{M\Omega}(\phi, \theta, \chi), \tag{3.34}$$

$$\langle \rho, \zeta, \chi, \mathbf{r}_2, \ldots, \mathbf{r}_N, r, \theta, \phi \, | nvJM \rangle \approx \sum_{\Omega=-J}^{J} \langle \rho, \zeta, \mathbf{r}_2', \ldots, \mathbf{r}_N'; r \, | n \rangle \langle r | v_n \rangle \, D^{J*}_{M\Omega}(\phi, \theta, \chi). \tag{3.35}$$

3.4.2 Calculating the Line-strength

The line-strength was introduced by Equation 1.2. More explicitly, we now have

$$S(n'v'J'M', nvJM) = \sum_{M'=-J'}^{J'} \sum_{M=-J}^{J} \sum_{k=-q}^{q} \left| \langle n'v'J'M' | \hat{T}_k^{(q)} | nvJM \rangle \right|^2 \tag{3.36}$$

where the Wigner-Eckart theorem gives the transition moment,

$$\langle n'v'J'M' | \hat{T}_k^{(q)} | nvJM \rangle = \frac{1}{\sqrt{2J'+1}} \langle JMqk | J'M' \rangle \langle n'v'J' || \hat{\mathbf{T}}^{(q)} || nvJ \rangle, \tag{3.37}$$

in terms of the reduced matrix element $\langle n'v'J' || \hat{\mathbf{T}}^{(q)} || nvJ \rangle$. The Clebsch-Gordan coefficient in the above equation vanishes unless $k = M' - M$, and Eq. (3.36) can be rewritten as

$$S(n'v'J'M', nvJM) = \sum_{M'=-J'}^{J'} \sum_{M=-J}^{J} \left| \langle n'v'J'M' | \hat{T}_{M'-M}^{(q)} | nvJM \rangle \right|^2. \tag{3.38}$$

It is now apparent that the Clebsch-Gordan coefficient determines whether the transition is allowed or forbidden.

Thus far, the issue of spin has been neglected in our model of the diatomic molecule. Spin is introduced using the Clebsch-Gordon coefficient, and our total angular momentum $\mathbf{J}$ includes spin. Precisely, how we choose to include spin in $\mathbf{J}$ is a matter of preference. In any case, a mathematically complete basis function is required. Such basis functions consist of the Hund's case (a) basis ($\mathbf{J} = \mathbf{L}+\mathbf{R}+\mathbf{S}$) and Hund's case (b) basis ($\mathbf{J} = \mathbf{N} + \mathbf{S}$). Parigger and Hornkohl (104) explicitly presents both Hund's case (a) and (b) bases in this context, while providing the physical assumptions made on the model of the diatomic molecule for each case. However, from a mathematical stand point, the fact that each case represents a complete basis is enough. The physical interpretation does not change the spectral predictions.

Generally speaking, the calculation of diatomic line-strengths can be described as a four step process. First the upper and lower Hamiltonian matrices must be

compiled. Then the upper and lower Hamiltonians must be diagonalized. Once this is done, all the term values for which the transition moment does not vanish are computed. From this, the line-strengths can be computed.

The best available experimental data for the line positions (*i.e.*, vacuum wavenumbers) are used to determine the number and numerical values of parameters (*e.g.*, B_v, D_v, A_v, A_{D_v}, γ_v, $\epsilon_v \ldots$) for the upper and lower levels. These parameters are to be used to predict the positions $\tilde{\nu}_{ul}$ of the spectral lines. The spectral lines are then used to calculate the Hönl-London factors $S_{ul}(J', J)$. The non-vanishing of the Hönl-London factor determines whether the transition is allowed. This is the only selection rule applied. Using the obtained values for the rotational constants B_v and vibrational term values G_v for the upper and lower electronic states, the Rydberg-Klein-Rees (RKR) algorithm (see Appendix B) is implemented to compute the potential energy curves $V(\mathbf{r})$ for the upper and lower electronic states (134; 64; 130; 153).

Conveniently, the situation is sufficiently described by the radial one-dimensional Schrödinger equation,

$$\frac{d\psi^2}{d\mathbf{r}^2} + [E - V(\mathbf{r})]\,\psi(\mathbf{r}) = 0, \tag{3.39}$$

where ψ is the radial eigenfunction multiplied by $\mathbf{r}$. Using the potential energy curves for the diatomic molecule, the radial one-dimensional Schrödinger equation is numerically solved for each vibrational level of the upper and lower electronic states in order to find the vibrational eigenfunctions $\psi_v(\mathbf{r})$ (20; 14). The so-called Numerov-Cooley method is used to obtain the numeric solution. In this procedure, values of $\psi(\mathbf{r})$ are obtained at equally spaced values of $\mathbf{r}$ from the difference equation

$$Y_{i+1} + Y_{i-1} - 2Y_i = h^2\,(V_i - E)\,\psi_i, \tag{3.40}$$

where

$$Y_i = \left[1 - \frac{h^2}{12}\left(V_i - E\right)\right]\psi_i, \tag{3.41}$$

h is the separation between adjacent $\mathbf{r}$ values, and E is the trial eigenvalue. By arbitrarily assigning a small value to ψ_{n+1}, inward integration is begun using,

$$\psi_n = \psi_{n+1} e^{\mathbf{r}_{n+1}(V_n - E)^{\frac{1}{2}} - \mathbf{r}_n (V_n - E)^{\frac{1}{2}}}. \tag{3.42}$$

Once ψ_n no longer increases with decreasing n, the outward integration is performed. This process is initiated by arbitrarily assigning a small value to ψ_1 and imposing the boundary condition $\psi_0 = 0$. Letting m represent the number of steps of inward integrations, outward integration will continue until the value of ψ_m^{out} is determined. Then, each value of ψ_n is replaced with its value divided by either ψ_m^{in} or ψ_m^{out}. This serves to join the two curves into one with the normalization condition $\psi_m = 1$. Finally, the slopes of the two curves at the crossing point $\mathbf{r}_m$ are used to provide a correction δE, which is to be added to E. The correction is obtained using

$$\delta E = \frac{\left(-Y_{m-1} + 2Y_m - Y_{m+1}\right) h^{-2} + \left(V_m - E\right)\psi_m}{\sum_{i=1}^{n} \psi_i^2}. \tag{3.43}$$

This process is then repeated until successive values of E differ within a given tolerance. Once this condition is met, the values for ψ_i are then normalized such that

$$\int \psi^2 d\mathbf{r} = 1. \tag{3.44}$$

Using these eigenfunctions, the Franck-Condon factors

$$q(v', v) = \left|\langle v' | v \rangle\right|^2 = \left| \int \psi_{v'}(\mathbf{r})\, \psi_v(\mathbf{r})\, d\mathbf{r} \right|^2, \tag{3.45}$$

and r-centroids

$$\bar{\mathbf{r}}^{(k)}(v', v) = \frac{\langle v'|\mathbf{r}^k|v\rangle}{\langle v'|v\rangle} = \int \psi_{v'}(\mathbf{r})\, \mathbf{r}^k\, \psi_v(\mathbf{r})\, d\mathbf{r} \Big/ \int \psi_{v'}(\mathbf{r})\, \psi_v(\mathbf{r})\, d\mathbf{r}. \tag{3.46}$$

can be computed (145; 58). The diatomic line-strength is then calculated using a Taylor's expansion of the electronic transition moment $\mathcal{R}_{n',n}(\mathbf{r})$, combining the Franck-Condon factors $q(v', v)$, the r-centroids $\bar{\mathbf{r}}^k(v', v)$, and the Hönl-London factors $S(J', J)$ (see Eq. 1.2 for Hund's case (a) basis).

Chapter 4

Spectroscopy

The present chapter serves to detail the analysis of the data obtained by means of the experimentation of Chapter 2. As outlined in Chapter 3, when spectra is gathered for the purposes of analyzing atomic transitions, of principle interest is the width and integrated intensity of the spectral lines observed. The widths provide a measure of the Stark effect, which is the predominant contributor to spectral broadening. Here, the Stark effect occurs as an emitting atom is perturbed by the electric field of a nearby ion or electron. While the net electric field of the plasma can be negated, the orientation of the electric fields in a plasma is, in general, randomly distributed. The result on a given spectral line is known as Stark broadening, which is considered as a pressure broadening (43). This can lead to inferences concerning the electron density of the observed region of the plasma. The integrated intensity may then be used in a Boltzmann plot method to infer temperature. As far as LIP characterization by means of analyzing atomic line shapes by optical emission spectroscopy goes, this is the highest goal one may achieve.

For analysis utilizing diatomic spectral transitions, it is the relative intensities associated with the radiative transitions of the molecule that is of significance. As introduced in Chapter 1, inferences are made from observed diatomic spectral transitions by fitting the collected spectra with spectra computed from theory. The

fitting is performed using a Nelder-Mead algorithm (92). The Nelder-Mead fitting method allows for a multi-parameter fit. In our experiments, this allows for the inferences regarding the full-width at half maximum of spectral lines, the intensity and shape of the spectral baseline, as well as the temperature of the emitting molecules.

However, the Nelder-Mead method is not without its caveats. Because the algorithm uses the method of downhill simplices to find minima, the algorithm is suspect to falling into local minima along the way. To protect against this, it is useful to perform the fitting multiple times slightly varying the initial parameters. It is also suggested for the initial guesses for the varying parameters to be within 20 % of their perceived values. Also, the Nelder-Mead method can be quite time consuming when compared to a least squares fitting routine. However, this is typically not an issue unless several parameters are being fit at once, and in this case, convenience of the algorithm is perhaps still outweighing the waiting time.

4.1 Radio Frequency Thermal Plasma

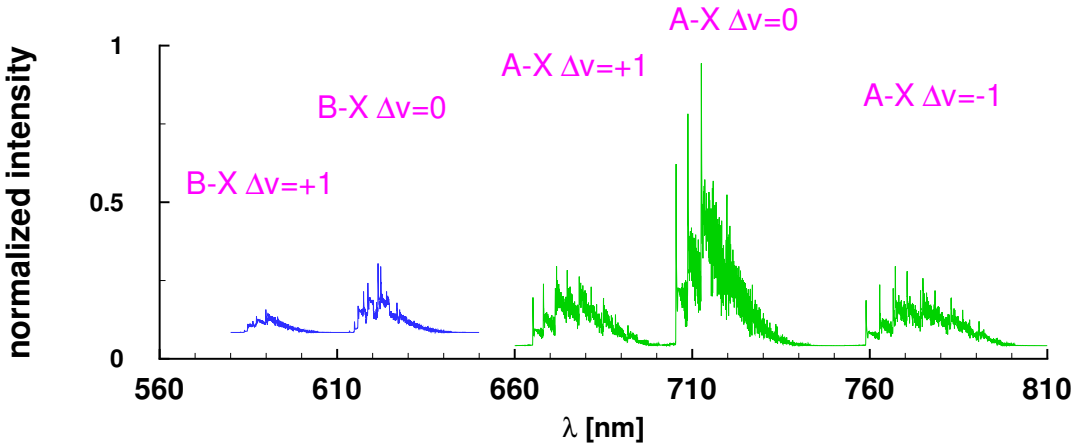

Figure 4.1: Computed $B-X$ and $A-X$ spectra using a FWHM = 0.08 nm. Inferred temperatures from spectral region containing $B-X$ and $A-X$ are, respectively, 3,800 and 3,030 K (112).

For the recorded spectrum from the RF thermal plasma at the Chemical Research Center of the Hungarian Academy of Science, rich emission spectra are obtained including atomic titanium lines near 400 nm, and it includes signatures or 'fingerprints' of TiO. By comparing Figures 2.2 and 4.1, near 620 nm TiO γ ′ Δv = 0 emissions can be identified, and near 710 nm the TiO γ Δv = 0 bands can be recognized. An attempt was made to fit portions of the $B-X$ and $A-X$ bands using our TiO line strength files. To account for contributions from other species between the 580 - 650 nm, a background of 0.084 was used in this region. For the 660 to 810 region, a background of 0.042 was used. Figure 4.1, displays the results. From the recorded spectrum in Fig. 2.2, we find a temperature of T = 3,800 K and T = 3,030 K for the $B-X$ and $A-X$ spectral regions, respectively. The error in temperature is due to several factors including, for example, accurate experimental determination of wavelength, spectral sensitivity, presence of other atomic and molecular species, variations in feeding of TiO_2. For the initial fitting illustrated in Fig. 4.2, we estimate the error from $A-X$ and $B-X$ fitting to be on the order of $\pm$ 1000 K and $\pm$ 2000 K, respectively.

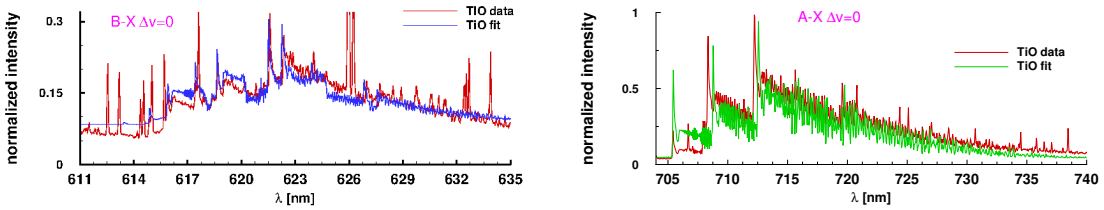

(a) TiO $B^3\Pi \rightarrow X^3\Delta$, Δv = 0 **(b)** TiO $A^3\Phi \rightarrow X^3\Delta$, Δv = 0

Figure 4.2: RF measured spectrum fit with (left) TiO γ', transitions corresponding to T = 3,800 K and (right) TiO γ transitions corresponding to T = 3,030 K (112).

Such error predictions are determined by use of Monte Carlo type simulations varying the assumed spectral baseline of computed spectra used for fitting. The ratios of some of the peak intensities of diatomic spectral transitions are temperature dependent. Consequently, the baseline used for inferring temperatures is a significant factor. The baseline adjusted spectra are then used to infer a temperature. This

process is sufficiently repeated creating a range of inferred temperatures for statistical analysis.

4.2 Laser Ablation Experiments

4.2.1 Measuring the TiO γ' Band

As noted in Section 2.2.1, some of the spectra collected show the presence of more than one TiO transition band. While Figure 2.6 illustrates recorded data from single-shot laser ablation in the 610 to 635-nm wavelength range, Fig. 2.7 displays computed spectra in range of 580 to 610 nm, and 610 to 640 nm. Although in principle the relative intensities can be used to determine relative prominence of the two transitions, this sort of investigation was not performed. Rather, attention was paid only to obtaining temperature inferences from the observed diatomic transitions. Accordingly, the gathered spectra are fit by the Nelder-Mead algorithm with computed spectra for the TiO γ', $B^3\Pi \rightarrow X^3\Delta$, $\Delta \mathrm{v} = 0$ transition. The Nelder-Mead method is used to find the best fitting temperature and spectral resolution, simultaneously. In order to protect the routine from falling into a local minimum, the fitting begins by assuming various starting points. Prior to fitting, certain measured spectra are subject to a sixth order Savitzky-Golay filter (137; 128).

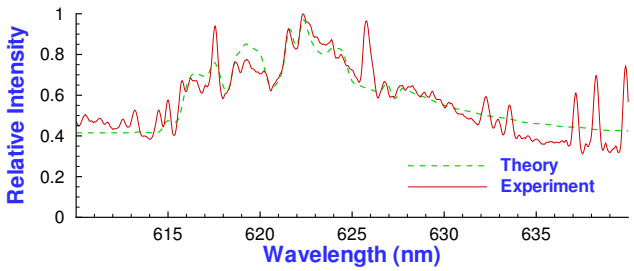

Figure 4.3: Spectra collected at t_{delay} = 52.2 μs fitted with calculated spectra representing the γ' system at T = 3600 $\pm$ 700 K at a spectral resolution of 0.4 nm (166).

Figure 4.3 and Figure 4.4 display measured spectra fit with computed spectra. The measured spectra shown have passed through a Savitzky-Golay filter (137; 128), allowing the spectral line shapes of interest to be more clearly visible. The experimental data represented in each figure is the result of a single shot measurement. The time delays are chosen based on previous TiO observations (28). The inferred temperature for the observed transitions in Figure 4.3 amounts to T = 3600 ± 700 K for a time delay of 52.2 μs using a window duration of 22 μs. For Figure 4.4, the inferred temperature is T = 4200 ± 800 K at a time delay of 72.2 μs using a 32 μs window duration. Monte Carlo simulations, using a uniform random number generator to vary amplitude, are used to calculate the 1-σ error (112). The estimated error from repeated measurements is found to be consistent with single shot variation.

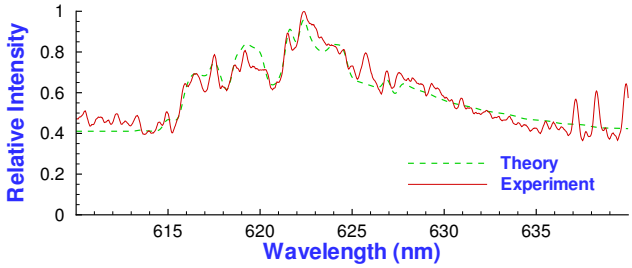

Figure 4.4: Spectra collected at t_{delay} = 72.2 μs fitted with calculated spectra representing the γ' system at T = 4200 ± 800 K at a spectral resolution of 0.4 nm (166).

Both figures display spectra fit with only the γ' transition band. As discussed, our computed spectra predict the presence of the γ, $A^3\Phi \rightarrow X^3\Delta$, transition band in this region, as well. The TiO α, $C^3\Delta \rightarrow X^3\Delta$, transition band also stretches into the region, as the Δv = -3 head is observed at 615.9 nm (16). The explanation for the relative prominence of the γ' band in this region is that the γ' Δv = 0 transition is being observed. The relative intensity is predicted to decrease as $|\Delta v|$ increases.

Despite the presence of various atomic lines in the measured spectra, the Nelder-Mead fit provided acceptable results. Notice that many of the atomic lines in Fig. 4.3 and Fig. 4.4 can be seen in the RF plasma emissions of Fig. 2.2. As should

be expected, these atomic line shapes are more prominent at earlier time delays. The spectra were also fit by excluding regions containing atomic transitions. These investigations resulted in comparable temperatures and did not significantly improve the tightness of the fit. Thus, errors in the inferred temperature are due primarily to uncertainty in the background. The 1-σ error calculated by adjusting the background is found to be on the order of 20 % of the indicated temperature. Therefore, a Savitzky-Golay filter will not significantly effect inferred temperature.

Also within these errors, the gate widths of 22 μs and 32 μs appear to have little effect on the inferred temperature. The detector measured nearly twice the signal at t_{delay} = 72.2 μs than it did at t_{delay} = 52.2 μs. This may have contributed to the elevated inferred temperature at a later time. However, use of gate widths on the order of 2 μs, as used in the following section, should allow us to further address the uncertainty in temperature.

4.2.2 Measuring the TiO γ Band

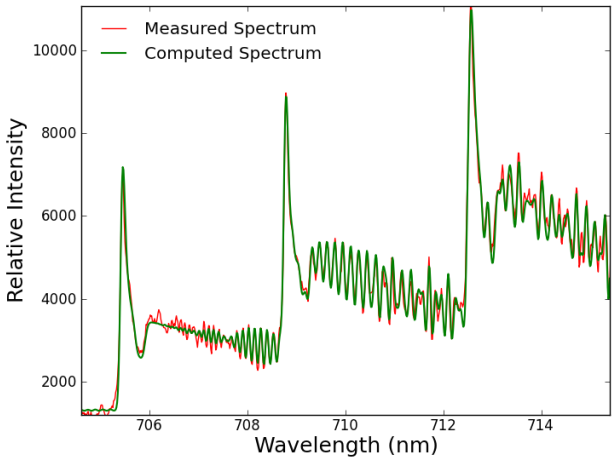

Figure 4.5: TiO $A^3\Phi \rightarrow X^3\Delta$ transition collected at a delay time t_{delay} = 95 μs with a 2 μs slit width. The fit results in an inferred temperature of 3335 K (167).

Figures 4.5 and 4.6 demonstrate the results of fitting computed spectra for the TiO γ transition band to a measured spectrum. Just as when fitting the TiO γ' band,

a reasonable temperature is inferred despite the significant presence of several atomic spectral lines. This is particularly the case for spectra gathered at the earlier time delays, as evident in Fig. 4.6. Recall that these atomic lines are observed with the 400 nm low-pass filter in position. If the filter were to be removed, many more lines would be present in the collected spectra of these earlier time delays.

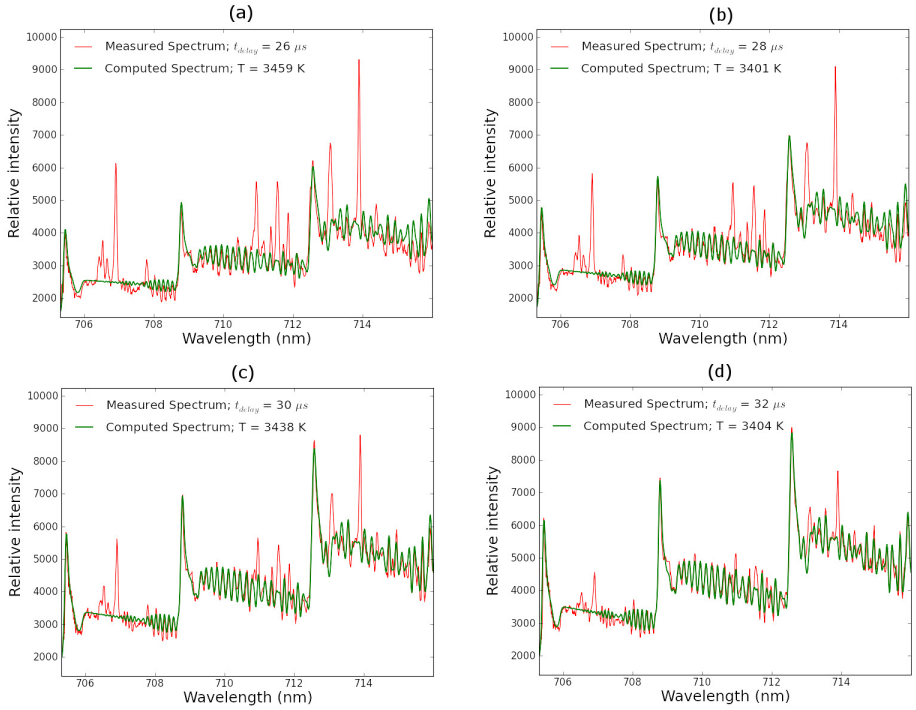

Figure 4.6: Experimentally collected spectrum along with a computed spectrum for the TiO $A^3\Phi - X^3\Delta$ transitions. Experimentally obtained spectra were collected using 2 μs gate widths.

A typical inferred temperature results from the fitting of computed spectra to a measured spectrum over the full wavelength range of the measurement. For this investigation, spectral regions consisting of predominantly rotational or vibrational structure are fit individually, as well. Figure 4.5 presents a measured spectrum along with the synthetic spectra used to infer temperature. Figure 4.7 illustrates the results of fitting the same measurement with only the predominantly rotational and vibrational regions of the computed synthetic spectra, respectively. The synthetic spectra used to infer temperature represents the TiO $A^3\Phi \rightarrow X^3\Delta$, $\Delta v = 0$ band.

The measured data shown corresponds to a delay time of 95 μs collected using a 2 μs window.

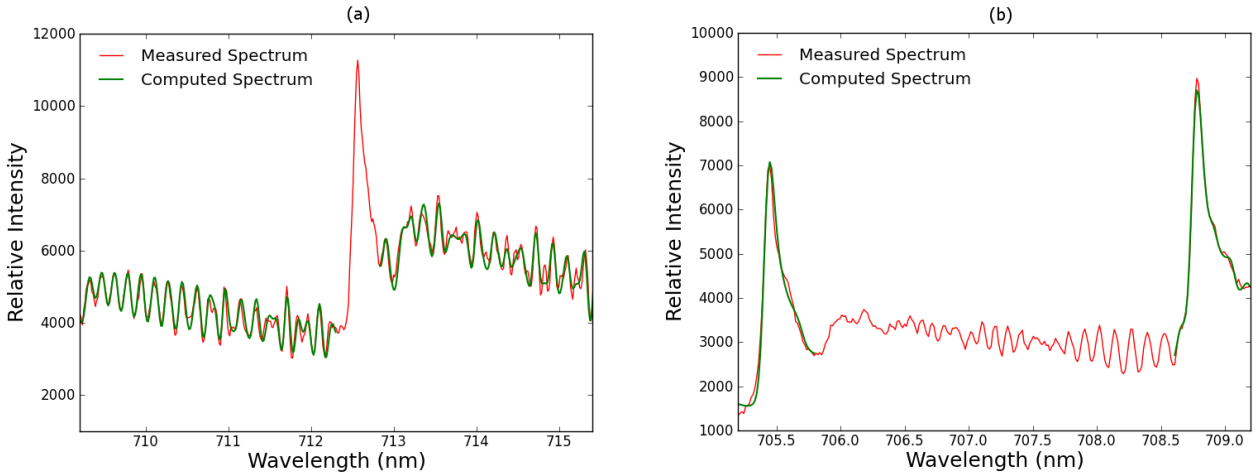

Figure 4.7: TiO $A^3\Phi \rightarrow X^3\Delta$ transition collected at a delay time $t_{delay} = 95$ μs with a 2 μs slit width. **(a)** The fit of the rotational structure results in an inferred temperature of 3216 K. **(b)** The fit of the vibrational structure results in an inferred temperature of 4178 K (167).

This particular measurement is noteworthy because it is observed that, for the third experimental run (see Section 2.2.2), the TiO spectra at the latest measurement times had less background contributions than at earlier delay times. This can be expected due to the overall decrease in signal with increasing time after optical breakdown. However, previous investigations concerning TiO in laser ablation plumes sometimes contain the presence of Ti atomic lines persisting at relatively long delay times of up to 60 μs (112; 166). As delay time further increases, diatomic spectra become less prominent and ultimately vanish. The measurements gathered for this region of the $A^3\Phi \rightarrow X^3\Delta$ band show minimal contributions from atomic spectral lines, and the TiO contributions remain discernable even at delay times such as this.

Tables 4.1, 4.2, and 4.3 present the inferred temperatures of the TiO $A^3\Phi \rightarrow X^3\Delta$, $\Delta\nu = 0$ system resulting from the Nelder-Mead fitting routine at various delay times following laser-induced breakdown. The first column of temperature values, labeled *T(K)*, represents the temperature inferred by fitting the entire range of the measured

Table 4.1: The table displays the inferred TiO temperatures for the $A^3\Phi \rightarrow X^3\Delta$ transition at various delay times in the region of 705-715 nm. Each measurement was collected using a 2 μs gate width.

$t_{delay}(\mu s)$	$T(K)$
26	4652 ± 360
30	4401 ± 273
34	4747 ± 438
38	4344 ± 376
42	4661 ± 304
50	3978 ± 222
54	3618 ± 160
58	3547 ± 221
62	3546 ± 117
66	3756 ± 174
70	3219 ± 172
74	3178 ± 98
78	3309 ± 75
82	3405 ± 42
86	3421 ± 40

spectrum with our computed spectra. The temperature values falling under columns labeled *Rotational T(K)* and *Vibrational T(K)* represent the inferred temperatures by analyzing only the region containing predominantly rotational and vibrational structure, respectively.

By examining Table 4.2, there appears to be a local minimum for the temperature inferences between 20 and 60 μs subsequent to laser-induced breakdown. The second experimental run presented in Table 4.3 provides a more resolved glimpse, with respect to delay time, at a spectral region where the first experimental run implies temperature decreasing to a local minimum. Figures 4.8 and 4.9 illustrate measurements made near the time delay corresponding to the local minimum.

For these measurements in particular, error analysis of the inferred temperatures is important. The error associated with each measurement is determined by re-fitting, using an arbitrarily fixed baseline. Each measurement is fit 1000 times, with a randomly chosen baseline within 25 % of the actual measured baseline. Since

Table 4.2: The table displays the inferred TiO temperatures for the $A^3\Phi - X^3\Delta$ transition at various delay times. Each measurement was collected using a 5 μs gate width. The rotational and vibrational temperatures were obtained by fitting portions of the spectra containing only rotational and vibrational transitions, respectively. An asterisk indicates that the signal to noise ratio of the measured spectrum is insufficient for a reasonable temperature inference.

$t_{delay}(\mu s)$	$T(K)$	$RotationalT(K)$	$VibrationalT(K)$
20	3985 ± 179	*	*
25	3339 ± 140	3308 ± 483	4226 ± 712
30	3189 ± 58	3009 ± 34	3140 ± 662
35	3075 ± 38	2660 ± 49	2721 ± 506
40	3026 ± 12	2642 ± 22	2519 ± 473
45	3140 ± 48	2894 ± 33	2435 ± 445
50	3437 ± 119	3196 ± 87	2682 ± 554
55	3802 ± 130	3874 ± 118	3081 ± 628
60	4269 ± 156	5332 ± 2013	3598 ± 511

Table 4.3: The table displays the inferred TiO temperatures for the $A^3\Phi - X^3\Delta$ transition at various delay times. Each measurement was collected using a 2 μs gate width. The rotational and vibrational temperatures were obtained by fitting portions of the spectra containing only rotational and vibrational transitions, respectively.

$t_{delay}(\mu s)$	$T(K)$	$RotationalT(K)$	$VibrationalT(K)$
26	3459 ± 235	3742 ± 906	5831 ± 2511
28	3401 ± 74	3505 ± 597	4823 ± 685
30	3438 ± 25	3830 ± 227	3956 ± 671
32	3404 ± 58	3394 ± 53	3312 ± 451
34	3297 ± 14	3091 ± 64	3055 ± 501
36	3309 ± 45	3101 ± 41	3191 ± 496

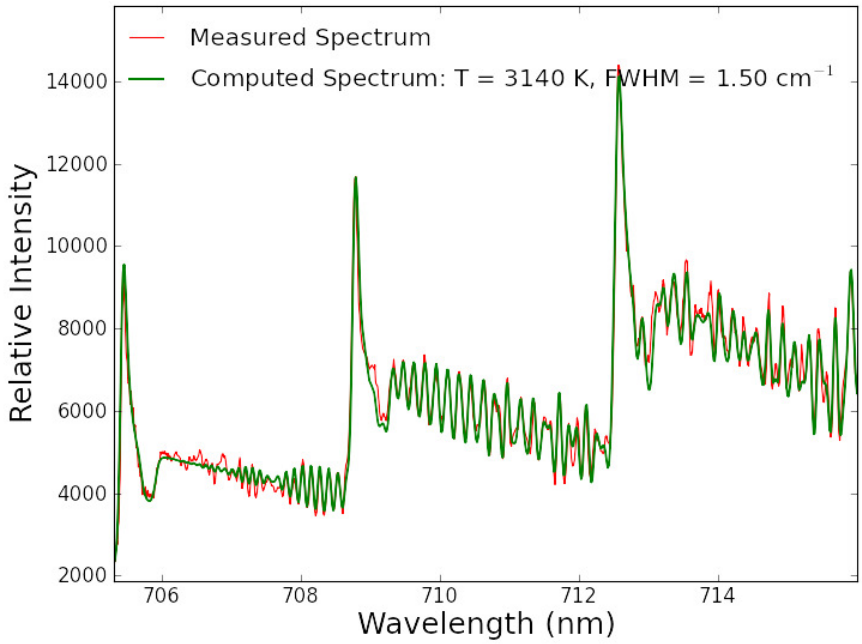

Figure 4.8: Experimentally collected spectrum along with a computed spectrum for the TiO $A^3\Phi - X^3\Delta$ transition corresponding to a temperature of 3140 K.

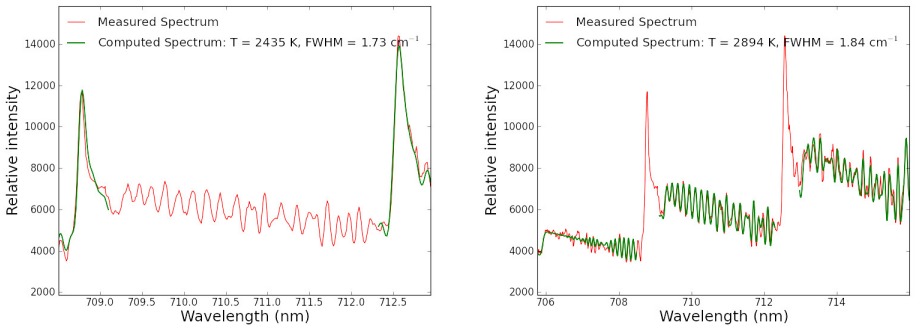

Figure 4.9: Experimentally collected spectrum along with a computed spectrum for the TiO $A^3\Phi - X^3\Delta$ transition corresponding to a temperature of (left) 2435 K and (right) 2894 K.

each measurement at a certain time delay is comprised of 100 individually collected laser events, variations among single shot events will usually be seen as variations in the baseline of the measurement. Since the peak-peak ratios of the observed spectral transitions factor into the determination of an inferred temperature, this type of background variation is meant to simulate fluctuations of shot-to-shot LIBS measurements and their effect on temperature inferences from a measured spectrum composed of several individual readings. The error associated with an inferred temperature by fitting a measured spectrum with complete computed diatomic molecular spectra by use of a Nelder-Mead algorithm is typically no greater than 10 %. The temperature ranges presented as error in this work are within 1-σ.

4.2.3 Error Analysis for Nelder-Mead Diatomic Spectrum Fitting

The observed radiative transitions of diatomic molecules are temperature dependent. By computing spectra from the current diatomic quantum theory and fitting the computed spectra to a measured diatomic molecular spectrum, the micro-plasma parameters of the measured spectrum can be inferred from the best fitting parameters of the model. For such tasks, a Nelder-Mead fitting routine is useful, as it provides a means of obtaining a nonlinear, multi-parameter fit. When using a fitting technique to infer temperatures for diatomic molecular transitions, the intensity ratios of observed spectral transitions are of particular importance.

While a Nelder-Mead fitting routine provides a technique for inferring the temperature for radiative transitions appearing in the spectra of diatomic molecules, the error associated with such inferences is unresolved. Possible reasons for temperature inferences to be inaccurate include: 'misfire' shots for multi-shot averages, excess noise for single and multi-shot measurements, and poor assumptions in the fitting routine. The Nelder-Mead method requires a trial value of the parameter to be determined before the method can initialize. This initial value is then randomly

varied until the fitting function is minimized. A poor choice for an initial trial value for the fitting parameter is one for which the fitting routine finds a local minimum and not the global minimum. By varying the initial trial value about an educated guess of the parameter value, this error can be avoided.

A 'misfire' shot, when considering multi-shot LIBS measurements, refers to a measurement in which the detector does not capture the desired event. This phenomenon typically occurs when the characteristic features of an element or molecule are not present in the measured spectrum. In instances such as these, the detector gathers a continuum of radiation emanating from the free-electron plasma. For multi-shot LIBS measurements, the result is an increase in the baseline of counts to which the spectral signal of interest is superposed.

Both single shot and to a lesser extent multi-shot LIBS measurements may be effected by excess noise in the measured spectrum. This type of noise in spectral measurements can originate from a number of different sources. It may be a result of shot-to-shot fluctuations in the observed plasma. For measurements with particularly low signal, the noise may be a consequence of the electronic features of the instrumentation. For multi-shot measurements the addition of noise from individual shots will tend to be distributed throughout the spectrum. Such noise will then result in an increased baseline offset to which the signal is superposed. For single shot measurements, there will be overall less signal in the measured data. This allows for noise in a spectrum to be more noticeable and capable of masking more subtle details of the radiative transitions of the atom or molecule of interest.

As a means to quantify the effects of noise in single shot and multi-shot LIBS experiments, Monte Carlo type simulations are utilized to adjust the baseline offset and to add noise throughout a measured spectrum, as the spectrum is repeatedly fit by the Nelder-Mead routine. For single-shot measurements, the addition of random synthetic noise across the spectrum is an appropriate means to simulate the effects of plasma fluctuations from shot-to-shot measurements and low signal-to-noise ratios. For multi-shot measurements, randomly adjusting the baseline offset of a spectrum

consisting of many single-shot measurements is adequate for simulating these same effects on the individual measurements.

4.2.4 Measuring Ultra-violet Ti Lines

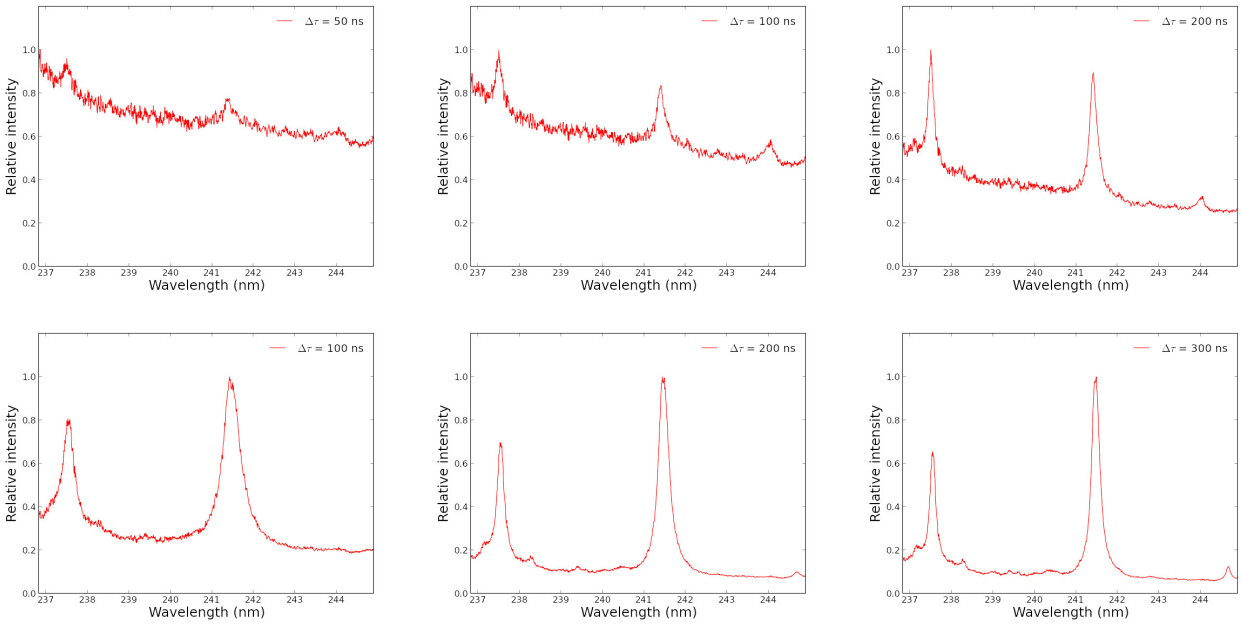

Figure 4.10: Top: Experimental data observing the Ti III and Ti II lines by laser ablation of a Ti target at 50, 100, and 200 ns after the laser pulse. Bottom: Experimental data observing the Ti III and Ti II lines by laser ablation of a Ti target at 100, 200, and 300 ns after the laser pulse.

Figure 4.10 provides some of the gathered spectra concerning the ultra-violet titanium lines in the spectral region of about 237-245 nm observed at time delays ranging from 50-300 ns after plasma formation. The spectral lines observed correspond to Ti III (237.49 nm and 241.40 nm) and Ti II lines (244.01 nm and 244.79 nm). After specifying the spectral baseline contribution, the integrated intensities of each line are determined. The integrated intensities are then used as a part of the Saha-Boltzmann plot method to infer temperature.

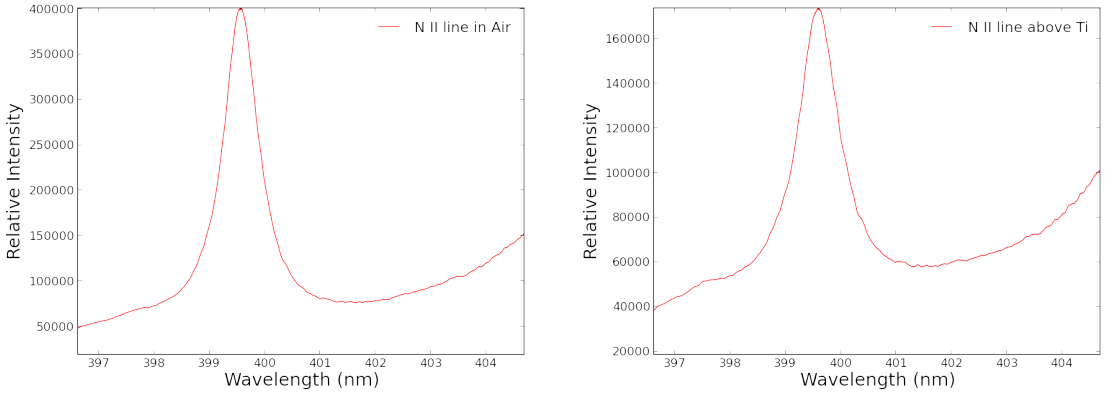

(a) N II line in Air **(b)** N II line above Ti

Figure 4.11: Observed N II 399.5 nm spectral line from LIP in air (left) and above the titanium surface (right) at $t_{delay} = 200$ ns.

Figure 4.11 represents the N II line at 399.5 nm observed at a time delay of 200 ns utilizing a 6 ns gate width. The emissions of the 399.5 nm N II line are observed both in LIP generated in laboratory and in the laser ablation plasma above a titanium surface. After specifying the spectral baseline contributions for each measurement, the spectral lines are fit with a Lorentzian line shape. From the Lorentzian profile, the FWHM are measured. The FWHM are then used to approximate the electron density. The N II line was observed in this manner for the same time delays as the titanium spectral lines. Tables 4.4 and 4.5 provide the measured widths and inferred electron densities for the N II line measured in air and above the titanium surface, respectively.

4.2.5 Measuring Spectra Along the Ablation Plume

Figure 4.12 illustrates the sort of measurements obtainable by implementing a two-dimensional ICCD as a means for gated detection. The image contains 128 horizontal spectra emitted from different heights along the ablation plume. The image is comprised of an accumulation of 200 laser events each measured at a time delay of 200 ns with a 6 ns gate width. To put the image in perspective, if the laser beam

Table 4.4: Widths of N II 399.5 nm lines and inferred electron densities N_e for specific time delays $\Delta\tau$. Data was collected in laser-induced plasma of laboratory air.

$\Delta\tau$ (ns)	N II width (nm)	n_e (10^{23} m^{-3})	$\Delta\tau$ (ns)	N II width (nm)	n_e (10^{23} m^{-3})	$\Delta\tau$ (ns)	N II width (nm)	n_e (10^{23} m^{-3})
20	1.29	43	120	0.97	32	220	0.68	23
40	1.44	58	140	0.89	30	240	0.64	21
60	1.33	44	160	0.82	27	260	0.61	20
80	1.20	40	180	0.76	25	280	0.58	19
100	1.07	36	200	0.71	24	300	0.56	19

Table 4.5: Widths of N II 399.5 nm lines and inferred electron densities N_e for specific time delays, $\Delta\tau$. Data was collected from resulting plasma of laser ablation of a titanium target.

$\Delta\tau$ (ns)	N II width (nm)	n_e (10^{23} m^{-3})	$\Delta\tau$ (ns)	N II width (nm)	n_e (10^{23} m^{-3})	$\Delta\tau$ (ns)	N II width (nm)	n_e (10^{23} m^{-3})
20	1.30	43	120	1.15	38	220	0.78	26
40	1.59	53	140	1.03	34	240	0.73	24
60	1.58	53	160	0.96	32	260	0.69	23
80	1.44	48	180	0.87	29	280	0.64	21
100	1.28	43	200	0.81	27	300	0.64	21

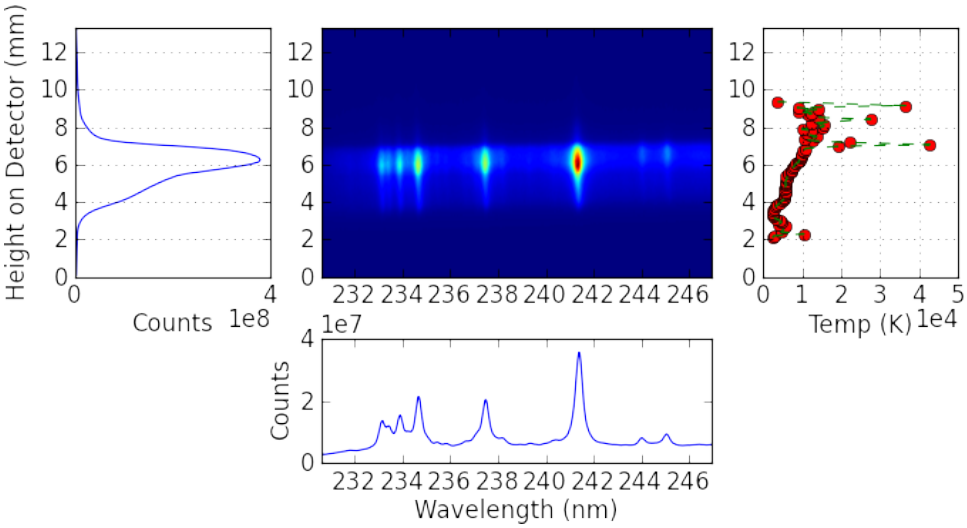

Figure 4.12: The above image represents data accumulated from 200 laser events at 200 ns after laser surface interaction.

were to be present, the beam would propagate vertically downward from the top of the image to the titanium sample resting just below the image.

The plot to the left of the image represents the intensity of the plume measured by the detector as a function of height on the detector. The plot immediately below the image represents the sum of the vertical pixels across the spectral region. It effective provides the information obtained if the two-dimensional ICCD were to be used as a linear diode array. The plot to the immediate right of the image represents the inferred temperatures by performing the Boltzmann plot method utilizing integrated intensity of the observed Ti III lines for each horizontal spectrum.

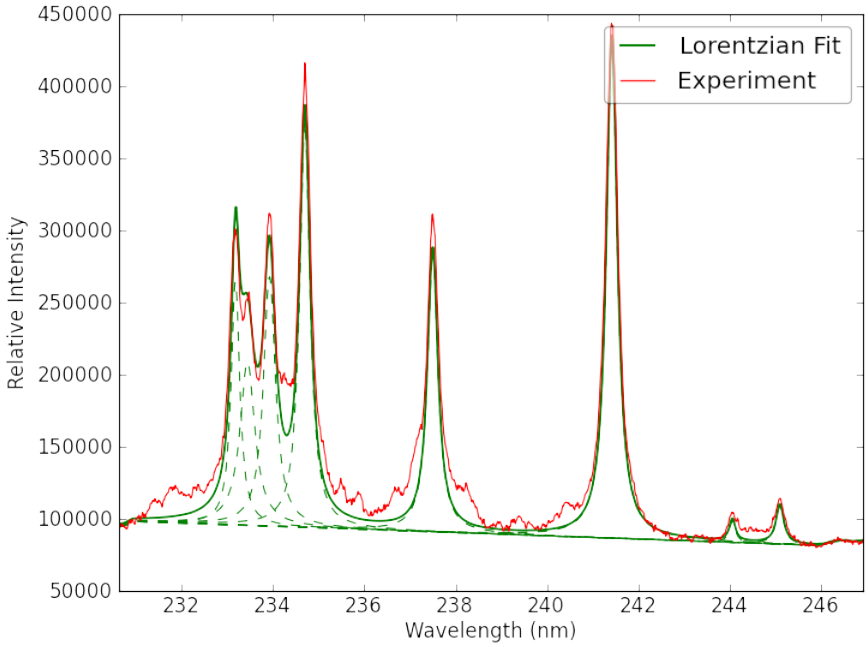

Figure 4.13: The above plot represents one horizontal slice of the image in Figure 4.12.

Figure 4.13 provides an arbitrarily selected horizontal slice of the image contained in Figure 4.12. Lorentzian profiles are fit to each Ti III and Ti II spectral line discernible. The integrated intensity of these Lorentzian line shapes for the Ti III lines are then used in the Boltzmann plot method to provide the temperatures presented

in Fig. 4.12. If this procedure is performed with the plot just below the image in Fig. 4.12 representing a linear diode measurement, the Boltzmann plot method for Ti III lines yields a temperature of 16,000 K.

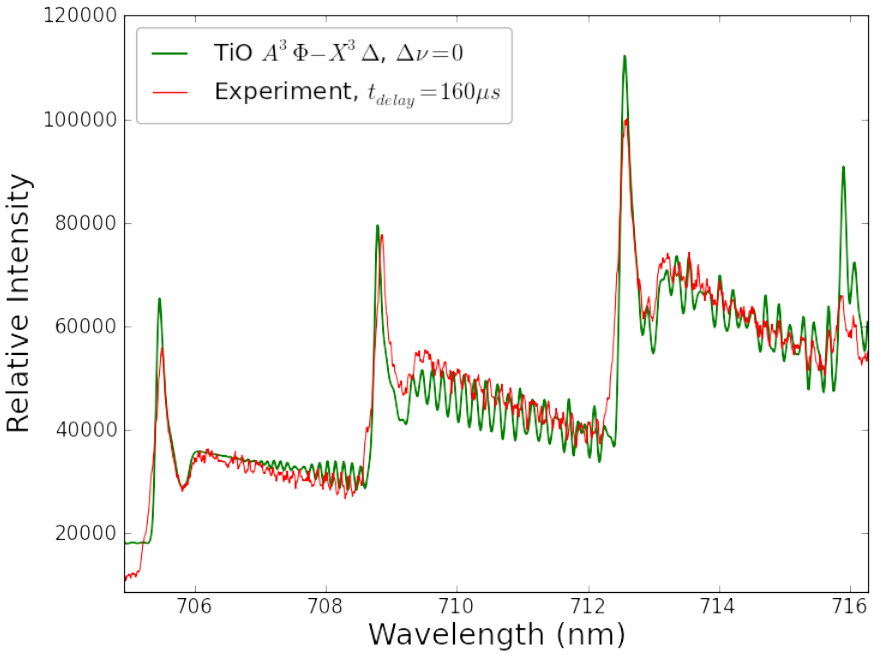

Figure 4.14: The above plot represents a horizontal slice of the image in Figure 4.22 fit with computed spectra corresponding to T = 3400 K.

Figures 4.15-4.24 present images for measurements made at t_{delay} = 20-200 μs following laser ablation of a titanium surface. Each image represents an accumulation of 200 individual laser events each collected with a 2 μs window. The intention of the measurements is to observe the TiO $A^3\Phi \rightarrow X^3\Delta$, Δv = 0 transition as a function of height along the plume at various delay times. Figure 4.14 represents an arbitrarily selected horizontal slice from the image in Fig. 4.22. Just as before experimentally obtained spectra are fit with computed spectra in order to infer temperature. The plot to the immediate right of each of the images in Fig. 4.15-4.24 provides the inferred temperatures as a function of height along the ablation plume.

By examining the plots below each image representing a linear diode array configuration, we notice just as before, that at the earlier time delays the diatomic spectral contributions are masked by the atomic contributions. For especially the measurement at $t_{delay} = 20$ μs, the computed TiO spectra does not fit well to the measured spectra. There are two likely causes for this. One explanation is that the TiO transitions due to recombination are just beginning to occur. Another explanation involves the signal to noise ratio of the measurements. When comparing horizontal spectra of a two-dimensional image to a spectrum produced by summing vertical pixels across a detector, the spectrum produced by summing over the height of the detector will contain significantly less noise. Thus, while TiO transitions containing many prominent atomic transition lines can be fit in a straight forward manner when observed with a linear diode array at a given time delay, the slices of a two-dimensional image at the same time delay may not be fit quite as readily.

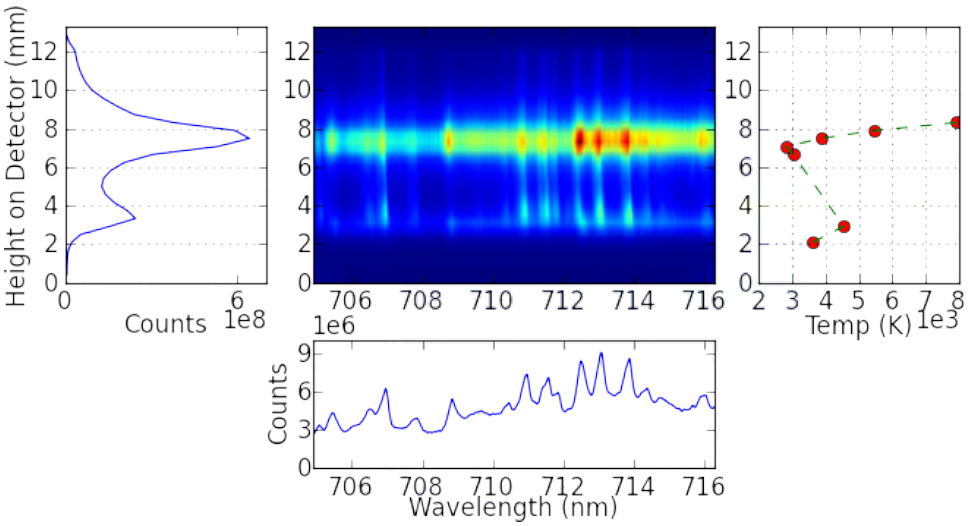

Figure 4.15: The above image represents spectra of laser ablation plasma above a titanium surface recorded at $t_{delay} = 20$ μs with a 2 μs gate width.

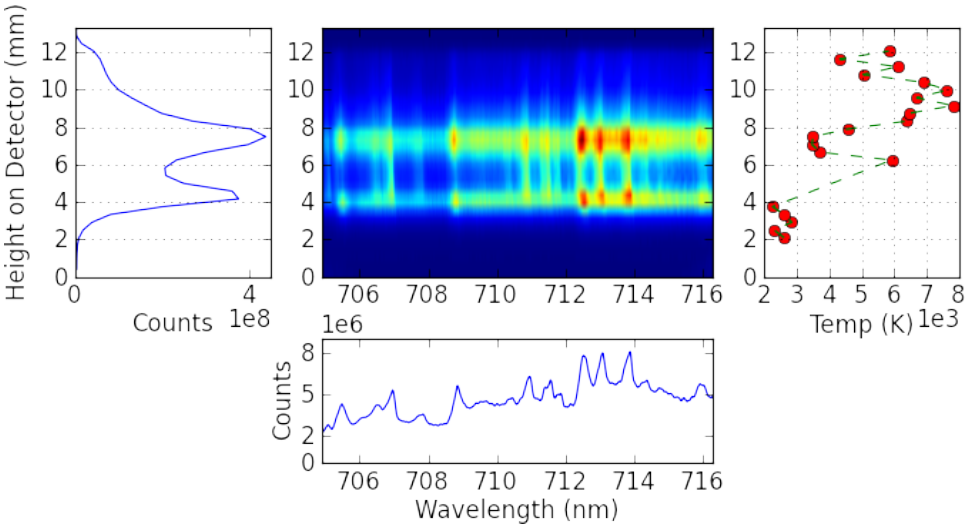

Figure 4.16: The above image represents spectra of laser ablation plasma above a titanium surface recorded at $t_{delay} = 40$ μs with a 2 μs gate width.

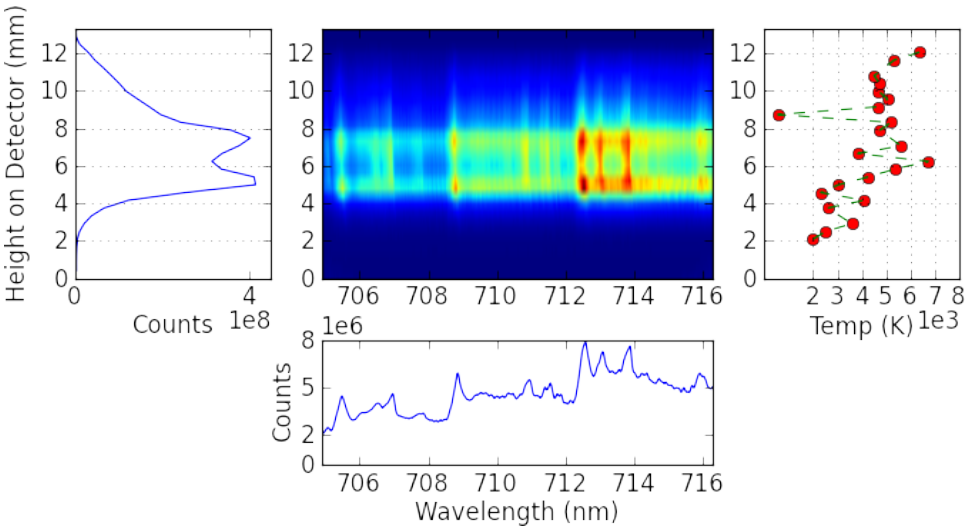

Figure 4.17: The above image represents spectra of laser ablation plasma above a titanium surface recorded at $t_{delay} = 60$ μs with a 2 μs gate width.

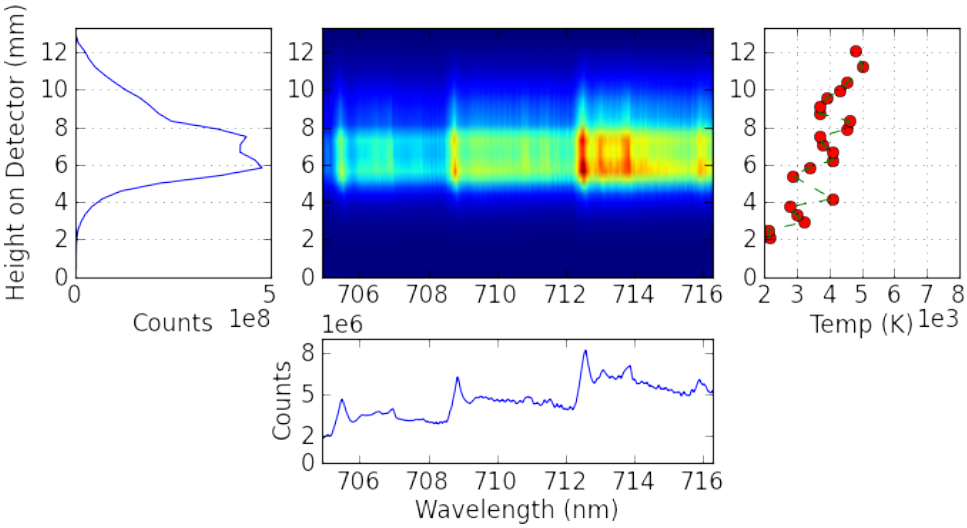

Figure 4.18: The above image represents spectra of laser ablation plasma above a titanium surface recorded at $t_{delay} = 80$ μs with a 2 μs gate width.

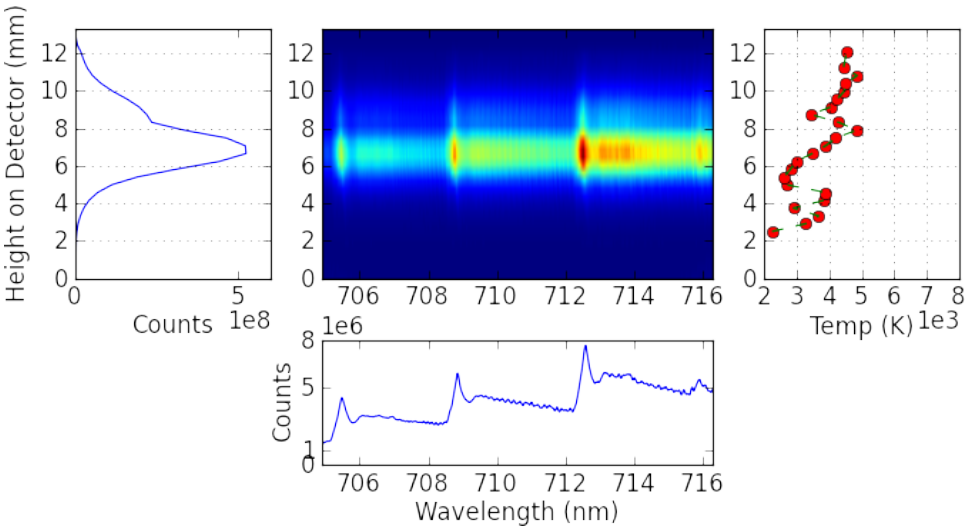

Figure 4.19: The above image represents spectra of laser ablation plasma above a titanium surface recorded at $t_{delay} = 100$ μs with a 2 μs gate width.

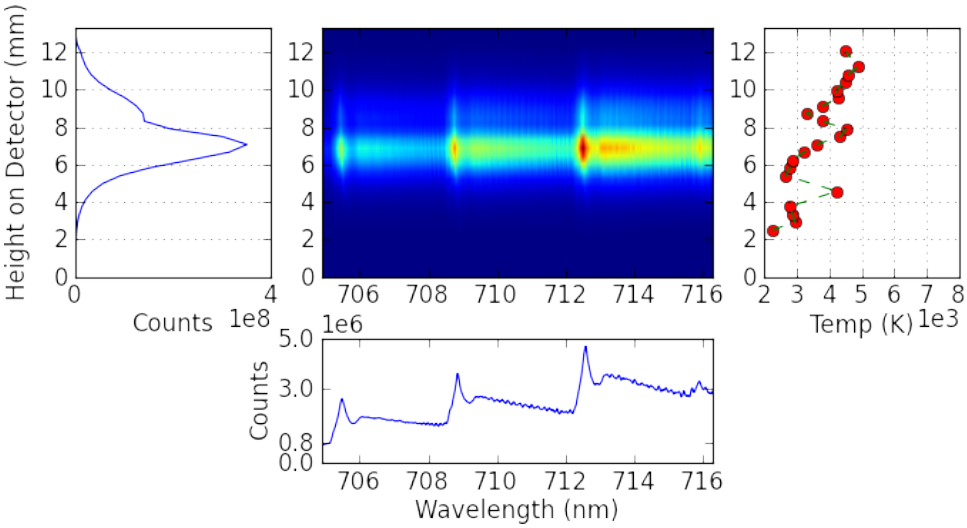

Figure 4.20: The above image represents spectra of laser ablation plasma above a titanium surface recorded at $t_{delay} = 120$ μs with a 2 μs gate width.

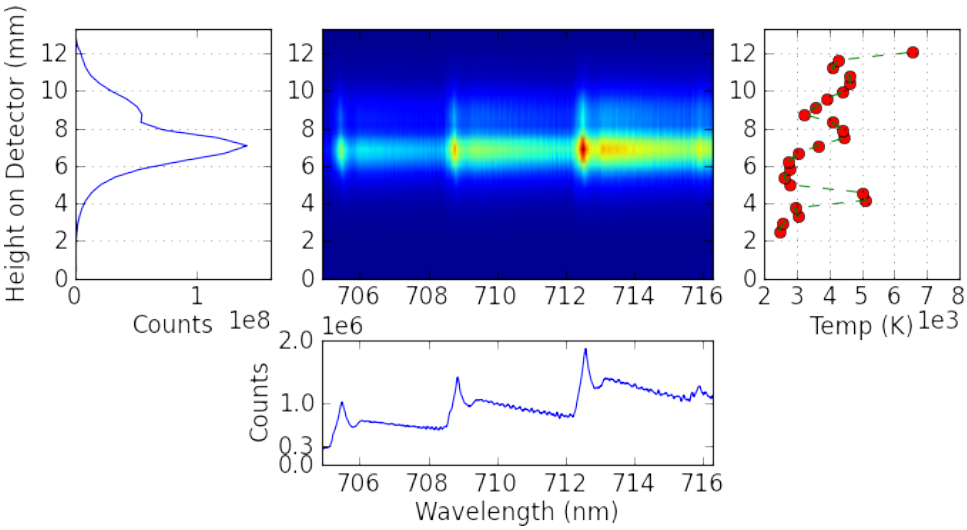

Figure 4.21: The above image represents spectra of laser ablation plasma above a titanium surface recorded at $t_{delay} = 140$ μs with a 2 μs gate width.

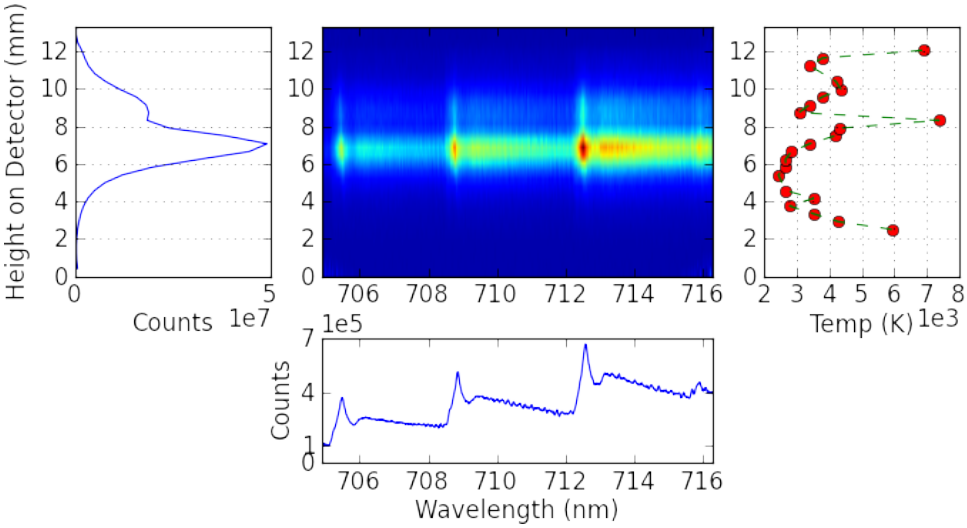

Figure 4.22: The above image represents spectra of laser ablation plasma above a titanium surface recorded at $t_{delay} = 160$ μs with a 2 μs gate width.

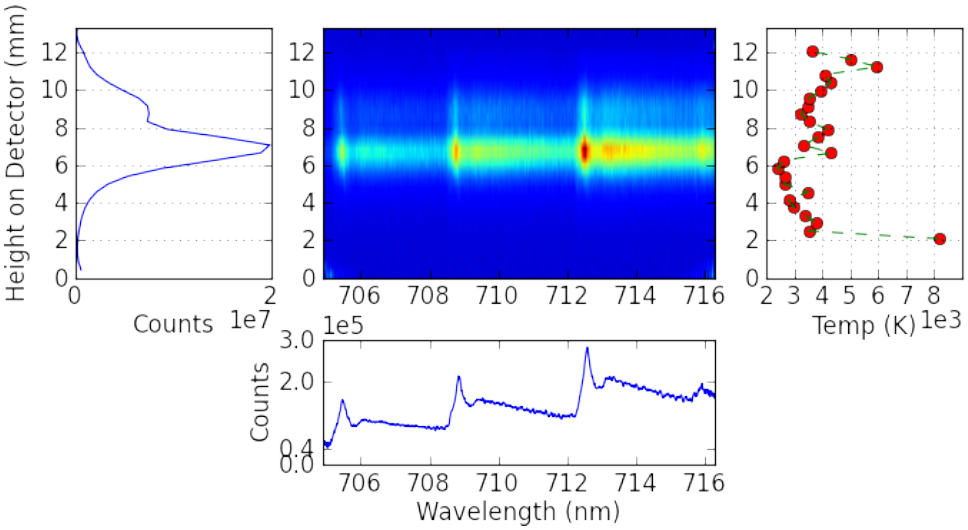

Figure 4.23: The above image represents spectra of laser ablation plasma above a titanium surface recorded at $t_{delay} = 180$ μs with a 2 μs gate width.

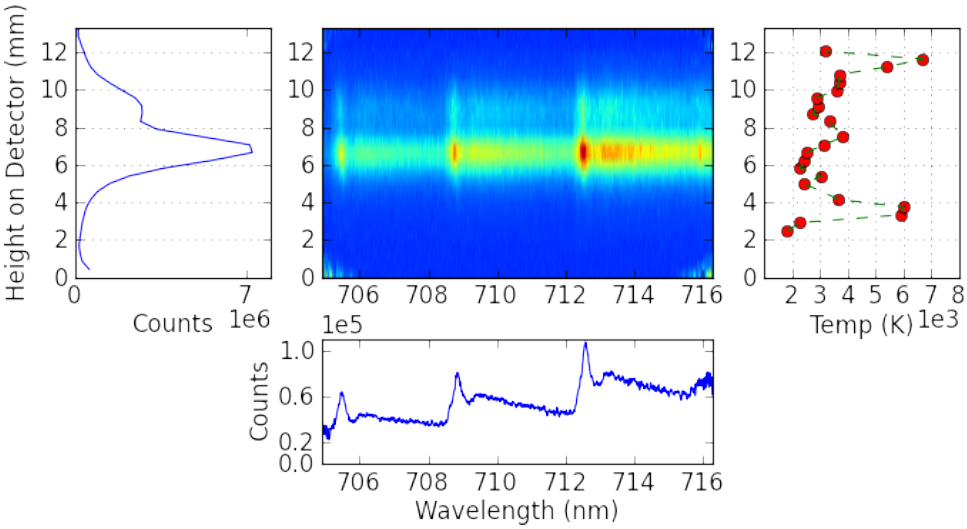

Figure 4.24: The above image represents spectra of laser ablation plasma above a titanium surface recorded at $t_{delay} = 200$ μs with a 2 μs gate width.

Chapter 5

Results

5.1 Laser Ablation of Ti within the First Microsecond

Research involving laser ablation of titanium has long been studied from the perspective of laser-induced breakdown spectroscopy (LIBS) (23; 159; 36; 170; 18; 12) and garners interest for various applications such as pulsed laser deposition for production of thin films and nanoparticles of use for solar cell technology, water and air purification, and industrial quality control (141; 5; 75; 96; 97; 41). While the processes involved in the evolution of plasma resulting from laser ablation of a titanium target are generally understood, a more comprehensive and detailed understanding of titanium particles in a laser ablation plume is desired (35). Of particular importance in this endeavor is the understanding of the plasma environment to which the titanium particles are exposed. A sufficient understanding would include the composition and temporal evolution of the titanium species in the plasma. The analysis of spectral lines emitted from plasma provides a means of quantifying the parameters of the plasma. Part of this research investigated various Ti II and Ti III emission lines located between 237 and 245 nm, as observed no later than 500 ns after plasma

formation. Table 5.1 presents information for the each of the Ti III and Ti II lines observed in this particular experiment.

Table 5.1: Atomic data for Ti III and Ti II lines that were observed (Kramida et al.).

λ (nm)	A (10^7 s^{-1})	E_l (cm^{-1})	E_u (cm^{-1})	Configurations	Terms
237.4986	40	41,704.27	83,796.86	$3p^6 3d4s$ - $3p^6 3d4p$	^{1}D - ^{1}P^o
241.3989	38	41,704.27	83,116.93	$3p^6 3d4s$ - $3p^6 3d4p$	^{1}D - ^{1}F^o
244.0165	5.1	12,628.8455	53,597.2664	$3d^3$ - $3d(^2D)4s4p(^3P^o)$	b^{2}D2 - w^{2}D^o
244.7897	0.37	12,758.2597	53,597.2664	$3d^3$ - $3d(^2D)4s4p(^3P^o)$	b^{2}D2 - w^{2}D^o

Ultra-violet Ti III and Ti II emission lines were measured in a laser ablation plasma as a function of delay time from plasma generation. These measurements were gathered at 10 ns intervals at delay times ranging from 20 to 100 ns after the laser event. The same spectral region was then examined at 20 ns intervals from 100 to 200 ns. Three additional measurements were then taken at 300, 400, and 500 ns times delays. The spectral widths of the lines were analyzed with respect to Stark broadening, in order to infer electron density. The Ti III and Ti II lines are further investigated by use of the Boltzmann plot method, to infer temperature.

The spectrometer was then adjusted in order to observe the N II line at 399.5 nm. The N II transition is measured in a titanium laser ablation plasma as well as in a laser-induced plasma of laboratory air at the same time intervals as before, ranging from 20 to 200 ns. The N II line was fit with a Lorentzian profile. The full-width at half maximum (FWHM) was then used to infer the electron density, n_e, of the plasma. Utilizing the temperatures obtained from the Boltzmann plot, the inferred electron densities for laser ablation plasma are compared with widths calculated by the MSE approach.

The N II 399.5 nm line was chosen because of the early plasma delay times involved in this investigation. Typically, the hydrogen Balmer series lines are an excellent

choice for inferring electron density (45). Their accuracy and availability in laser-induced plasma in laboratory air is well understood, with an accuracy of the inferred electron density utilizing the H_α line typically within 20 % and H_β inferences slightly more accurate (45). However, at the earliest delay times of this experiment, the Balmer lines proved to be so broad that the N II line became the more appropriate option.

Figure 4.10 illustrates six instances of collected data, observing the Ti III and Ti II lines, demonstrating the evolution of the laser ablation plasma. At a $\Delta\tau = 50$ ns, the Ti lines are hardly discernible, as the the plasma emissions are dominated by free electrons. As the plasma evolves in time, the two Ti III lines (237.49 nm and 241.40 nm) can be observed prior to the Ti II lines (244.01 nm and 244.79 nm). Also, the free electron radiation, providing the sloped baseline, gradually lessens, lowering this slope with increased time delay. The top row and the bottom row of Fig. 4.10 represent data collected from two separate experimental runs. Notice the presence of the Ti II at 244.01 nm in the top row is replaced by the Ti II line at 244.79 nm on the bottom row. As seen in Table 5.1, both Ti II lines share the same upper energy level. The difference in lower energy level is a factor of $J = 3/2$ and $J = 5/2$ for 244.01 nm and 244.79 nm Ti II lines (Kramida et al.), respectively.

Tables 4.4 and 4.5 list the measured widths of the N II 399.5 nm line along with the corresponding inferred electron densities for various delay times following laser-induced plasma formation in air and laser ablation of a titanium target in air, respectively. Due to the electrons provided by the Ti surface, the N II line observed in the laser ablation plasma of Ti indicates a greater electron density than the N II line observed in laser-induced plasma of air. However, the electron density inferred from each plasma behaves similarly as a function of time after the laser event. The first one or two data points for each inference do not follow the exponential decay of the other data points, but rather show a rapidly increasing electron density.

Figure 5.1 compares the inferred electron densities from the tables with an exponentially decaying function. The horizontal error bars of Fig. 5.1 represent

the 6 ns gate width used in the measurement. The vertical error bars represent ± 30 % of the inferred value, in accordance with previously estimated accuracy for electron density inferences utilizing the N II 399.5 nm line given the inferred electron temperatures of the current measurements (66).

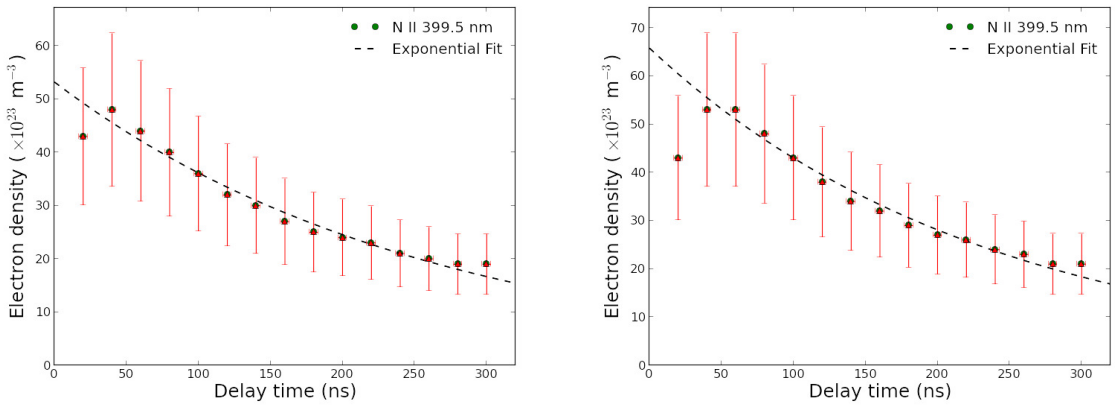

Figure 5.1: Left: Inferred electron density from measured Stark widths of the N II line at 399.5 nm as a function of delay time from laser-induced plasma formation in air. Right: Inferred electron density from measured Stark widths of the N II line at 399.5 nm as a function of delay time from titanium laser ablation plasma formation.

5.1.1 Gaunt Factor

The modified semiempirical (MSE) approach(46) based on electron impact Stark broadening(7; 6) is often useful in calculating the FWHM of a spectral line and its Stark shift(151; 29). When calculating the spectral line widths within the MSE approach,

$$w_{MSE} = n_e \frac{8\pi}{3} \left(\frac{\hbar}{m}\right)^2 \sqrt{\frac{2m}{\pi k_B T_e}} \frac{\pi}{\sqrt{3}} \left[\sum_{i'} \mathbf{R}^2_{i'i} g\left(\frac{E}{\Delta E_{i'i}}\right) + \sum_{f'} \mathbf{R}^2_{f'f} g\left(\frac{E}{\Delta E_{f'f}}\right)\right], \tag{5.1}$$

where n_e is the electron density, m is the electron mass, k_B is the Boltzmann constant, and T_e is the electron temperature. $E = \frac{3}{2} k_B T_e$ is the energy of the perturbing

electron, and $\Delta E_{j'j} = |E_{j'} - E_j|$ is the energy difference between levels j and j'. Here, $\mathbf{R}^2_{i'i}$ is the square of the coordinate operator matrix element summed over all components of the operator, the magnetic substates of total angular momentum J', and averaged over the magnetic substates of J. The matrix element can be estimated using the hydrogenic ion value between arbitrary levels j and j'

$$\mathbf{R}^2_{jj} = \sum_{j'} \mathbf{R}^2_{j'j} \approx \frac{1}{a_0}\langle j|\mathbf{r}^2|j\rangle = \frac{1}{2}\left(\frac{n_j}{Z}\right)^2 \left[5n_j^2 + 1 - 3l_j\left(l_j+1\right)\right]. \tag{5.2}$$

Commonly, an effective Gaunt factor,

$$\widetilde{g}(x) = 0.7 - \frac{1.1}{Z} + g(x), \tag{5.3}$$

is employed in addition to the Gaunt factor, $g(x)$(15). Note that in the above equations, $Z - 1$ provides the ionic charge. The Gaunt factor is suggested to have a lower threshold value of $g(x) = 0.2$(46; 29). Given the electron density and temperature values we have inferred for the plasma at our experimental delay times, our measured Stark widths show agreement with the MSE approach by assuming a Gaunt factor at threshold, $g(x) = 0.2$, without requiring an effective Gaunt factor.

Given our determined temperatures and line widths, our inferred electron density agrees with previous investigations into Stark broadening of the N II 399.5 nm line, providing accuracy between 20 and 30 % (66). The exponentially decreasing behavior of the inferred electron density as a function of time, implies a consistent exponential cooling for both the laser ablation plasma and the laser-induced plasma in air. The first one or two data points for the inferred electron density of the N II line imply the rapid contribution of free electrons in the plasma. This agrees with the observed Ti III and Ti II lines of the laser ablation plasma, as the free electron radiation is overpowering.

5.1.2 Boltzmann Plot

The electron excitation temperature, T_e, at early time delays following formation of the plasma was found by considering titanium atomic emissions. At early time delays following laser ablation of the titanium sample, Ti II lines are observed with emissions at 244.01 nm and 244.79 nm, and Ti III lines are observed with emissions at 237.49 nm and 241.40 nm. Using a combination of the Ti II and Ti III lines, Saha-Boltzmann plotting methods may be used to determined the electron temperature, which relates the integrated intensity of each emission line to the electron excitation temperature. The integrated intensities were determined by fitting Lorentzian line profiles to each titanium emission. Using this method, initial temperature calculations are found to be in excess of T_e = 40,000 K for a time delay of 200 ns following laser-induced breakdown. Further measurements and analysis would be required to determine the temperature as function of delay time due to uncertainties in the sensitivity of the detector in the specified spectral region and calibrations of background emission contributions. Despite these limitations the order of magnitude temperature of 40,000 K may be determined within an accuracy of 10,000 K.

For the gathered titanium emission lines, the Boltzmann plot method was successful in providing electron temperature estimates, but such estimates contained considerable error. The error is mainly attributed to inaccuracies in the sensitivity corrections made for the detector at the wavelength region. When compared with previous, reliable sensitivity corrected measurements made by this detector, the lower wavelength region of our collected Ti spectra typically displays a factor of two smaller sensitivity.

When compared to a similar investigation into Ti III Stark broadening (15), the current experiment resulted in greater electron excitation temperatures and lesser inferred electron densities. Considering the differences in the laser excitation energy and the spectral grating implemented in each investigation, the experimental data appears to agree. However, the previous investigation utilizes the effective Gaunt

factor of Equation (3) to enhance the threshold Gaunt factor (15). For the current investigation, comparison with calculated values of Stark widths from the MSE approach demonstrate agreement when replacing an effective Gaunt factor with simply the Gaunt factor value at threshold. The semi-empirical Gaunt factor, at threshold, has been interpreted as accounting for the first truly quantum mechanical effect in electron impact broadening (46). Further comparison with the MSE approach was made utilizing Table IV (151) reported by Tankcosić et al. (151), and it also shows agreement.

5.1.3 Two-dimensional Analysis

While the Boltzmann plot technique was used to provide electronic excitation temperature inferences from the ultra-violet titanium lines observed, there were significant problems. One being that there were only two Ti III lines available in the collected spectra. This requires the integrated intensity to be calculated with great accuracy or considerable error can be introduced. Even when the Saha-Boltzmann plot technique is used, considering the Ti III as well as the Ti II lines, there are issues. Despite adding two more data points by including the Ti II lines in a Saha-Boltzmann method, the two Ti II lines observed are so near each other in energy level that they hardly contribute accuracy to the temperature inference.

When examining the spectra obtained by two-dimensional imaging, as seen in Figure 4.12, more Ti III lines become available in the spectra. This is made apparent in Figure 4.13. Table 5.2 provides information for each of the Ti III lines observed in the two-dimensional analysis. Using the data obtained from the image in Fig. 4.12, six Ti III spectral lines can be used in a Boltzmann plot technique. When comparing the temperatures plotted in Fig. 4.12 with the temperatures inferred in Section 5.1.2, we see that typically much lower temperature are inferred from similar experimental conditions.

Table 5.2: Atomic data for Ti III lines that were observed (Kramida et al.).

λ (nm)	A (10^7 s^{-1})	E_l (cm^{-1})	E_u (cm^{-1})	Configurations	Terms
233.166	12	38,064.35	80,939.19	$3p^6 3d4s$ - $3p^6 3d4p$	^{3}D - ^{3}P^o
233.434	7.7	38,198.95	81,024.47	$3p^6 3d4s$ - $3p^6 3d4p$	^{3}D - ^{3}P^o
233.9	30	38,198.95	80,939.19	$3p^6 3d4s$ - $3p^6 3d4p$	^{3}D - ^{3}P^o
234.678	33	38,425.99	81,024.47	$3p^6 3d4s$ - $3p^6 3d4p$	^{3}D - ^{3}P^o
237.4986	40	41,704.27	83,796.86	$3p^6 3d4s$ - $3p^6 3d4p$	^{1}D - ^{1}P^o
241.3989	38	41,704.27	83,116.93	$3p^6 3d4s$ - $3p^6 3d4p$	^{1}D - ^{1}F^o
244.0165	5.1	12,628.8455	53,597.2664	$3d^3$ - $3d(^2D)4s4p(^3P^o)$	b^2D2 - w^2D^o
244.7897	0.37	12,758.2597	53,597.2664	$3d^3$ - $3d(^2D)4s4p(^3P^o)$	b^2D2 - w^2D^o

By comparing the inferred temperature of 16,000 K obtained by analyzing the spectrum produced by summing the vertical pixels of the ICCD with the temperature inferences along the height of the detector, we notice that inferred temperature from the sum corresponds to the temperature of the hottest region of the plasma. This finding provides insight into all previous measurements obtained using the intensified linear diode array (model 1460 Princeton Applied Research detector). Also, of interest is that we measure a temperature increase in the plasma as a function of height from the ablation surface. This will continue to be the case when discussing temperature inferences using the TiO transitions as a function of height along the plume in the subsequent section.

5.2 Line Strength Files for Titanium Monoxide

In this work, we report results of electric dipole line strengths for the $A^3\Phi - X^3\Delta$ and $B^3\Pi - X^3\Delta$ band systems of TiO. Values of the diatomic parameters are obtained by fitting model Hamiltonians for upper and lower states to best available line position measurements. The fitted parameters were then used to compute accurate line positions, *i.e.*, vacuum wavenumbers, and Hönl-London factors for all lines in a band, not just those experimentally known with high accuracy. The Rydberg-Klein-Reese

(RKR) procedure (134; 64; 130; 153; 152) was not applied to determine the potential $V(r)$ from vibrational constants ω_e, $\omega_e x_e$, $\omega_e y_e$, *etc.*, and rotational constants B_e, α_e, γ_e, *etc.* Here, Franck-Condon factors and r-centroids are computed using Morse potential chosen to best fit the low lying vibrational levels. The electronic transition moments were taken from the most recently reported *ab initio* computations for $A-X$, $B-X$, and $E-X$ transitions.

In this section, we present an overview of the computation of TiO line strength tables. First, the framework is discussed for generating our accurate database for selected diatomic transitions. Second, example computations are presented of TiO γ, γ', and $E-X$ 0-0 bands. Comparisons with experimental data are included.

5.2.1 Line Strength File Framework

Quantities like Einstein coefficients, oscillator strength, and cross section are standard terms in spectroscopy. One such example is the Einstein A coefficient,

$$A_{ul} = \frac{2\omega_{ul}^3}{3\varepsilon_0 h c^3 g_u} S_{ul}, \tag{5.4}$$

where ω_{ul} is the transition frequency ($\omega_{ul} = 2\pi\nu_{ul}$), g_u is the upper level degeneracy, h is Planck's constant, c is the speed of light, and ε_0 is the vacuum permittivity. However, when computing diatomic spectra it is the line-strength that is typically used to provide the information contained in these other spectroscopic terms. The line-strength S_{ul} is defined as

$$S_{ul} = \sum_u \sum_l |\langle u|T_k^{(q)}|l\rangle|^2. \tag{5.5}$$

Here, $T_k^{(q)}$ is the kth component of the irreducible tensor of order q responsible for the transition, and the summations account for all upper (u) and lower (l) states that produce that particular spectral line. Diatomic spectra are computed with line strength data.

A diatomic spectral line is the result of a radiative transition between an upper state $n'v'J'$ and a lower state nvJ, where n is the electronic quantum number (n actually represents a collection of electronic quantum numbers), v is the vibrational quantum number, and J is the total angular momentum quantum number. The diatomic line strength can be written as the product of the electronic-vibrational strength $S_{ev}\left(n'v', nv\right)$ which has units of line strength, and the unitless rotational line strength $S\left(J, J'\right)$ or Hönl-London factors (56),

$$S\left(n'v'J', nvJ\right) = S_{ev}\left(n'v', nv\right) S\left(J, J'\right). \tag{5.6}$$

The eigenfunction for a diatomic molecule having N electrons is

$$\langle \mathbf{r_1 r_2} \cdots \mathbf{r_{N-1}} \rho \zeta r \phi \theta \chi | nJM \rangle = \sum_{\Omega=-J}^{J} \langle \mathbf{r'_1 r'_2} \cdots \mathbf{r'_{N-1}} \rho \zeta r | n \rangle D^{J*}_{M\Omega}\left(\phi, \theta, \chi\right), \tag{5.7}$$

where $\mathbf{r_1 r_2} \cdots \mathbf{r_{N-1}} \rho \zeta r \phi \theta \chi$ are electronic coordinates and r, θ, and ϕ are the spherical polar coordinates of the internuclear vector. The primes denote coordinates in a coordinate system of the rotating molecule attached to the molecule in such a way that physical rotations ϕ, θ, and χ are Euler angles ϕ, θ, and χ. The symbol $D^{J*}_{M\Omega}\left(\phi, \theta, \chi\right)$ is the complex conjugate of the Wigner D-function, J is the quantum number of the total angular momentum $\mathbf{J}$, M is the quantum number for the z component of $\mathbf{J}$, and Ω is the quantum number for the z' component of $\mathbf{J}$. Equation 5.2.1 indicates that in principle the diatomic Hamiltonian matrix shows dimensions of $(2J+1) \times (2J+1)$, but in practice the Hamiltonian matrix is smaller than that. For example, we were able to model successfully the TiO $B^3\Pi$ eigenfunctions as the eigenvectors of 9×9 matrices for all J values. The (one photon) Hönl-London factors are given by

$$S\left(J', J\right) = \left| \sum_{i=1}^{N_u} \sum_{k=1}^{N_l} f_{J'_i} \langle J \Omega_k 1, \Omega'_i - \Omega_k | J' \Omega'_i \rangle f_{J_k} \right|^2, \tag{5.8}$$

where the upper Hamiltonian matrix has dimensions $N_u \times N_u$ and has eigenvectors $f_{J_i'}$, while the lower Hamiltonian has dimensions $N_l \times N_l$ and has eigenvectors f_{J_k}. The symbol $\langle J\Omega_k 1, \Omega_i' - \Omega_k | J'\Omega_i' \rangle$ denotes the Clebsch-Gordan coefficient.

In the Born-Oppenheimer approximation, the electronic-vibrational eigenfunction can be written as

$$S_{ev}\left(n'v', nv\right) = \left|\mathcal{R}_{n'n}\left(r\right)\langle v'|v\rangle\right|^2, \tag{5.9}$$

where $\mathcal{R}_{n'n}\left(r\right)$ is the electronic transition moment that is an explicit function of the internuclear distance r. In the Born-Oppenheimer approximation the electronic eigenfunctions are parametric functions of r. The symbol $\langle v'|v\rangle$ is called the overlap integral

$$\langle v'|v\rangle = \int_0^\infty \Psi_{v'}\left(r\right)\Psi_v\left(r\right)dr. \tag{5.10}$$

Ab initio quantum chemistry computations have progressed to the point where computed $\mathcal{R}_{n'n}\left(r\right)$ functions are considered more reliable than those experimentally determined. With a Taylor series expansion of the electronic transition moment,

$$\mathcal{R}_{n'n}\left(r\right) = a_0 + a_1\left(r - r_0\right) + a_2\left(r - r_0\right)^2 + \ldots, \tag{5.11}$$

where $a_{i=0,1,2,\ldots}$ are constant coefficients, the electronic-vibrational strength becomes

$$S_{ev}\left(n'v', nv\right) = \left|a_0 + a_1\bar{r}_{v'v}^{(1)} + a_2\bar{r}_{v'v}^{(2)} + \ldots\right|^2 q_{v'v}, \tag{5.12}$$

in which the i-th translated r-centroid is

$$\bar{r}_{v'v}^{(i)} = \frac{\langle v'|\left(r - r_0\right)^i|\rangle}{\langle v'|v\rangle}. \tag{5.13}$$

The sqaure of the overlap integral in Eq. 5.2.1 is called the Franck-Condon factor,

$$q_{v'v} = \langle v'|v\rangle^2. \tag{5.14}$$

We use translated r-centroids with their origin given as

$$r_0 = \frac{r'_e + r_e}{2}, \tag{5.15}$$

the average of the upper and lower classical equilibrium internuclear distances.

The so-called r-centroid approximation is easily avoided, therefore, we do not use it. Use of un-translated r-centroids would require computation with high precision to avoid round-off errors. Moreover, un-translated r-centroids conceal the $\bar{r}^{(i)}_{v'v} \simeq \left[\bar{r}^{(1)}_{v'v}\right]^i$ inaccuracies. After computation of vibrational eigenfunctions $\Psi_{v'}(r)$ and $\Psi_v(r)$, we find the first r-centroid $\bar{r}^{(1)}_{v'v}$ and Franck-Condon factor $q_{v'v}$, and then calculate higher order r-centroids $\bar{r}^{(i>1)}_{v'v}$. The majority of our computed Franck-Condon factors agree within a few % with the ones in Table 9 of Ref. (129).

In accepted practice, the spectroscopic vibrational term values G_v and the rotational constants B_v are used in an algorithm developed by Rydberg, Klein, and Rees (RKR) to evaluate the potential energy curves $V(r)$ for the upper and lower electronic states. A one-dimensional Schrödinger equation with the potential $V(r)$ is then numerically solved to obtain the upper $\Psi_{v'}(r)$ and lower $\Psi_v(r)$ vibrational eigenfunctions. With electronic transition moments $\mathcal{R}_{n'n}(r)$ from the literature, the electronic-vibrational strength $S_{ev}(n'v', nv)$ is computed using Equation 5.12 and the Hönl-London factor $S(J', J)$ is found from Eq. 5.2.1. Finally, the diatomic line strength is calculated as the product $S_{ev}(n'v', nv)\, S(J, J')$, see Eq. 5.6.

5.2.2 Computation of TiO γ Bands

An overview spectrum is generated with our current line strength file for TiO γ system. Figure 5.2 shows the normalized intensity versus wavelength for 5 bands,

namely for $\Delta v = +2, +1, 0, -1, -2$. The $\Delta v = \pm 3$ bands (not shown) are about a factor of 200 weaker than the 0-0 band. Here, we use a full-width at half maximum (FWHM) spectral resolution of FWHM = 0.15 nm, and a temperature of T = 2,500 K.

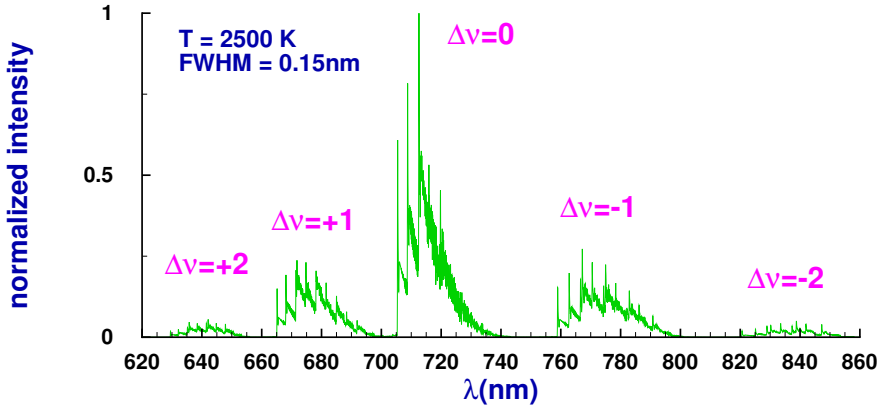

Figure 5.2: Overview of computed spectrum of TiO γ bands.

Electronically excited TiO molecules were observed following LIB (28) for delay times in excess of 30 μs. These observations occurred in the expanding plume, 13 mm from the laser-ablation spot generated with focused, 7 nanosecond, 90 mJ pulses, 532-nm radiation with irradiance of typically 3 TW/cm^2. A gate-width of 2μs at a delay time of 32 μs was employed to record TiO γ system band heads in the spectral range 750 - 780 nm. This particular experimental result, see Figure 6 in De Giacomo et al. (28), is further analyzed with our TiO A-X line strength file.

Early in the plasma decay for delay times on the order of 1 to 2 μs, molecular temperature on the order of 5,000 K is quite typical in LIBS experiments (e.g., see Parigger et al. (107)), yet for delay times of some 50 μs molecular temperature on the order of 2,500 K may be expected in expanding plumes. For that reason, and in view of the comparison displayed in Fig. 1.16, we elected to use T = 2,500 K in the TiO γ band overview. Application of our Nelder-Mead fitting routine to the TiO spectrum reported by De Giacomo et al. (28) allows us to infer temperature in the expanding plume following laser ablation (112). For the computed spectrum,

we utilized a spectral resolution of 0.5 nm, and find a temperature of 2,170 K. The error in temperature is estimated by use of Monte-Carlo simulations. Here, we vary the measured amplitudes by a factor of ± 25 % using a uniform random number generator. We find for the temperature 2,180 ± 55 Kelvin, where the 55 K error corresponds to the 1-σ error in the simulations.

5.2.3 Computation of TiO γ' and E-X systems

Just as for the TiO γ band, computational procedures were applied to find the Hönl-London factors (Eq. 5.2.1) as discussed in Hornkohl et al. (56) for the TiO γ' and E-X systems. Subsequently, the Frank-Condon factors (Eq. 5.2.1) and r-centroids (Eq. 5.2.1) were determined. Even though our experiments were not designed to measure the TiO $E - X$ system, for completeness the $E - X$, $\Delta v = 0$ spectrum is included. This band appears important for Astrophysics applications an has been studied in flame spectroscopy of TiO (77). Figure 1.15, shows an overview spectrum of the TiO $\gamma\,'$ sequences and progressions, and it also shows the TiO $E - X$ 0-0 spectrum.

5.3 Fitting Diatomic Transitions in the Presence of Atomic Lines

When gathering experimental spectra, it is not uncommon for additional line shapes to be present in the observed spectra resulting from a laser-induced plasma. Typically, these additional lines can be attributed to atomic transitions occurring in the plasma. This is especially common when experiments are conducted outside of a vacuum chamber containing carefully selected buffer gases. When one is performing laser ablation of a metal in laboratory air, a plethora of atomic lines are likely to be observed.

Fortunately, the evolution of laser-induced plasma often provides emissions from various species separated temporally. In the first few nanoseconds, the emissions

of a laser-induced plasma are dominated by a continuous emission spectrum of excited free electrons. Over the subsequent hundreds of nanoseconds, atomic emission lines characterize an observed spectrum. Beginning with higher ionized species and concluding with neutral atomic lines, different atomic line shapes will evolve in and out of observed spectra as delay time increases. Diatomic molecular transitions typically become discernible on the order of microseconds after plasma formation.

Concerning laser ablation of titanium in laboratory air, there are an abundance of titanium atomic lines detectable throughout a given spectral region. In some regions, these atomic transition lines are present at delay times on the order of tens of microseconds after laser ablation. At such delay times, it is expected that TiO diatomic molecular transitions will also be observable.

If one is only interested in the diatomic transitions, the use of a well chosen low-pass filter positioned along the observable path between the plasma and the spectrometer slit will serve to remove second order spectral emissions present in an observed spectrum. However, sometimes this will not remove all of the atomic spectral lines observed in a given region. Thus despite one's best efforts, diatomic transitions can be difficult to discern even if such transitions are present in a collected spectrum.

Figure 4.6 illustrates the results of fitting computed spectra to a measured spectrum for the measurements at the earlier time delays. In the experiment, it is observed that diatomic spectral transitions become noticeable at later delay times, as atomic transitions become less prominent. As demonstrated in Fig. 4.6, the Nelder-Mead fitting routine used is capable of providing a reasonable temperature inference for diatomic transitions despite the presence of multiple atomic transitions, even if the presence of the molecular transition is not obvious.

Table 4.1 provides temperature inferences obtained by fitting the TiO $A^3\Phi \rightarrow X^3\Delta$, $\Delta v = 0$ transitions in the spectral region of 705-715 nm. Measurements of the γ band were gathered at delay times ranging from 26-86 μs with a 4 μs gate width at intervals of 4 μs. As indicated in Table 4.1, the error associated with inferences

made from just visible diatomic transitions can be much larger than inferences with clearly defined transitions.

5.4 Indication of Combustion

Measurements observing the TiO γ, $\Delta v = 0$ transition band were collected at delay times ranging from 20 to 60 μs with a gate width of 5 μs. These measurements were gathered by incrementally increasing the delay time with 5 μs intervals. Then, another set of measurements were collected at time delays ranging from 26 to 60 μs with a 2 μs gate width measured at 2 μs intervals.

Tables 4.2 and 4.3 present the inferred temperatures of the TiO $A^3\Phi - X^3\Delta$, $\Delta v = 0$ system resulting from the Nelder-Mead fitting routine at various delay times following laser-induced breakdown. The first column of temperature values, labeled *T(K)*, represents the temperature inferred by fitting the entire range of the measured spectrum with our computed spectra. The temperature values falling under columns labeled *Rotational T(K)* and *Vibrational T(K)* represent the inferred temperatures by analyzing only the region containing predominantly rotational and vibrational structure, respectively.

Typically, the temperature is found as a result from the fitting of computed spectra to a measured spectrum over the full wavelength range of the measurement. For this investigation, spectral regions consisting of predominantly rotational or vibrational structure are fit individually, as well. Figure 4.8 presents a measured spectrum along with the synthetic spectra used to infer temperature. Figure 4.9 illustrates the results of fitting the same measurement with only the predominantly vibrational (left) and rotational (right) regions of the computed synthetic spectra. The synthetic spectra used to infer temperature represents the TiO $A^3\Phi - X^3\Delta$, $\Delta v = 0$ band. The measured data shown in Fig. 4.8 and Fig. 4.9 correspond to a delay time of 45 μs collected using an 4 μs window.

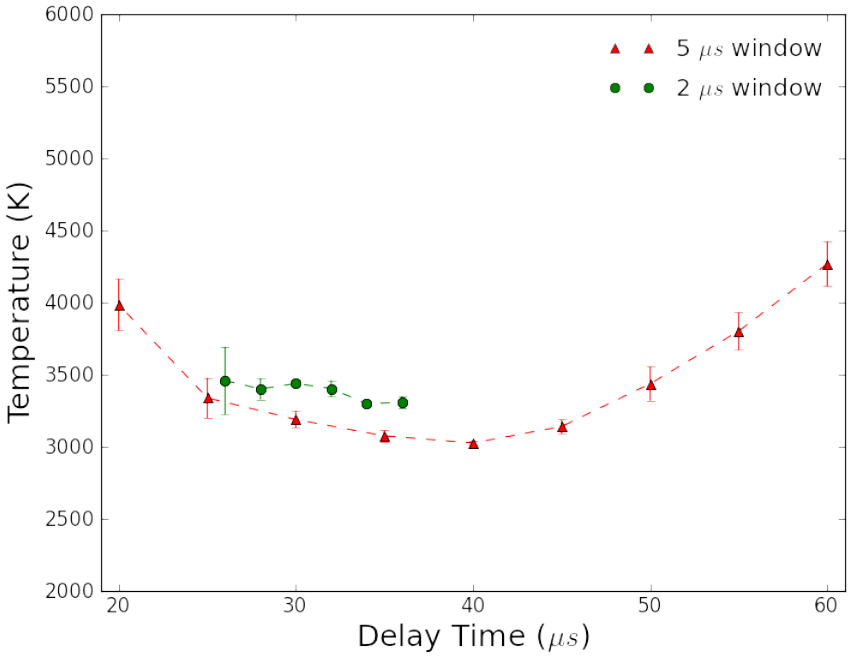

Figure 5.3: Temperature inferences as a function of time from laser ablation for 5 μs (Table 4.2) and 2 μs (Table 4.3) gate widths.

Figure 5.3 shows a visual representation of Tables 4.2 and 4.3. The plot illustrates that the inferred temperatures listed in 4.2 contain a local minimum between 20 and 60 μs subsequent to the generation of laser-induced plasma. The second experimental run provides a more temporally resolved representation for a spectral region where the first experimental run implies temperature decreasing to a local minimum.

The local minimum, as seen in the first set of experimental runs, is unexpected. Temperature is predicted to decrease with increasing delay time, as the laser-induced plasma equilibrates with the surrounding environment and cools. The presence of a local minimum with respect to temperature in regards to laser-induced plasma is sometimes indicative of combustion. In laser-induced plasma, combustion interrupts the overall cooling of the plasma and results in an increasing temperature for a brief time interval before the plasma ultimately resumes cooling. This process would thus result in a local minimum temperature followed by a local maximum with increasing

delay time. Here, it is important to note that following certain laser pulses the induced plasma was observed to eject luminescent material slightly displaced from the usual optical breakdown spark.

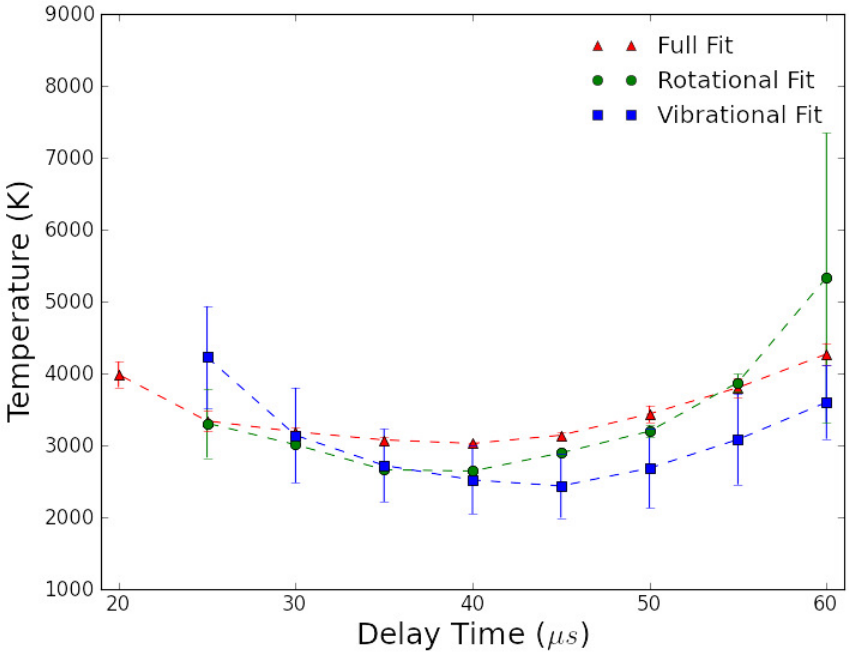

Figure 5.4: Temperature as a function of time after laser ablation as inferred by fitting the full experimental spectrum, as well as only select regions dominated by either rotational or vibrational molecular structure.

Figures 5.4-5.7 compare the full, rotational, and vibrational temperature inferences from Tables 4.2 and 4.3, respectively. Figure 5.4 reveals a local minimum for each type of fit, with the minima for the full fit and rotational fit occurring prior with respect to delay time than the minimum of the vibrational fit. However, it is clear from the error bars associated with each measurement that the rotational, vibrational, and full fits each return essentially the same temperature values. For Figures 5.4-5.7, the rotational and full fit inferences even more nicely with each other when compared to the inferences of a purely vibrational fit.

The errors associated with temperature inferences, while fitting only vibrational structure, are seen to be larger than the error associated with fitting purely rotational

structure or the full spectrum. This is largely due to the decreased number of spectral points included in fitting vibrational structure. As illustrated in Figure 4.9, the majority of the measured spectra can be considered rotational structure, while the vibrational structure typically consists of several intense peaks. This variability between spectra impacts temperature inferences. This reasoning also accounts for the agreement between a rotationally fit temperature inference and the full fit temperature inference.

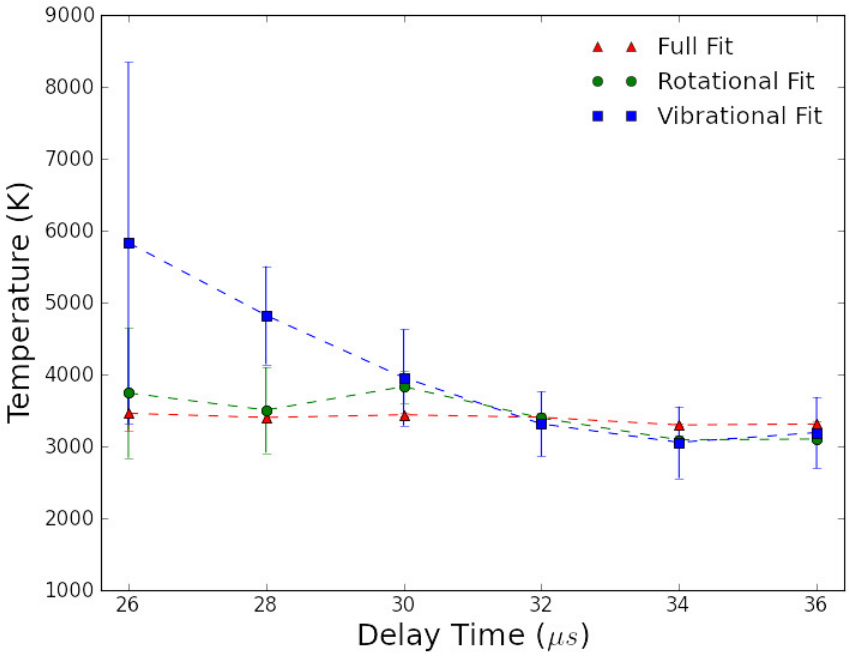

Figure 5.5: Temperature as a function of time after laser ablation as inferred by fitting the full experimental spectrum, as well as only select regions dominated by either rotational or vibrational molecular structure.

While the results of the first experimental run seem to suggest chemical reactions in the ablation plume at the later delay times, such an explanation is not entirely convincing. For the later delay times of the second series of measurements, the TiO transitions became increasingly less prominent in the measured spectra. A low signal to noise ratio of the diatomic spectrum, when compared to other spectral contributions, will often contribute to inferred temperatures which are believed to

be hotter than the actual temperature of the observed molecular transitions. This error is a consequence of poor signal to noise when using this particular method of inferring temperature, as the ratios of peak intensities of various transition lines are a key factor.

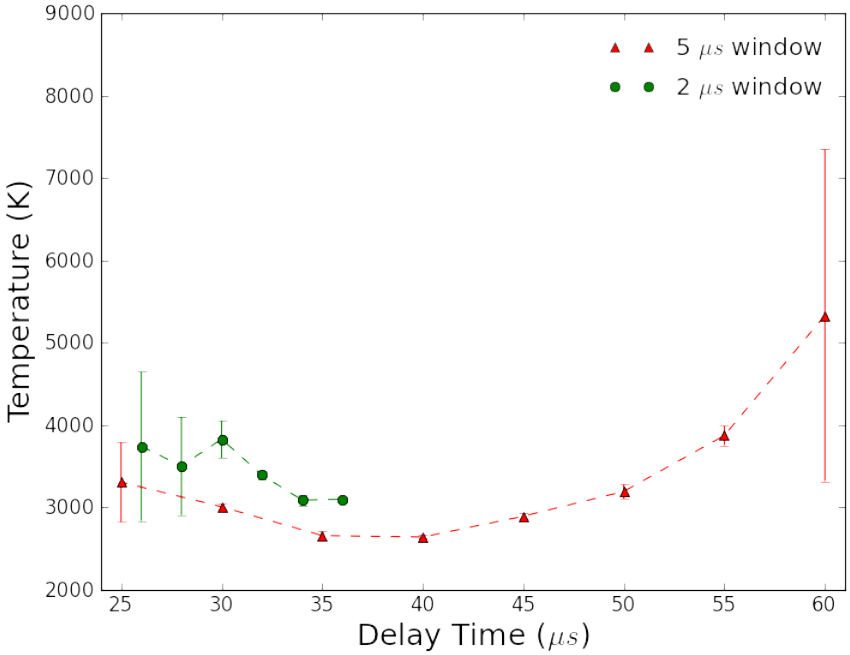

Figure 5.6: Temperature as a function of time after laser ablation as inferred by fitting only regions dominated by rotational molecular structure from the TiO $A^3\Phi - X^3\Delta$ transition.

The second set of measurements is meant to gain a clearer understanding of the expected transition temperatures for a given temporal region. The region of t_{delay} = 26-36 μs was chosen on account of the local minimum observed in the first series of measurements. Provided that the observed increase in inferred temperature from the first measurements might be due to low signal to noise, this temporal region is expected to be especially bright without over powering the diatomic transitions of interest. The decrease in observation window of the 5 μs used for the first series of measurements to 2 μs is meant to temporally localize an inferred temperature. It was expected that each measurement would result in an inferred

temperature slightly lower than the previous. The temperatures inferred by fitting each entire measured spectrum are consistent with each other and represent an overall decreasing temperature, see Figure 5.5. However, the temperatures do fluctuate. These fluctuations are relatively small and are within the error associated with the temperature inferences.

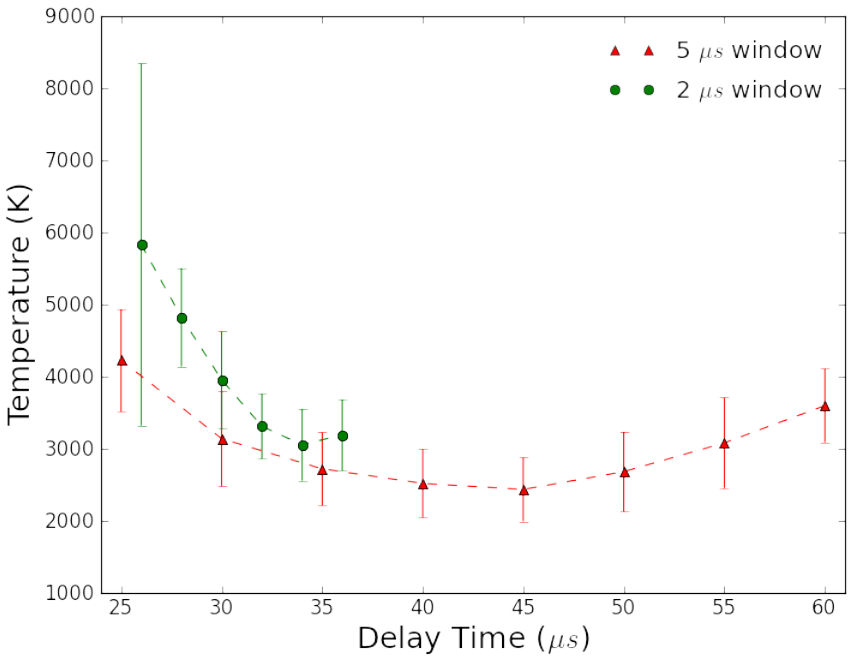

Figure 5.7: Temperature as a function of time after laser ablation as inferred by fitting only regions dominated by vibrational molecular structure from the TiO $A^3\Phi - X^3\Delta$ transition.

The results obtained by fitting only portions of the observed spectra believed to be dominated by rotational or vibrational transitions provide an intriguing element of analysis. It is predicted that the rotational transitions reach thermal equilibrium more readily than the vibrational transitions. Thus, distinguishing between a rotational and vibrational temperature could allow for a single spectrum collected at a given delay time to provide insight into which direction the temperature is trending. By inspecting Figure 5.4, the inferred vibrational temperatures provide a parabolic shape similar to that of the inferred rotational temperatures only delayed. Figure 5.5

provides an image of the inferred vibrational temperature possibly decreasing to that of the rotational temperature. Recall, the second experimental run gathered measurements near the local minimum provided by the inferred temperatures of the first series of measurements. While it is possible to see this predictive behavior by inferring temperatures only from the rotational structure in the plots, the error bars associated with each measurement indicate that the temperatures inferred from just rotational structure, vibrational structure, and both are all essentially equivalent. So, while this analysis did not provide us with any insight into temperature predictions, it does confirm that there is LTE.

5.4.1 Two-dimensional Analysis of TiO γ Band

By studying Figures 4.15-4.24, some very interesting phenomena becomes apparent. As seen in Section 5.1.3 regarding temperature inferences using the Boltzmann plot method, the temperature inferred from the TiO molecular transitions increases with height along the ablation plume. This phenomena is consistent throughout t_{delay} =20-200 μs. More interestingly, it is clear that between t_{delay} = 20-80 μs there are two distinct regions of the plasma. One region rests several millimeters above the sample surface, while the other appears to rise from the surface before the two ultimately combine. After the two regions combine ($\sim$100μs), there is a noticeable bulge in uppermost part of the intensity profile.

When the temperature inferences made from emissions of the two regions are compared, it is apparent that the inferred temperature of the TiO emissions from the region closer to the sample surface is distinctly lower than that of the region further above the surface. This is most clearly evident in Fig. 4.16 and 4.17. Particularly when examining the inferred temperatures of Fig. 4.16, it is important to keep in mind that we are struggling to make temperature inferences resulting from fitting computed TiO spectra to the collected spectra on account of signal to noise issues. When inspecting the inferred temperature more trust should be given to those values

inferred from the brighter regions of the plume. This conveniently allows for succinct comparison between the two regions of Fig. 4.16, as essentially all temperatures above 5,000 K are deemed less trust worthy.

By comparing the inferred temperature from the upper region of Fig. 4.16, we find remarkable agreement with the results obtained previously at this same time delay ($t_{delay} = 40\ \mu s$) using this same window (2 μs), see Fig. 5.3. If we make the same comparison with the upper region of Fig. 4.17 and Fig. 5.3 at $t_{delay} = 60\ \mu s$, there is some agreement for the inferred temperatures here as well. Now, recall that in Section 5.1.3 it was determined that our temperature inferences made by applying the Boltzmann plot method to the data provided in a linear diode like fashion represented the temperature at of the hottest emitting portion of the plume. It appears that we have once again encountered this feature attributed to integrating over the detector. With regards to the higher temperatures (>5000 K) inferred from the images such as in Fig. 4.16, these temperatures can effectively be considered erroneous and victims of poor signal to noise. We can assume that signal to noise is the culprit because our linear diode array measurement (see Fig. 4.8 and Tables 4.2 and 4.3), which contains minimal signal to noise issues, excellently agrees with our inferences from the region of our image least susceptible to signal to noise problems.

The local minimum encountered concerning inferred temperatures from TiO as a function of delay time discussed in the the previous section can now be further addressed. By examining the relevant temperature inferences of Fig. 4.16 and Fig. 4.17, we can again see the temperature of certain regions of the plume increase with delay time. Specifically, the regions affected tend to be the hotter regions of the plume. We can also determine that the mechanism for this increase in temperature is the interaction of emitting particles in the lower region of the plume rising from the surface to the upper region of the plume.

While more investigations are required to fully characterize this bright region rising from the surface, some simple hypotheses can be formed. By our ability to fit computed TiO spectra to this emitting region, we have determined that the TiO

molecule is the dominant emitter. Furthermore, because the temperatures inferred from the TiO transitions in this region are starkly less than those of the upper region and gradually increase as the regions interact, it is fair to assume that the mechanism causing the radiative transitions of the diatomic molecule is different between the two regions. In the upper region, the TiO transitions are the result of recombination. This is consistent with the delay time in which the transitions become discernible given the excitation source and the evolution of the temperature and electron density, as determined by the measurements made within the first hundreds of nanoseconds. However, since the lower region is much cooler and appears to heat as it leaves the surface, it leads one to believe that the TiO emissions in this region are emanating from bulk titanium being ejected from the sample surface.

5.5 Summary of Conclusions

In this work, ultra-violet Ti II and Ti III atomic transition lines were used to infer temperature of a laser ablation plasma above a pure titanium sample at time delays ranging from 20-500 ns. This was accomplished by use of the Saha-Boltzmann plot technique. The N II line at 399.5 nm was used to infer electron density in the plasma at each measured time interval, by measuring the observed Stark widths and comparing to previous calculations (66). The electron densities of the N II line measured in laser ablation plasma above the Ti surface and laser-induced plasma in laboratory air were also compared.

Two-dimensional imaging of the laser ablation plasma at a delay time of 200 ns was then used to observe five Ti III lines. This allowed for more reliable temperature inferences via the Boltzmann plot method, by providing more data points and a wider range of emitting energy level values than the previous measurements. The resulting temperatures were significantly cooler than the previously inferred temperature at $t_{delay} = 200$ ns. Further analysis of the inferred temperatures along the vertical height of the ablation plume above the sample surface indicate that the electron

temperature increases as a function of height along the plume. When the two-dimensional image is binned such that it behaves as an intensified linear diode array, the inferred temperature by means of the Boltzmann plot method corresponds to the inferred temperature from the hottest region along the height of the plume.

For the purposes of analyzing the laser ablation plasma above the Ti surface at time delays on the order of tens to hundreds of microseconds, TiO spectral transitions were utilized to infer temperature. This required the computation of new, accurate line-strength tables. The line-strengths were then used to generate computed spectra for various transitions of the molecule. Specifically, the TiO $B^3\Pi \rightarrow X^3\Delta$ and $A^3\Phi \rightarrow X^3\Delta$ $\Delta v = 0$ transition bands were observed in the ablation plasma. The collected spectra were then fit with computed spectra in order to infer temperature as a function of delay time.

Temperature inferences resulting from the use of an intensified linear diode array arrangement to gather spectra typically contained a local minimum occurring between a 40 μs and 60 μs delay time. Further investigation into this phenomena led to temperature inferences for vibrational and rotational temperature independently. The results confirmed that vibrational and rotational temperatures are equivalent for TiO in the observed plasma and also contained this local minimum.

Analysis of the TiO molecular transitions in two-dimensional spectra along the height of the plume for t_{delay} = 20 - 200 μs aided in explaining the unexpected temperature increase at such late delay times as 50 μs. The two-dimensional images contained two luminescent regions along the height of the plume at t_{delay} = 20 - 80 μs. Furthermore, the two regions provided two distinct temperatures. At a time delay of 40 μs, the temperature of the upper region is nearly 1000 K hotter than that of the lower region. As time passes, the lower region approaches the upper region, and the two regions combine in between 80 μs and 100 μs after laser plasma formation. As the lower region combines with the upper region, the temperature at the upper region temporarily increases before eventually decaying with the TiO spectral signal. The temperature inferred from the hotter, upper region is consistent with temperature

inferences from both the TiO $B^3\Pi \rightarrow X^3\Delta$ and $A^3\Phi \rightarrow X^3\Delta$ $\Delta v = 0$ transition bands at the same delay times, utilizing an intensified linear diode array arrangement.

The two-dimensional imaging of the TiO molecular transitions reveals a phenomenon that is rarely studied in laser-induced plasma. The spectral emissions of the observed plasma in this temporal range are no longer dominated by electron impacts, but are dominated by recombination. This recombination is likely responsible for the increase in temperature at the 60 μs to 80 μs delay time.

However, the drastic temperature difference at $t_{delay} = 40$ μs between the upper and lower luminescent regions remains largely unexplained. As the cooler plasma temperatures are found to be in the lower regions, it is possible that a sudden flurry of recombination occurs near the sample surface and the trend rises until it reaches the upper region. However, it is perhaps more likely that the bright lower region consists of bulk material that is being ejected from the sample in the form of TiO molecules or contain luminescent TiO molecules on their surface.

Chapter 6

Future Work

6.1 Two-dimensional Analysis

The additional data provided by the use of the two-dimensional ICCD camera greatly enhanced the research contained in this dissertation. A clear example is the insight into the increase in temperature of inferences from the TiO molecule at later delay times. Such a temperature increase is completely unexpected and is simply unacceptable for the LIP community without thorough investigation and repeatability. The additional dimension provided by the ICCD not only allowed for reproducibility, but also provided insight into the mechanisms responsible. Furthermore, these results were presented as part of a poster and oral presentation at the 22^{nd} International Conference of Spectral Line Shapes and were so well received that a collaboration on a future paper has been requested.

In addition to this future collaboration, additional investigations utilizing the two-dimensional ICCD are anticipated. Future investigations should include spatial analysis of laser ablation plasma with the intent on analyzing other transition bands of the TiO molecule. Future investigations should also include spatial analysis of laser ablation with the intent on analyzing other diatomic molecules such as C_2, CN, and AlO. Such investigations into TiO and other diatomic molecules should be performed

in laboratory air as well as in vacuum cell, where the buffer gas and pressure can be controlled. While this dissertation focused on laser ablation, spatial analysis of LIP of gasses is also of interest. To this extent the use of a vacuum cell is also greatly desired. The spectral signatures of diatomic molecules such as C_2, CN, NO, and N_2 produced by LIP of laboratory air can overlap in spectral regions of interest. By controlling the elements present in the cell, certain transitions which are typically overpowered by others may become observable.

Additional analysis of spectra resulting from two-dimensional images of LIP should include the use of a Radon transform in order to infer a three-dimensional perspective of the plasma. The use of the Radon transform is preferred to that of the more common Abel inversion. This is because the Abel inversion would assume a certain amount of symmetry about the LIP. From our investigations, we know this is not always the case.

The research reported here utilized the ICCD in only one manner, namely attached to the exit aperture of a spectrograph. The ICCD may additionally be used to capture images of the plasma expansion and evolution without the use of a spectrograph. Such images would be useful for investigating plasma dynamics. The ICCD may also be used in conjunction with a streak camera to study phenomena on a smaller time scale.

6.2 Error Analysis for Temperature Inferences

Additional research should also be focused on the error associated with making temperature inferences by means of Nelder-Mead fitting computed spectra to an experimentally obtained spectrum. The current research investigated and utilized a Monte-Carlo-like technique for error analysis of the temperatures inferred from diatomic transitions. However, similar techniques can be used to analyze the susceptibility of the Nelder-Mead algorithm to falling into local minimums. Such analysis will provide valuable insight into the true usefulness of the Nelder-Mead method in this research. For example, Figure C.2 presents the results of randomly

assuming a spectral baseline within a specified percentage of the actual baseline intensity refitting over 1000 iterations. The y-axis in the histogram represents the percentage of each temperature being returned as the best fit. The red dashed line would represent the standard distribution of the temperatures returned, but it is apparent that the best fitting temperatures as determined by the Nelder-Mead routine do not agree with this distribution. Rather, it appears the routine falls into several local minima around the temperature inference being investigated. The Nelder-Mead method is used out of convenience and its ability to provide a nonlinear multiparameter fit.

6.3 Self-absorption Studies

Additional studies involving self-absorption are also desired. Self-absorption is an issue that must constantly be addressed in LIP optical emission experiments. If self-absorption is occurring during the observation time of the experiment the results cannot be salvaged. Investigations into self-absorption have begun at UTSI by use of a mirror to reflect the image of the LIP back through itself (90). This method is perhaps the quickest and simplest to test for self-absorption to perform for LIBS experiments. This method was used with regards to self-absorption of the hydrogen Balmer series. The method therefore requires further investigations to first test its limitations and then its applications to various systems.

6.4 Isotopomers

In addition to experimental investigations, theoretical endeavors must also be undertaken. Namely, line-strength tables for the various isotopomers of TiO are desired. The current TiO line-strength table represents only the predominant isotopomer, $^{48}Ti^{16}O$. Adjustments in the calculation of the line strength files to account for the various isotopes is expected to permit further investigations for laser

ablation molecular isotopic spectrometry (LAMIS) (133), as the estimated magnitude of the vibrational isotope shifts are on the order of 0.6 nm. Similar investigations into TiO spectral signatures in stellar emissions are also of interest. Such analysis would provide insight in determining isotope abundances of titanium in stellar atmospheres. This research will require future collaborations with astrophysicists and possible grants through the NASA ROSES project.

Bibliography

[1] Allard, F., Hauschildt, P. H., and Schwenke, D. (2000). TiO and H_2O absorption lines in cool stellar atmospheres. *The Astrophysical Journal*, 540(2):1005–1015. 26

[2] Amiot, C., Azaroual, E. M., Luc, P., and Vetter, R. (1995). High resolution rotational analysis of the $B^3\Pi$-$X^3\Delta$ (1,0) band of titanium monoxide. *The Journal of Chemical Physics*, 102(11):4375–4381. 26

[3] Amoruso, S., Armenante, M., Berardi, V., Bruzzese, R., and Spinelli, N. (1997). Absorption and saturation mechanisms in aluminium laser ablated plasmas. *Applied Physics A*, 65(3):265–271. 24

[4] Ashkenazy, J., Kipper, R., and Caner, M. (1991). Spectroscopic measurements of electron density of capillary plasma based on Stark broadening of hydrogen lines. *Phys. Rev. A*, 43:5568–5574. 1

[5] Assim, E. M. (2008). Optical constants of titanium monoxide TiO thin films. *Journal of Alloys and Compounds*, 465(1–2):1–7. 82

[6] Baranger, M. (1958a). General impact theory of pressure broadening. *Phys. Rev.*, 112:855–865. 1, 85, 133

[7] Baranger, M. (1958b). Simplified quantum-mechanical theory of pressure broadening. *Phys. Rev.*, 111:481–493. 1, 85, 133

[8] Bartkowski, S., Neumann, M., Kurmaev, E. Z., Fedorenko, V. V., Shamin, S. N., Cherkashenko, V. M., Nemnonov, S. N., Winiarski, A., and Rubie, D. C. (1997). Electronic structure of titanium monoxide. *Phys. Rev. B*, 56:10656–10667. 26

[9] Blau, P., Smilanski, I., and Rosenwaks, S. (1992). Simultaneous time averaged measurements of gas temperature and electron density in a copper vapor laser using hydrogen emission spectroscopy. *Journal of Applied Physics*, 72(3):849–854. 1

[10] Born, M. and Oppenheimer, R. (1927). On the quantum theory of molecules. *Ann. Phys.*, 84:457. 49, 53

[11] Breech, F. and Cross, L. (1962). Optical microemission stimulated by a ruby maser. *Appl. Spectrosc.*, 16:59. 1

[12] Capitelli, F., Colao, F., Provenzano, M. R., Fantoni, R., Brunetti, G., and Senesi, N. (2002). Determination of heavy metals in soils by laser induced breakdown spectroscopy. *Geoderma*, 106(1–2):45–62. 82

[13] Capitelli, M. (2004). Laser-induced plasma expansion: Theoretical and experimental aspects. *Spectrochim. Acta Part B*, 59:271–289. 42, 45

[14] Cashion, J. K. (1963). Testing of diatomic potentialenergy functions by numerical methods. *The Journal of Chemical Physics*, 39(7):1872–1877. 55

[15] Chen, C. S., Man, B. Y., Liu, D., Song, X., and Chen, X. J. (2013). Investigation of Ti III line broadening in a laser-induced plasma. *Journal of Physics B: Atomic, Molecular and Optical Physics*, 46(1):015701. 86, 87, 88

[16] Christy, A. (1929). Quantum analysis of the blue-green bands of titanium oxide. *Phys. Rev.*, 33:701–729. 26, 62

[17] Churchwell, E., Hocking, W., Merer, A., and Gerry, M. (1980). Interstellar titanium monoxide: Limits and implications. *The Astronomical Journal*, 85:1382–1385. 26

[18] Ciucci, A., Corsi, M., Palleschi, V., Rastelli, S., Salvetti, A., and Tognoni, E. (1999). New procedure for quantitative elemental analysis by laser-induced plasma spectroscopy. *Appl. Spectrosc.*, 53(8):960–964. 82

[19] Collins, J. G. and Jr., T. D. F. (1974). Radiative opacities for the α, γ, and ϕ systems of titanium monoxide. *Journal of Quantitative Spectroscopy and Radiative Transfer*, 14(12):1259–1272. 26

[20] Cooley, J. W. (1961). An improved eigenvalue corrector formula for solving the schrodinger equation for central fields. *Mathematics of Computation*, 15(76):pp. 363–374. 55

[21] Coons, R. W., Harilal, S. M., Hassan, S. M., and Hassanein, A. (2011). The importance of loner wavelength reheating in dual-pulse laser-induced breakdown spectroscopy. *Appl. Phys. B*, 107:873–880. 3

[22] Cremers, D. A. (1987). The analysis of metals at a distance using laser-induced breakdown spectroscopy. *Applied Spectroscopy*, 41(4):572–579. 3

[23] Cremers, D. E. and Radziemski, L. J. (2006). *Handbook of Laser-induced Breakdown Spectroscopy*. John Wiley, New York, USA. 3, 82

[24] Curtis, C., Hirschfelder, J., and Adler, F. (1950). The separation of the rotational coordinates from the n-particle schroedinger equation. *J. Chem. Phys.*, 18:1638–1642. 49

[25] Davies, R. H. and Vanderslice, J. T. (1966). Second-order WKB corrections to Rydberg-Klein-Rees potential curves. *J. Chem. Phys.*, 45:95. 143

[26] Davis, S. P., Phillips, J. G., and Littleton, J. (1986). Transition rates for the TiO β, δ, ϕ, γ', γ, and α systems. *The Astrophysical Journal*, 309:449–454. 26

[27] Davydov, A. (1965). *Quantum Mechanics*. Pergamon, Oxford, UK. 49

[28] De Giacomo, A., Dell'Aglio, M., Santagata, A., and Teghil, R. (2005). Early stage emission spectroscopy study of metallic titanium plasma induced in air by femtosecond- and nanosecond-laser pulses. *Spectrochim. Acta, Part B*, 60:935–947. xiii, 28, 31, 62, 94

[29] Dimitrijević, M. and Konjević, N. (1980). Stark widths of doubly- and triply-ionized atom lines. *Journal of Quantitative Spectroscopy and Radiative Transfer*, 24(6):451–459. 85, 86, 134

[30] Dobrodey, N. V. (2001). Radiative transitions in TiO: Ab initio oscillator strengths and lifetimes for low-lying electronic states. *Astronomy and Astrophysics*, 365(3):642–655. 26

[31] Dors, I., Parigger, C., and Lewis, J. (1998). Spectroscopic temperature determination of aluminum monoxide in laser ablation with 266-nm radiation. *Opt. Lett.*, 23:1778–1780. 2, 13, 26

[32] Eickmans, J. H., Hsieh, W.-F., and Chang, R. K. (1987). Plasma spectroscopy of H, Li, and Na in plumes resulting from laser-induced droplet explosion. *Appl. Opt.*, 26(17):3721–3725. 1

[33] Faris, G. W. and Bergström, H. (1991). Two-wavelength beam deflection technique for electron density measurements in laser-produced plasmas. *Appl. Opt.*, 30(16):2212–2218. 24

[34] Fleischmann, J. P., Swafford, L. D., Witte, M. J., Surmick, D. M., Woods, A. C., Behery, S. A., Parigger, C. G., and Hornkohl, J. O. (2014). Spectroscopic temperature and number density of nitric oxide in laser-induced plasma. *Bulletin of the American Physical Society*. 20

[35] Giacomo, A. D. (2003). Experimental characterization of metallic titanium-laser induced plasma by time and space resolved optical emission spectroscopy. *Spectrochimica Acta Part B: Atomic Spectroscopy*, 58(1):71–83. 82

[36] Giacomo, A. D., Shakhatov, V., Senesi, G., Pascale, O. D., and Prudenzano, F. (2002). Plasma-assisted pulsed laser deposition for the improvement of the film growth process. *Applied Surface Science*, 186(1–4):533–537. Proceedings of the European Materials Research Society 2001-Symposium L Photon-induced Sufrace Proceedings. 82

[37] Gigosos, M. A. and Cardeñoso, V. (1996). New plasma diagnosis tables of hydrogen Stark broadening including ion dynamics. *J. Phys. B: At. Mol. Opt. Phys.*, 29(20):4795–4838. 2

[38] Gigosos, M. A., González, M. A., and Cardeñoso, V. (2003). Computer simulated Balmer-alpha, -beta and -gamma Stark line profiles for non-equilibrium plasmas diagnostics. *Spectrochimica Acta Part B: Atomic Spectroscopy*, 58(8):1489–1504. 5th European Furnace Symposium and 10th International Solid Sampling Colloquium with Atomic Spectroscopy. 2

[39] Gornushkin, I., Shabanov, S., Merk, S., Tognoni, E., and Panne, U. (2010). Effects of non-uniformity of laser induced plasma on plasma temperature and concentrations determined by the boltzmann plot method: Implications from plasma modeling. *J. Anal. At. Spectrom.*, 25:1643–1653. 7, 46

[40] Goroshin, S., Mamen, J., Higgins, A., Bazyn, T., Glumac, N., and Krier, H. (2007). Emission spectroscopy of flame fronts in aluminum suspensions. *Proceedings of the Combustion Institute*, 31(2):2011–2019. 15, 16

[41] Grant, C. D., Schwartzberg, A. M., Smestad, G. P., Kowalik, J., Tolbert, L. M., and Zhang, J. Z. (2002). Characterization of nanocrystalline and thin film TiO_2 solar cells with poly (3-undecyl-2, 2-bithiophene) as a sensitizer and hole conductor. *Journal of electroanalytical Chemistry*, 522(1):40–48. 82

[42] Greiner, W., Neise, L., and Stöcker, H. (1997). *Thermodynamics and Statistical Mechanics*. Springer-Verlag, New York, USA. 46

[43] Griem, H. (1964). *Plasma Spectroscopy*. McGraw-Hill, New York, USA. 1, 58, 133

[44] Griem, H. (1974). *Spectral Line Broadening by Plasma*. Academic Press, New York, USA. 1

[45] Griem, H. (1997). *Principles of Plasma Spectroscopy*. Cambridge University Press, Cambridge, UK. 43, 47, 84

[46] Griem, H. R. (1968). Semiempirical formulas for the electron-impact widths and shifts of isolated ion lines in plasmas. *Phys. Rev.*, 165:258–266. 85, 86, 88, 133

[47] Griem, H. R., Baranger, M., Kolb, A. C., and Oertel, G. (1962). Stark broadening of neutral helium lines in a plasma. *Phys. Rev.*, 125:177–195. 133

[48] Hammack, S. D., Carter, C. D., Gord, J. R., and Lee, T. (2012). Nitric-oxide planar laser-induced fluorescence at 10 khz in a seeded flow, a plasma discharge, and a flame. *Appl. Opt.*, 51:8817–8824. 24

[49] Height, J., Donaldson, B., Gill, W., and Parigger, C. (2011). Measurements in solid propellant plumes at ambient conditions. *Proceedings of IMECE2011*, page 62726. 13

[50] Helbig, V. and Nick, K. P. (1981). Investigation of the Stark broadening of Balmer beta. *J. Phys. B: At. Mol. Phys.*, 14(19):3573–3583. 1

[51] Hermann, J., Boulmer-Leborgne, C., and Hong, D. (1998). Diagnostics of the early phase of an ultraviolet laser-induced plasma by spectral line analysis considering self-absorption. *J. Appl. Phys.*, 83(7):691–696. 44

[52] Hermann, J., Thomann, A., Boulmer-Leborgne, C., Dubreuil, B., De Giorgi, M. L., Perrone, A., Luches, A., and Mihailescu, I. N. (1995). Plasma diagnostics in pulsed laser TiN layer deposition. *J. Appl. Phys.*, 77(7):2928–2936. 24, 41

[53] Hilborn, R. (1981). Analysis of atomic and molecular superposition spectra following laser-induced optical breakdown. *Am. J. Phys.*, 50:982–986. 8

[54] Hirschfelder, J. and Wigner, E. (1935). *Proc. Nat. Acad. Sci.*, 21:113–119. 49

[55] Hornkohl, J., Nemes, L., and Parigger, C. (2011). Spectroscopy of carbon containing diatomic molecules. *Spectroscopy, Dynamics and Molecular Theory of*

Carbon Plasmas and Vapor, L. Nemes and S. Irle, eds.(World Scientific, 2011), pages 113–165. 2, 8

[56] Hornkohl, J. O., Parigger, C. G., and Nemes, L. (2005). Diatomic Hönl-London factor computer program. *Appl. Opt.*, 44(18):3686–3695. 91, 95

[57] Howe, J. (1963). Observations on the maser-induced graphite jet. *J. Chem. Phys.*, 39:1362. 1

[58] Jarmain, W. R. (1971). Realistic Franck-Condon factors and related integrals for diatomic molecules I. Method. *Journal of Quantitative Spectroscopy and Radiative Transfer*, 11(5):421–426. 57

[59] Jones, H. R. A. and Tsuji, T. (1997). Spectral evidence for dust in late-type M dwarfs. *The Astrophysical Journal Letters*, 480(1):L39–L41. 26

[60] Jorgensen, H. (1994). Effects of TiO in stellar atmospheres. *Astron. Astrophys.*, 284:179–186. 26

[61] Judd, B. (1975). *Angular Momentum Theory for Diatomic Molecules*. Academic, New York, USA. 49

[62] Killinger, D. K., Allen, S. D., Waterbury, R. D., Stefano, C., and Dottery, E. L. (2007). Enhancement of Nd:YAG LIBS emission of a remote target using a simultaneous CO_2 laser pulse. *Opt. Express*, 15(20):12905–12915. 3

[63] Kirkpatrick, J. D., Reid, I. N., Liebert, J., Cutri, R. M., Nelson, B., Beichman, C. A., Dahn, C. C., Monet, D. G., Gizis, J. E., and Skrutskie, M. F. (1999). Dwarfs cooler than "M": The definition of spectral type "L" using discoveries from the 2-micron all-sky survey (2mass). *The Astrophysical Journal*, 519(2):802–833. 26

[64] Klein, O. (1932). Zur berechnung von potentialkurven fr zweiatomige molekle mit hilfe von spektraltermen. *Z. Physik*, 76(3):226–235. 55, 90, 137, 139

[65] Knight, A. K., Scherbarth, N. L., Cremers, D. A., and Ferris, M. J. (2000). Characterization of laser-induced breakdown spectroscopy (LIBS) for application to space exploration. *Applied Spectroscopy*, 54(3):331–340. 3

[66] Konjevi, N., Lesage, A., Fuhr, J. R., and Wiese, W. L. (2002). Experimental Stark widths and shifts for spectral lines of neutral and ionized atoms (a critical review of selected data for the period 1989 through 2000). *Journal of Physical and Chemical Reference Data*, 31(3):819–927. 85, 86, 105

[67] Kools, J. C. S., Baller, T. S., De Zwart, S. T., and Dieleman, J. (1992). Gas flow dynamics in laser ablation deposition. *Journal of Applied Physics*, 71(9):4547–4556. 24

[68] Kotnik-Karuza, D. and Jurdana-Sepic, R. (2000). CH Cygni: TiO molecule as a probe of temperature variations in the atmosphere of the cool component. *Astron. Astrophys.*, 355:595–602. 26

[Kramida et al.] Kramida, A., Ralchenko, Y., and Reader, J. NIST atomic spectra database. http://www.nist.gov/pml/data/asd.cfm. Accessed: 2014-06-26. xi, 83, 84, 89

[70] Krupp, B., Collins, J., and Johnson, H. (1978). The effects of TiO opacity on the atmospheric structure of cool stars. *The Astrophysical Journal*, 219:963–969. 26

[71] Kushawaha, V. (1973). Potential energy curves and dissociation energy of titanium monoxide. *The Journal of Physical Chemistry*, 77(24):2885–2888. 26

[72] Laux, C. (2002). Radiation and nonequilibrium collisional-radiative models. *von Karman Institute Lecture Series*, 60:935–947. 12

[73] Lewis, J. W. L., Parigger, C. G., Hornkohl, J. O., and Guan, G. (1999). Laser induced optical breakdown plasma spectra and analyses with the program NEQAIR. *AIAA-99-0723*. 20

[74] Linlor, W. (1962). Plasma produced by laser bursts. *Bull. Am. Phys. Soc.*, 7:440. 1

[75] Linsebigler, A. L., Lu, G., and Yates, J. T. (1995). Photocatalysis on TiO_2 surfaces: Principles, mechanisms, and selected results. *Chemical Reviews*, 95(3):735–758. 82

[76] Linton, C. and Broida, H. (1977a). Flame spectroscopy of TiO: Chemiluminescence. *Journal of Molecular Spectroscopy*, 64(3):382–388. 26

[77] Linton, C. and Broida, H. (1977b). Flame spectroscopy of TiO: Chemiluminescence. *Journal of Molecular Spectroscopy*, 64(3):382–388. 95

[78] Linton, C. and Broida, H. (1977c). Flame spectroscopy of TiO: Photoluminescence of the α ($C^3\Delta$-$X^3\Delta$) system. *Journal of Molecular Spectroscopy*, 64(3):389–400. 26

[79] Litvak, M. M. and Edwards, D. (1966a). 7A8 - spectroscopic studies of laser-produced hydrogen plasma. *Quantum Electronics, IEEE Journal of*, 2(9):486–492. 1

[80] Litvak, M. M. and Edwards, D. F. (1966b). Electron recombination in laser produced hydrogen plasma. *Journal of Applied Physics*, 37(12):4462–4474. 1

[81] Lodders, K. (2002). Titanium and vanadium chemistry in low-mass dwarf stars. *The Astrophysical Journal*, 577(2):974–985. 26

[82] Lopez-Moreno, C., Palanco, S., Laserna, J. J., DeLucia Jr, F., Miziolek, A. W., Rose, J., Walters, R. A., and Whitehouse, A. I. (2006). Test of a stand-off laser-induced breakdown spectroscopy sensor for the detection of explosive residues on solid surfaces. *J. Anal. At. Spectrom.*, 21:55–60. 3

[83] Lowater, F. (1928). The band systems of titanium oxide. *Proceedings of the Physical Society*, 41(1):557–568. 26

[84] Maimon, T. (1960). Stimulated optical radiation in ruby. *Nature*, 187:493–494. 1

[85] Martín, E. L., Delfosse, X., Basri, G., Goldman, B., Forveille, T., and Osorio, M. R. Z. (1999). Spectroscopic classification of late-M and L field dwarfs. *The Astronomical Journal*, 118(5):2466–2482. 26

[86] Martin, M. Z., Cheng, M. D., and Martin, R. C. (1999). Aerosol measurement by laser-induced plasma technique: A review. *Aerosol Science and Technology*, 31(6):409–421. 3

[87] Milone, A. and Barbuy, B. (1994). TiO bands as a function of stellar parameters. *Astron. Astrophys. Suppl.*, 108:449–454. 26

[88] Miziolek, A., Palleschi, V., and Schechter, I. (2006). *Laser Induced Breakdown Spectroscopy*. Cambridge University Press, New York, USA. 2

[89] Mizushima, M. (1975). *The Theory of Radiating Diatomic Molecules*. Wiley, New York, USA. 49

[90] Moon, H.-Y., Herrera, K. K., Omenetto, N., Smith, B. W., and Winefordner, J. (2009). On the usefulness of a duplicating mirror to evaluate self-absorption effects in laser induced breakdown spectroscopy. *Spectrochimica Acta Part B: Atomic Spectroscopy*, 64(7):702–713. 110

[91] Muray, J. (1963). Photoelectric effect induced by high-intensity laser light beam form quartz and borosilicate glass. *Bull. Am. Phys. Soc.*, 8:77. 1

[92] Nelder, J. A. and Mead, R. (1965). A simplex method for function minimization. *The computer journal*, 7(4):308–313. 8, 15, 59

[93] Oks, E. (2006a). *Stark Broadening of Hydrogen and Hydrogen like Spectral Lines on Plasmas: The Physical Insight*. Alpha Science International, Oxford, UK. 2

[94] Oks, E. (2006b). *Stark Broadening of Hydrogen and Hydrogenlike Spectral Lines in Plasmas: The Physical Insight*. Alpha Science Int., Oxford, UK. 3

[95] Oks, E. (2006c). Stark widths of hydrogen spectral lines in plasmas: a highly-advanced non-simulative semiclassical theory and tables. In *Spectral Line Shapes: 18th International Conference on Spectral Line Shapes*, volume 874, pages 19–34. AIP Publishing. 2

[96] Ollis, D. F. (2000). Photocatalytic purification and remediation of contaminated air and water. *Comptes Rendus de l'Académie des Sciences-Series IIC-Chemistry*, 3(6):405–411. 82

[97] Oregan, B. and Grätzel, M. (1991). Low cost and highly efficient solar cells based on the sensitization of colloidal titanium dioxide. *Nature*, 335(24):737–740. 82

[98] Parigger, C.G. Woods, A., Oks, E., Hornkohl, J., Height, J., Donaldson, B., and Gill, W. (2011a). Atomic and molecular superposition spectra following laser-induced optical breakdown. In *Proceedings of 3rd North American Symposium on Laser Induced Optical Breakdown*, volume 1. xii, 3, 13, 15, 26

[99] Parigger, C. (2010). Diagnostic of a laser-induced optical breakdown based on half-width at half area of H_α, H_β, and H_γ lines. *Int. Rev. Atom. Mol. Phys.*, 1(2):129–136. 2, 3, 6, 7

[100] Parigger, C. (2013). Atomic and molecular emissions in laser-induced breakdown spectroscopy. *Spectrochim. Acta Part B*, 79–80:4–16. 42

[101] Parigger, C., Dackman, M., and Hornkohl, J. (2008). Time-resolved spectroscopy measurements of hydrogen-alpha, -beta, and -gamma emissions. *Appl. Opt.*, 47:G1–G6. 2, 3, 6, 7

[102] Parigger, C., Guan, G., and Hornkohl, J. (2003a). Measurement and analysis of OH emission spectra following laser-induced optical breakdown in air. *Appl. Opt.*, 42(30). 7, 29

[103] Parigger, C. and Hornkohl, J. (2010). Diatomic molecular spectroscopy with standard and anomalous commutators. *Int. Rev. Atom. Mol. Phys.*, 1:25–43. 27

[104] Parigger, C. and Hornkohl, J. (2011). Computation of AlO $B\,^2\Sigma^+ \rightarrow X\,^2\Sigma^+$ emission spectra. *Spectrochim. Acta, Part A*, 81(1):404–411. 9, 10, 13, 54

[105] Parigger, C. and Oks, E. (2010). Hydrogen Balmer series spectroscopy in laser-induced breakdown plasmas. *Int. Rev. Atom. Mol. Phys.*, 1(1):13–23. 2, 3, 6, 26

[106] Parigger, C., Plemmons, D., and Oks, E. (2003b). Balmer series H_β measurements in a laser induced hydrogen plasma. *Appl. Opt.*, 42:5992–6000. 3

[107] Parigger, C., Woods, A., and Hornkohl, J. (2011b). Analysis of atomic and molecular superposition spectra following laser-induced optical breakdown. *Int. Rev. Atom. Mol. Phys.*, 2:77–83. 3, 8, 13, 94

[108] Parigger, C. G., Lewis, J. W. L., Plemmons, D. H., and Hornkohl, J. O. (1996). Nitric oxide optical breakdown spectra and analysis by the use of the program NEQAIR. *Laser Appl. Chem. Bio. Env. Anal.*, 3:85–87. 20

[109] Parigger, C. G., Surmick, D. M., Woods, A. C., Donaldson, A. B., and Height, J. L. Measurement and analysis of aluminum monoxide flame emission spectra. In *U.S. National Comb. Meet. 2013. Park City, UT*. 13

[110] Parigger, C. G., Woods, A., and Hornkohl, J. O. (2012a). Analysis of time-resolved superposed atomic hydrogen Balmer lines and molecular diatomic carbon spectra. *Appl. Opt.*, 51(7):B1–B6. xii, 3, 6, 7, 8, 12, 26, 31

[111] Parigger, C. G., Woods, A. C., Height, J., Donaldson, A. B., and Gill, W. AlO flame emission spectroscopy. x, xii, xiii, 13, 14, 17, 18, 19, 26

[112] Parigger, C. G., Woods, A. C., Keszler, A., Nemes, L., and Hornkohl, J. O. (2012b). Titanium monoxide spectroscopy following laser-induced optical

breakdown. In *International Symposium On High Power Laser Ablation 2012*, volume 1464, pages 628–639. AIP Publishing. xiii, xiv, 27, 29, 30, 31, 33, 37, 38, 59, 60, 62, 65, 94

[113] Parigger, C. G., Woods, A. C., and Rezaee, M. R. (2012c). Atomic hydrogen and molecular carbon emissions in laser-induced breakdown spectroscopy. *Journal of Physics: Conference Series*, 397(1):012022. 3

[114] Parigger, C. G., Woods, A. C., Surmick, D. M., Donaldson, A., and Height, J. L. (2014a). Aluminum flame temperature measurements in solid propellant combustion. *Appl. Spectrosc.*, 68(3):362–366. 13

[115] Parigger, C. G., Woods, A. C., Surmick, D. M., Swafford, L. D., and Witte, M. J. (2014b). Measurements of ultra-violet titanium lines in laser-ablation plasma. *Spectrochimica Acta Part B: Atomic Spectroscopy*, 99(0):15–19. 30

[116] Parigger, C. G., Woods, A. C., Witte, M. J., Swafford, L. D., and Surmick, D. M. (2014c). Measurement and analysis of atomic hydrogen and diatomic molecular AlO, C_2, CN, and TiO spectra following laser-induced optical breakdown. *Journal of visualized experiments : JoVE*, (84):e51250. 3, 30, 31

[117] Park, C. (1985). Nonequilibrium air radiation (Neqair) program: User's manual. 20

[118] Park, R. T. and Hirschfelder, J. O. (1968). Separation of rotational coordinates from the N-electron diatomic Schrödinger equation. *J. Chem. Phys.*, 49:4009. 49

[119] Pathak, C. and Palmer, H. (1970). New electronic transitions in TiO. *Journal of Molecular Spectroscopy*, 33(1):137–146. 26

[120] Pender, J., Pearman, B., Scaffidi, J., Goode, S. R., and Angel, S. M. (2006). *Laser Induced Breakdown Spectroscopy*. Cambridge University Press, New York, USA. 3

[121] Phillips, J. (1954). The laboratory determination of relative transition probabilities of diatomic molecules I. the α-system of TiO. *ApJ*, 119:274–285. 26

[122] Phillips, J. G. (1950). Singlet electronic states of the TiO molecule. *The Astrophysical Journal*, 111:314–327. 28

[123] Phillips, J. G. (1951). A rotational analysis of the gamma-system of the TiO molecule. *The Astrophysical Journal*, 114:152–162. 28

[124] Phillips, J. G. (1969). The gamma'-system of the TiO molecule. *The Astrophysical Journal*, 157:449–458. 28

[125] Phillips, J. G. (1973). Molecular constants of the TiO molecule. *The Astrophysical Journal Supplement Series*, 26(232):313–331. 28

[126] Phillips, J. G. (1974). The fundamental rotation-vibration band of TiO. *The Astrophysical Journal Supplement Series*, 27:319–330. 28

[127] Plez, B. (1998). A new TiO line list. *Astronomy and Astrophysics*, 337:495–500. 26

[128] Press, W. H., Teukolsky, S. A., Vetterling, W. T., and Flannery, B. P. (2007). *Numerical Recipes in FORTRAN: the Art of Scientific Computing*. Cambridge University Press, New York, USA. 61, 62

[129] Ram, R. S., Bernath, P. F., Dulick, M., and Wallace, L. (1999). The $A^3\Phi - X^3\Delta$ system (γ bands) of TiO: Laboratory and sunspot measurements. *The Astrophysical Journal Supplement Series*, 122(1):331. 26, 93

[130] Rees, A. L. G. (1947). The calculation of potential-energy curves from band-spectroscopic data. *Proc. Phys. Soc.*, 59:998–1008. 55, 90, 139

[131] Rosenwasser, S., Asimellis, G., Bromley, B., Hazlett, R., Martin, J., Pearce, T., and Zigler, A. (2001). Development of a method for automated quantitative

analysis of ores using LIBS. *Spectrochimica Acta Part B: Atomic Spectroscopy*, 56(6):707–714. 3

[132] Rubin, P. (1966). Line intensity factors in electronic spectra of diatomic molecules. *Opt. Spectrosc.*, 20:325. 49

[133] Russo, R. E., Bol'shakov, A. A., Mao, X., McKay, C. P., Perry, D. L., and Sorkhabi, O. (2011). Laser ablation molecular isotopic spectrometry. *Spectrochimica Acta Part B: Atomic Spectroscopy*, 66(2):99–104. 111

[134] Rydberg, R. (1932). Graphische darstellung einiger bandenspektroskopischer ergebnisse. *Z. Physik*, 73(5-6):376–385. 55, 90, 137, 139

[135] Saha, M. (1920). Ionization in the solar chromosphere. *Philos. Mag.*, 40(6):472. 48

[136] Saha, M. (1921). On a physical theory of stellar spectra. *Proc. R. Soc. Lond.*, 99(A):135–152. 48

[137] Savitzky, A. and Golay, M. J. E. (1964). Smoothing and differentiation of data by simplified least squares procedures. *Analytical Chemistry*, 36(8):1627–1639. 61, 62

[138] Schamps, J., Sennesal, J., and Carette, P. (1992). Spontaneous radiative properties of the excited electronic states of TiO. *Journal of Quantitative Spectroscopy and Radiative Transfer*, 48(2):147–152. 26

[139] Schmidt, S., Wallerstein, G., Woolf, V., and Bean, J. (2009). Cool star oxygen abundances of from spectral synthesis of TiO bands. *American Institute of Physics*. 26

[140] Schulz, C., Sick, V., Heinze, J., and Stricker, W. (1997). Laser-induced-fluorescence detection of nitric oxide in high-pressure flames with A-X (0,2) excitation. *Appl. Opt.*, 36:3227–3232. 24

[141] Semaltianos, N. G., Logothetidis, S., Frangis, N., Tsiaoussis, I., Perrie, W., Dearden, G., and Watkins, K. G. (2010). Laser ablation in water: A route to synthesize nanoparticles of titanium monoxide. *Chemical Physics Letters*, 496(1):113–116. 82

[142] Settles, G. (2001). *Schlieren and Shadowgraph Techniques: Visualizing Phenomena in Transparent Media*. Springer Verlag, New York, USA. xii, 5

[143] Simeonsson, J. B. and Miziolek, A. W. (1993). Time-resolved emission studies of ArF-laser-produced microplasmas. *Appl. Opt.*, 32(6):939–947. 1

[144] Singh, J. P. and Thakur, S. N. (2007). *Laser Induced Breakdown Spectroscopy*. Elsevier Science, New York, USA. 3

[145] Spindler, R. J. (1965). Franck-condon factors based on RKR potentials with applications to radiative absorption coefficients. *Journal of Quantitative Spectroscopy and Radiative Transfer*, 5(1):165–204. 57

[146] Steele, R. and Linton, C. (1978). Flame spectroscopy of TiO: Radiative lifetimes and oscillator strengths of the α (c3δ-x3δ) system. *Journal of Molecular Spectroscopy*, 69(1):66–70. 26

[147] Steimle, T. C. and Virgo, W. (2003). The permanent electric dipole moments of the $X^3\Delta$, $E^3\Pi$, $A^3\Phi$ and $B^3\Pi$ states of titanium monoxide, TiO. *Chemical Physics Letters*, 381(1–2):30–36. 26

[148] Stewart, S. M. (2012). Blackbody radiation functions and polylogarithms. *Journal of Quantitative Spectroscopy and Radiative Transfer*, 113(3):232–238. 14

[149] Surmick, D. M., Woods, A. C., Parigger, C. G., Height, J., Donaldson, A. B., and Gill, W. (2012). Spectroscopy of aluminum monoxide in flames. *Bulletin of the American Physical Society*, 57. 13

[150] Tanguay, V., Goroshin, S., Higgins, A. J., and Zhang, F. (2009). Aluminum particle combustion in high-speed detonation products. *Combustion Science and Technology*, 181(4):670–693. 15, 16

[151] Tankcosić, D., Popović, L., and Dimitrijević, M. S. (2001). Electron-impact Stark broadening parameters for Ti II and Ti III spectral lines. *Atomic Data and Nuclear Data Tables*, 77(2):277–310. 85, 88

[152] Tellinghuisen, J. (1972). Fast, accurate RKR computations. *J. Mol. Spectosc.*, 44:194–196. 90, 141

[153] Tellinghuisen, J. (1974). A fast quadrature method for computing diatomic RKR potential curves. *Comp. Phys. Comm.*, 6:221–228. 55, 90, 141

[154] Tognoni, E., Christoforetti, G., Legnaioli, S., Palleschi, V., Salvetti, A., Mueller, M., Panne, U., and Gornushkin, I. (2007). A numerical study of expected accuracy and precision in calibration-free laser-induced breakdown spectroscopy in the assumption of ideal analytical plasma. *J. Anal. At. Spectrom.*, 62(12):1287–1302. 48

[155] Valenti, J. A., Piskunov, N., and Johns-Krull, C. M. (1998). Spectral synthesis of TiO lines. *The Astrophysical Journal*, 498(2):851–862. 26

[156] Wang, X. T., Man, B. Y., Wang, G. T., Zhao, Z., Liao, Y., Xu, B. Z., Xia, Y. Y., Mei, L. M., and Hu, X. Y. (1996). Optical spectroscopy of plasma produced by laser ablation of Ti alloy in air. *Journal of Applied Physics*, 80(3):1783–1786. 24

[157] Wiese, W. L. and Augis, J. A. (1977). Time- and space-resolved spectroscopic studies of electrical breakdowns in an argon-hydrogen mixture. *J. Phys. B: At. Mol. Phys.*, 48:4528–4535. 1

[158] Wigner, E. and Witmer, E. (1928). On the structure of the spectra of two-atomic molecules according to quantum mechanics. *Z. Phys.*, 51:859. 49, 53

[159] Willmott, P. R. and Huber, J. R. (2000). Pulsed laser vaporization and deposition. *Rev. Mod. Phys.*, 72:315–328. 82

[160] Wöhl, H. (1971). On molecules in sunspots. *Solar Physics*, 16(2):362–372. 26

[161] Woods, A. and Parigger, C. (2013). Micro-plasma parameter inferences utilizing titanium spectral transitions. *Bulletin of the American Physical Society*, 58. 30, 31

[162] Woods, A. C. and Parigger, C. G. (2011). Identification and analysis of atomic and molecular superposition spectra following laser-induced optical breakdown. In *APS Southeastern Section Meeting Abstracts*, volume 1. xii, 3, 13, 14, 26

[163] Woods, A. C. and Parigger, C. G. (2012). Acquisition and analysis of titanium monoxide spectra in plasma. *Bulletin of the American Physical Society*, 57. 25, 30, 31

[164] Woods, A. C. and Parigger, C. G. (2014). Molecular spectroscopy of TiO in laser-induced plasma. *Bulletin of the American Physical Society*. 30, 31

[165] Woods, A. C., Parigger, C. G., and Hornkohl, J. O. (2012a). LIBS: Measurement and analysis of TiO spectra. In *SCiX 2012 The Great Scientific Exchange Program Book of Abstracts*, page 136. 25, 30

[166] Woods, A. C., Parigger, C. G., and Hornkohl, J. O. (2012b). Measurement and analysis of titanium monoxide spectra in laser-induced plasma. *Opt. Lett.*, 37(24):5139–5141. xiv, 25, 29, 30, 31, 61, 62, 65

[167] Woods, A. C., Parigger, C. G., and Hornkohl, J. O. (2012c). Time-resolved temperature inferences utilizing the TiO $A^3\Phi \rightarrow X^3\Delta$ band in laser-induced plasma. *Int. Rev. Atom. Mol. Phys.*, 3(2):103–111. xiv, 25, 30, 63, 65

[168] Woods, A. C., Parigger, C. G., Keszler, A., Nemes, L., and Hornkohl, J. O. (2012d). Analysis of TiO spectral transitions in laser-induced and radio-frequency thermal plasmas. *Int. Rev. Atom. Mol. Phys.*, 3(1):51–59. 30

[169] Woods, A. C., Parigger, C. G., Oks, E., and Hornkohl, J. O. (2011). Analysis of combined atomic and molecular spectra. In *FACSS 2011 Analytical Science and Innovation Program Book of Abstracts*. 3, 13, 26

[170] Yalçin, Ş., Crosley, D., Smith, G., and Faris, G. W. (1999). Influence of ambient conditions on the laser air spark. *Applied Physics B: Lasers and Optics*, 68(1):121–130. 82

[171] Zare, R., Schmeltekopf, A., Harrop, W., and Albritton, D. (1973). A direct approach for the reduction of diatomic spectra to molecular constants for the construction of RKR potentials. *J. Mol. Spectrosc.*, 46(1):37–66. 49

Appendix

Appendix A

Gaunt Factor

Michel Baranger performed much of the early theoretical development of the calculation of atomic spectral lines shifts and widths (7; 6), which was further developed by Griem (47; 46; 43). Baranger's explanation relied on the impact approximation. This assumes that various perturbing factors interact separately with the perturbed atom or ion and that only the net changes in the perturbed system are significant. In other words, it takes many collisions to produce an appreciable change in the wave functions of the atom.

In considering the impact approximation, Baranger (6) derived a quantum mechanical expression for the width of an isolated ion line in terms of inelastic cross sections.

$$W = N \left\{ \nu \left[\sum_{i'} \sigma_{i'i} + \sum_{f'} \sigma_{f'f} \right] \right\}_{a\nu} + W_{el}. \tag{A.1}$$

Bethe's relation may be used to express the inelastic cross sections,

$$\sigma_{i'i} = \frac{8\pi}{3} \left(\frac{\hbar}{m\nu} \right)^2 \mathbf{R}^2_{j'j} \frac{\pi}{\sqrt{3}} g, \tag{A.2}$$

assuming the dipole approximation. Here, W is the full width at half maximum in units of angular frequency, N is the electron concentration, W_{el} is the line width

contributed by elastic collisions, and $\mathbf{R}^2_{j'j}$ is the square of the coordinated operator matrix element summed over all components of the operator, the magnetic substates of total angular momentum J', and averaged over the magnetic substates of J. For the equation expressing the inelastic cross section, g represents the Gaunt factor. The averaging in the first equation is performed over the electron velocity distribution.

Griem assumed that the contribution of elastic collisions to the line width can be ignored for higher electron temperatures. Griem also to into account elastic collisions at the low temperature limit by using the threshold value of the inelastic cross section below the threshold. The resulting semiempirical formula for calculating the line width is

$$W = N\frac{8\pi}{3}\left(\frac{\hbar}{m}\right)^2\sqrt{\frac{2m}{\pi kT}}\frac{\pi}{\sqrt{3}}\left[\sum_{i'}\mathbf{R}^2_{i'i}g\left(\frac{E}{\Delta E_{i'i}}\right)+\sum_{f'}\mathbf{R}^2_{f'f}g\left(\frac{E}{\Delta E_{f'f}}\right)\right]. \quad \text{(A.3)}$$

$E = \frac{3}{2}kT$ is the energy of the perturbing electron and $\Delta E_{j'j} = |E_{j'} - E_j|$ is the energy difference between levels j and j' (29).

Assuming the Gaunt factor, g, to be constant and by evaluating the summations, the line width (FWHM) in Å then becomes

$$W\left(\text{Å}\right) = 0.4430\cdot 10^{-8}\frac{\lambda^2(cm)N(cm^{-3})}{T^{\frac{1}{2}}}\left(\mathbf{R}^2_{ii}+\mathbf{R}^2_{ff}\right) \quad \text{(A.4)}$$

with

$$\mathbf{R}^2_{jj} = \sum_{j'}\mathbf{R}^2_{j'j} \simeq \frac{1}{2}\left(\frac{n_j}{Z}\right)^2\left[5n_j^2+1-3l_j\left(l_j+1\right)\right]. \quad \text{(A.5)}$$

In the above equation, n_j is the effective principal and l_j the orbital angular momentum quantum number. $(Z-1)$ is the ionic charge.

Dimitrijević and Konjević (29) note that the "semiempirical relation agrees on the average within ±50% with experimental data from singly ionized atoms. Griem suggested that the same expression with an effective Gaunt factor threshold value of 0.2 can be used for multiply-ionized atoms with an error ±100%. However, the

comparison with the experimental values of the line widths of doubly- and triply-ionized atoms shows that the theoretical results are systematically lower. This observation is an indication that the threshold value of 0.2 for the gaunt factor is rather small for higher ionization stages."

At threshold for $\Delta n = 0$, the empirical value for the Gaunt factor is chosen to be

$$g(x) = 0.9 - \frac{1}{Z}. \tag{A.6}$$

For high electron energies, the effective Gaunt factor is expressed as

$$\widetilde{g}(x) = 0.7 - \frac{1.1}{Z} + g(x). \tag{A.7}$$

A lack of atomic data causes difficulties in the evaluation of the needed matrix elements for calculating Stark line widths, especially for multiply-ionized atoms. To overcome this, transitions with $\Delta n = 0$ are handled separately, and the LS coupling approximation is assumed. Thus only two matrix elements are calculated. These two elements correspond to the transition array $l \to l + \mathbf{R}^2_{l,l+1}$ and $l \to l - \mathbf{R}^2_{l,l-1}$. This is in accordance with the procedure used by Griem for semiclassical calculations of multiply charged ion line widths.

$$\begin{aligned} W = N\frac{8\pi}{3}\left(\frac{\hbar}{m}\right)^2\sqrt{\frac{2m}{\pi kT}}\frac{\pi}{\sqrt{3}}\Bigg[&\mathbf{R}^2_{l_i,l_i+1}\widetilde{g}\left(\frac{E}{\Delta E_{l_i,l_i+1}}\right) + \mathbf{R}^2_{l_i,l_i-1}\widetilde{g}\left(\frac{E}{\Delta E_{l_i,l_i-1}}\right) \\ &+ \mathbf{R}^2_{l_f,l_f+1}\widetilde{g}\left(\frac{E}{\Delta E_{l_f,l_f+1}}\right) + \mathbf{R}^2_{l_f,l_f-1}\widetilde{g}\left(\frac{E}{\Delta E_{l_f,l_f-1}}\right) \\ &+ \sum_{i'}\left(\mathbf{R}^2_{ii'}\right)_{\Delta n\neq 0} g\left(\frac{3kTn_i^3}{4Z^2E_H}\right) + \sum_{f'}\left(\mathbf{R}^2_{ff'}\right)_{\Delta n\neq 0} g\left(\frac{3kTn_f^3}{4Z^2E_H}\right)\Bigg], \end{aligned} \tag{A.8}$$

$$\mathbf{R}^2_{l,l'} \simeq \left(\frac{3n}{2Z}\right)^2 \frac{\max[l,l']}{2l+1}\left(n^2 - \max^2[l,l']\right)\phi^2, \tag{A.9}$$

$$\sum_{j'} \left(\mathbf{R}^2_{jj'}\right)_{\Delta n \neq 0} \simeq \left(\frac{3n}{2Z}\right)^2 \frac{1}{9} \left(n_j^2 + 3l_j^2 + 3l_j + 11\right). \tag{A.10}$$

The nearest perturbing level for the inelastic part in the above equations is estimated from

$$\Delta E_{n,n+1} \approx \frac{2Z^2 E_H}{n^3}. \tag{A.11}$$

At high temperatures $\left(\frac{3kT}{2\Delta E} > 50\right)$, all Gaunt factors are calculated in accordance with the GBKO high temperature limit.

$$\widetilde{g}_{j'j} = g_{j'j} = \frac{\sqrt{3}}{\pi} \left[\frac{1}{2} + ln\left(\frac{2ZkT}{n_j^2 \Delta E_{j'j}}\right)\right]. \tag{A.12}$$

Appendix B

Calculation of Potential Energy Curves of Diatomic Molecules: Rydberg-Klein-Rees Method

The Rydberg-Klein-Rees procedure is a semiclassical inversion procedure, typically of first-order. The term inversion procedure is used because unlike the Schrödinger equation, which is solved for eigenfunctions $\Psi_\nu(r)$ and eigenvalues E_n given a specific potential $V(r)$, the RKR method is used to compute the potential curve $V(r)$ for a diatomic molecule, given experimentally observed vibrational energy levels G_ν and inertial rotation constants B_ν. The method emerged from Rydberg's graphical trial-and-error procedure (134), and was mathematically defined by Klein, soon after (64).

Once the potential is known, spectral predictions can be made by solving the one-dimensional Schrödinger equation representing the molecule. In order to compute diatomic molecular potential energy curves with the RKR method, the experimentally determined vibrational constants ω, $\omega\chi$, the coupling constant α, and the rotational constant, B, must be known.

The rotational constant may be expressed by writing the rotational energy,

$$E_{rot} = \kappa(\overline{\frac{1}{r^2}}) = \frac{\kappa}{\tau_\nu} \oint \frac{dt}{r^2} = \frac{\kappa\mu}{\tau_\nu} \oint \frac{dr}{r^2 p_r}. \tag{B.1}$$

Here, τ_ν is the period of vibration, μ is the reduced mass, r is the internuclear separation, p_r is the momentum along the radial direction between the two atoms, and

$$\kappa = \frac{p_\theta^2}{2\mu}, \tag{B.2}$$

where p_θ is the angular momentum which is a constant of motion. Quantization of the angular momentum allows κ to be expressed as,

$$\kappa = \frac{h}{8\pi^2\mu} J(J+1). \tag{B.3}$$

Now, if we express the constant total energy,

$$U = \frac{p_r^2}{2\mu} + V_{eff}(r). \tag{B.4}$$

Letting

$$V_{eff}(r) = V(r) + \frac{\kappa}{r^2}, \tag{B.5}$$

where $V(r)$ is the actual potential and $\frac{\kappa}{r^2}$ is the centrifugal potential, we may solve for p_r in terms of $V_{eff}(r)$, U, and μ. Substituting p_r and our equation for κ into the expression representing the rotational energy,

$$\frac{h}{8\pi^2\tau_\nu\sqrt{2\mu}} \oint \frac{dr}{r^2\sqrt{U - V_{eff}(r)}} = B_\nu. \tag{B.6}$$

It is now important to introduce the classical action,

$$I = \oint p_r dr = \sqrt{2\mu} \oint \sqrt{U - V_{eff}(r)} dr. \tag{B.7}$$

For our purposes, we must apply a quantization to the classical action such that

$$I = h(\nu + \frac{1}{2}) = \sqrt{2\mu} \oint \sqrt{U - V_{eff}(r)} dr. \tag{B.8}$$

This implies a WKB approximation.

We may now express the vibrational and rotational energy, $E(I, \kappa)$, in terms of the action and p_θ^2. If $E(I, \kappa)$ is expressed as quadratic in $I = h(\nu + \frac{1}{2})$,

$$E(I,\kappa) = \omega(\nu+\frac{1}{2}) - \omega\chi(\nu+\frac{1}{2})^2 - \alpha(\nu+\frac{1}{2})J(J+1) + BJ(J+1) + DJ^2(J+1)^2 + \ldots \tag{B.9}$$

The vibrational constants ω and $\omega\chi$ are allowed to vary with energy level, along with the rotational constant, B, and the coupling constant, α. The entire experimental range cannot be represented by this expansion of $E(I, \kappa)$. However, the entire range may be covered by expressing $E(I, \kappa)$ as a quadratic over the different regions comprising the full experimental range. The significance of this sort of expression for the vibrational and rotational energy was pointed out by Rees (130).

It was Klein (64), who modified the procedure introduced by Rydberg (134) to calculate the classical turning points, r_{min} and r_{max}. This calculation is done directly in terms of the functions

$$f = \frac{1}{2}(r_{max} - r_{min}) = \frac{\partial S}{\partial U} \tag{B.10}$$

and

$$g = \frac{1}{2}[\frac{1}{r_{min}} - \frac{1}{r_{max}}] = -\frac{\partial S}{\partial \kappa}. \tag{B.11}$$

The auxiliary function, S, is defined as

$$S(U, \kappa) = \frac{1}{\sqrt{2\pi^2\mu}} \int_0^{I'} \sqrt{U - E(I, \kappa)} dI. \tag{B.12}$$

The upper limit of integration, I', is the value of I for which the integrand vanishes.

Klein introduced the function S because it turns out to be mathematically convenient. However, if the total energy (U) and the potential curve ($V_{eff}(r)$) are plotted as a function of the radial distance (r), S represents half the area between the constant total energy and the potential curve. This can be shown by recalling from classical mechanics that

$$dI = \tau dE \tag{B.13}$$

where

$$\tau = \sqrt{\frac{\mu}{2}} \oint \frac{dr}{\sqrt{E - V_{eff}}}. \tag{B.14}$$

Substituting into the expression for S,

$$S = \frac{1}{2\pi} \int_0^U \sqrt{U - E} [\oint \frac{dr}{\sqrt{E - V_{eff}}}] dE = \frac{1}{2\pi} \oint \int_{V_{eff}}^U \sqrt{\frac{(U - E)}{(E - V_{eff})}} dE dr. \tag{B.15}$$

The lower limit of the integral over dE is changed to V_{eff} because this integral is evaluated at a constant value of r. The integral is of standard form, such that

$$\int_{V_{eff}}^U \sqrt{\frac{(U - E)}{(E - V_{eff})}} dE = \frac{\pi}{2}(U - V_{eff}). \tag{B.16}$$

We may now immediately write,

$$S = \frac{1}{2} \int_{r_{min}}^{r_{max}} (U - V_{eff}) dr = \frac{1}{2} \int_{r_{min}}^{r_{max}} (U - V - \frac{\kappa}{r^2}) dr, \tag{B.17}$$

which is clearly half the area between U and V_{eff}. The integral may further be manipulated

$$S = \frac{1}{2} \int_{r_{min}}^{r_{max}} dr \int_{V_{eff}}^U dE = \frac{1}{2} \int_0^U [r_{max}(E) - r_{min}(E)] dE, \tag{B.18}$$

which upon differentiation provide Klein's original equations for f and g. From this perspective, $2f$ represents the change in the area between U and V_{eff} with respect to a change in U at constant rotational energy, and $2g$ represents the change in this

area with respect to a change in κ (rotational energy) at constant total energy. The equations for f and g may be combined to solve for the classical turning points,

$$r_{\pm} = \sqrt{f^2 + \frac{f}{g}} \pm f. \tag{B.19}$$

The goal of the RKR procedure is to determine r_+ (r_{max}) and r_- (r_{min}) for each of the experimentally observed energy eigenvalues. This is equivalent to knowing the potential $V(r)$, and subsequently the one-dimensional Schrödinger equation may be solved corresponding to the potential curve for the molecule. In order to compute the values of r_+ and r_-, the integral representations for f and g must be solved. This is done numerically by Gaussian integration. Gaussian integration involves the integral being replaced by a weighted finite sum,

$$\int_a^b f(x)dx = \frac{b-a}{2} \sum_{i=1}^{N} w_i f(x_i), \tag{B.20}$$

where w_i are the weights. Specifically, the use of the Gauss-Mehler quadrature formula, first introduced by Tellinghuisen (153, 152), is the preferred method for evaluating this integral. Here, the weight function is chosen to be

$$w(x) = (1-x)^{-\frac{1}{2}}. \tag{B.21}$$

B.1 RKR in Practice

Rather than increasing the number of quadrature points used, the RKR program implemented achieves accuracy with a fixed number of quadrature points in the integration procedure, but repeatedly subdivides the overall integration interval into smaller intervals until the whole integral converges. Dividing the interval in half will yield two types of subintervals due to the singularities of the integral expressions for f and g being at the upper end of the limits of integration. The first interval,

$[\nu_{min}, \frac{(\nu_{min}+\nu)}{2}]$, will have a well behaved integrand, and ordinary Gauss-Legendre quadrature formula is acceptable. For the second interval, $[\frac{(\nu_{min}+\nu)}{2}, \nu]$, the integrand will have the same singular behavior as when the entire interval is treated. For a Gauss-Legendre quadrature scheme, the overall error decreases by a factor of $\frac{1}{2^{N-2}}$ with each subdivision, assuming an N-point quadrature is being performed on each subinterval. After the n^{th} subdivision, only one interval requires Gauss-Mehler points and weights, while the first (2^n-1) subintervals may be evaluated with the Gauss-Legendre procedure.

For insufficient experimental B_ν values for which the integral expression of g cannot be evaluated, directly calculated values of the f integral may be combined with an assumed inner potential wall. In such instances, the inner potential wall may be represented by a Morse function,

$$V_{Morse}(r) = D_e[e^{-\beta(r-r_e)} - 1]^2. \tag{B.22}$$

The corresponding outer turning points are generated by adding values of $2f$ calculated from its integral expression to the Morse function inner turning point at each energy level. The well-depth D_e and exponent parameter β are then provided by the first two derivatives of the vibrational energy at the potential minimum.

B.2 Second Order RKR Solution

The RKR expressions up to terms in second order are

$$A = (\frac{2}{\mu\pi^2})^2 \int_{I_0}^{I'} (U-E)^{1/2} dI - \frac{5h^2}{256\mu\pi^3} \int_{U_0}^{U} (U-E)^{1/2} dE \oint \frac{V_f'^2 dr}{(E-V_f)^{7/2}}, \tag{B.23}$$

$$r_2 - r_1 = (\frac{\partial A}{\partial U})_\kappa, \tag{B.24}$$

$$r_1^{-1} - r_2^{-1} = (\frac{\partial A}{\partial \kappa})_U, \tag{B.25}$$

where U is the energy at the classical turning points r_1 and r_2, $I = h(v + \frac{1}{2})$,

$$\kappa = \frac{h^2}{8\pi^2\mu} J(J+1), \tag{B.26}$$

and the energy $E(I, \kappa)$ is given by the Dunham expansion

$$E = \sum_{i,j} Y_{ij}(v + \frac{1}{2})^i [J(J+1)]^j. \tag{B.27}$$

In an energy versus distance plot A represents the area enclosed by the line of constant energy U and the effective potential curve,

$$V_f = V(r) + \frac{\kappa}{r^2}. \tag{B.28}$$

Interestingly, the evaluation of the second integral in Eq. B.23 requires a knowledge of the very potential of interest. However, this term is expected to be small. Thus, an iterative procedure using the first order results of the WKB approximation to evaluate this term will allow for an improved version of the potential to be obtained (25).

By changing the limits of energy,

$$-\frac{5h^2}{256\mu\pi^3} \int_{U_0}^{U} (U - E)^{1/2} dE = -\frac{5h^2}{256\mu\pi^3} \int_{0}^{U-U_0} (U - U_0 - E)^{1/2} dE, \tag{B.29}$$

with E and V_f also measured from a lower limit of zero. By using the method introduced by Dunham, the variable of integration may be changed from r to V_f,

$$\oint \frac{V_f'^2 dr}{(E - V_f)^{7/2}} = \oint \frac{V_f' dV_f}{(E - V_f)^{7/2}}, \tag{B.30}$$

assuming the derivative of the potential V_f' obtained via first approximation my be represented by a power series in $V_f^{1/2}$.

$$V_f' = A_1 V_f^{1/2} + A_2 V_f + A_3 V_f^{3/2} + A_4 V_f^2 + A_5 V_f^{5/2} + \dots \tag{B.31}$$

Depending on whether considering the left-hand side or the right-hand side of the potential, the $V^{1/2}$ terms will be of opposite sign. Substitution of the above equation for V_f' into Eq. B.30, allows for the first part of the double integral to be evaluated by either Dunham's of Pockhammer's method. The result is

$$\oint \frac{V_f' dV_f}{(E - V_f)^{7/2}} = 4A_5 + 14A_7 E + \frac{63}{2} A_9 E^2 + \dots . \tag{B.32}$$

The area may now be written,

$$A = (\frac{2}{\mu\pi^2})^2 \int_{I_0}^{I'} (U-E)^{1/2} dI + \frac{5h^2}{64\mu\pi^2} [\frac{2}{3} A_5 (U-U_0)^{3/2} + \frac{14}{15} A_7 (U-U_0)^{5/2} + \frac{6}{5} A_9 (U-U_0)^{7/2} + \dots]. \tag{B.33}$$

Appendix C

Parallel Computing on Newton

In order to estimate the error involved with micro-plasma inferences made for individual measurements utilizing the Nelder-Mead algorithm, a gathered spectrum is repeatedly fit assuming an arbitrary baseline offset. The assumed baseline offset is chosen at random within a specified range of the measured offset. The resulting inferences are then analyzed to provide a measure of the variation that can be expected in fitting each spectrum. Alternatively, a collected spectrum can be repeatedly made noisy, by randomly adjusting each point across the spectrum, and fit. Similarly, the resulting inferences are provide a statistical measure of the variation associated with each measurement.

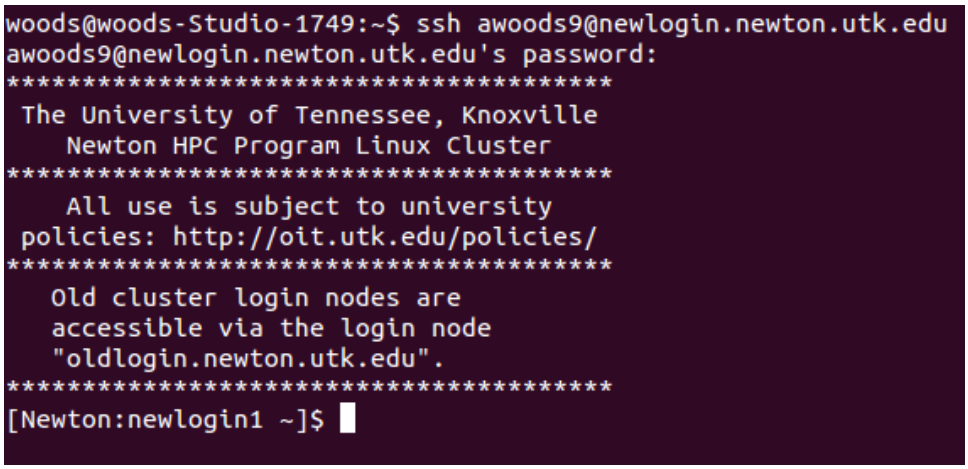

Figure C.1: Image of ssh login to the Newton High Performance Computing cluster.

In order to carry out repeated Nelder-Mead fitting on the many collected spectra, the Newton High Performance Computing (HPC) Program at the University of Tennessee, Knoxville is used. The Newton computing cluster provides a network of machines, which can be repeatedly called upon to carry out computations. In this research, job definition files are created and submitted to the cluster in a batch processing method.

C.1 Preparing Submissions for Cluster

A FORTRAN code is written with the purpose of preparing and submitting each job to the cluster. The program must generate a file containing input parameters for the Nelder-Mead algorithm and a job definition file for each job submitted. The program will then submit the job to the cluster and begin generating the next input file and corresponding job definition file.

C.1.1 Job Definition File

The job definition files contain information specifying the Grid Engine resources that are to be used on each node assigned to the job along with the command to be executed. A typical job definition file might include:

```
#$ -N JobName.sge
#$ -q short*
#$ -cwd
#$ -o null
#$ -e null
mpirun ./NelderMead.mpi <InputFile  >OutputFile
```

Here, the string `#$` precedes all Grid Engine options. The `-N` option will set the name of the job, which will be used to create the output log files for the individual job. `-q` resets the queue to which the job will be sent. `short*` indicates that the

job should be sent to a queue consisting of jobs which require less than 2 hours to execute. The `-cwd` option instructs the Grid Engine to execute the job form the directory in which the job was submitted. The `-o` and `-e` define the paths for the standard output stream and standard error stream of the batch job, respectively. The final line represents the command to be executed. In this example, the executable `NelderMead.mpi` is called using `mpirun` with `<` specifying the file containing the user input for the program and `>` the name of the resulting output file.

The following is an example of a FORTRAN code, which will generate the job description file above.

```
1       program MakeDescriptionFile
        character*8 sge
3       character*9 varfil
        character*10 outfil
5       write(sge,'Name.sge')
        write(varfil,'InputFile')
7       write(outfil,'OutputFile')
        open(1,file=sge)
9       write(1,'("#$ -N Job",a8)') sge
        write(1,'(a12)')'#$ -q short*'
11      write(1,'(a7)')'#$ -cwd'
        write(1,'(a10)')'#$ -o null'
13      write(1,'(a10)')'#$ -e null'
        write(1,'(4a)')'mpirun ./NelderMead.mpi <',varfil,' >',outfil
15      close(1)
```

In the above code, the variable `sge` represents file name given to the job definition file, `Name.sge`. As before, the name of the job is to be `JobName.sge`, the file containing the user input will be named `InputFile`, and the file containing the output will be named `OutputFile`.

C.1.2 Submitting Jobs to Newton

The `qsub` command along with the job definition file are all that is required to submit a job to the cluster.

```
qsub Name.sge
```

Once this has been entered by the user, the job will be placed in a queue. In this context, queue refers to a logical group of machines on which the job may execute. Each queue is defined by the specific resources available on its machines. The contents of the job definition file should contain the desired options of the `qsub` command and specify any additional resources the machine might need. Based upon this information the job will be placed in the appropriate queue.

Before the job is placed in the queue, it will be put in a "pending" state. When resources become available, the Grid Engine will attempt to execute the pending jobs with the highest priority. A job's priority is based on the user's group priority class, the group's historical resource usage, and the user's historical resource usage. The primary factor is the group's priority class. First class groups will have current active monetary contributions to the Newton HPC program. Second class groups will have past monetary contributions to the program, and third class groups will have no history of monetary contributions. The historical resource history of group's and user's is weighted by a seven day half-life of use. The resources used are further compared to the amount of resources guaranteed to the group.

As the job executes, the Grid Engine will generate files containing the job output on the user's home directory. The naming convention for these output files are [job name].[job number]. The `qstat` command and its corresponding options will allow a user to monitor jobs or queues.

C.1.3 Submitting Jobs in Batch

For this research, each measured spectrum is fit with computed diatomic molecular spectra using a Nelder-Mead algorithm. The algorithm allows for a multi-parameter fit, which is used to infer the micro-plasma parameters of the diatomic molecular emissions observed in the collected spectra. For the purposes of error analysis, one of the fitted parameters is selected for further investigation to determine its affect on the fitting of another parameter. In the most common case, the effect of the baseline offset on inferred temperature is studied. In this situation, the best fitting parameters are first determined. Then, the parameter whose affect is to be studied (baseline offset) is varied from its best fitting value. As the spectrum is fit again, this new value will be fixed along with all the other best fitting values except the one of interest (temperature). This process is repeated until there are a reasonable number of results for a statistical analysis.

In order to achieve this type of error analysis with Newton, the Nelder-Mead program is submitted to a machine in the cluster along with the input parameters for the fitting routine and the experimental spectrum. This is done for each varied value of the parameter under investigation. The values of the varied parameters are arbitrarily chosen within a specified percentile of the best fitting value. A single program is responsible for assigning this value, generating a file containing input parameters, creating a job description file, and submitting it to the queue. The following is an example of FORTRAN code for such a program.

```
1       program control
        integer bytes
3       character*13 txt
        character*14 sge
5       character*10 inpfil, varfil, outfil, expfil, datfil
        character*17 resfil
7       character*100 command, command2
        iseed = 1
9       call gettim(ihr,im,is,ihs)
```

```
        iseed=60*im+is
        if(iseed/2*2.eq.iseed)iseed=iseed+1
        doj=1,50                        !Number of experimental files
        doi=1,1000                              !Number of iterations
        if(i.gt.1001.or.j.gt.99)Stop 'i or j too large!'
!!!!!!!!!!!!!!!!!!!!!!!!!!!!!!!!!!!!!!!!!!!!!!!!!!!!!!!!!!!!!!!!!!!!!!!
!   Prepare files
!!!!!!!!!!!!!!!!!!!!!!!!!!!!!!!!!!!!!!!!!!!!!!!!!!!!!!!!!!!!!!!!!!!!!!!
        if(j.le.9)then
          write(inpfil,10)j,'.inp'
          write(expfil,10)j,'.txt'
          write(sge,'("TiO",I1.1,"i0000.sge")')j
          write(varfil,10)j,'inp.0000'
          write(datfil,10)j,'dat.0000'
          write(outfil,10)j,'out.0000'
          write(resfil,'("TempResults",I1.1,".txt")') j
        else
          write(inpfil,101)j,'.inp'
          write(expfil,101)j,'.txt'
          write(sge,'("TiO",I2.2,"i0000.sge")')j
          write(varfil,101)j,'inp.0000'
          write(datfil,101)j,'dat.0000'
          write(outfil,101)j,'out.0000'
          write(resfil,'("TempResults",I2.2,".txt")')j
        endif
        if(j.le.9)then
          write(datfil(6:9),'(I4.4)')i
          write(varfil(6:9),'(I4.4)')i
          write(outfil(6:9),'(I4.4)')i
          write(sge(6:9),'(I4.4)')i
        else
         write(datfil(7:10),'(I4.4)')i
         write(varfil(7:10),'(I4.4)')i
         write(outfil(7:10),'(I4.4)')i
```

```
          write(sge(7:10),'(I4.4)')i
        endif
!!!!!!!!!!!!!!!!!!!!!!!!!!!!!!!!!!!!!!!!!!!!!!!!!!!!!!!!!!!!!!!!!!!!!!!!
        open(1,file=inpfil)
        open(2,file=varfil)
        open(4,file=expfil)
        open(5,file=datfil)
 10     format(I1,a)
 101    format(I2,a)
!!!!!!!!!!!!!!!!!!!!!!!!!!!!!!!!!!!!!!!!!!!!!!!!!!!!!!!!!!!!!!!!!!!!!!!!
!  Add noise to the experimental file
!!!!!!!!!!!!!!!!!!!!!!!!!!!!!!!!!!!!!!!!!!!!!!!!!!!!!!!!!!!!!!!!!!!!!!!!
!         don=1,1024                                              !Loop to
!         rx=ran(iseed)                                          !generate
!         read(4,*)x,y                                             !noise
!         write(5,*)x,y*(1.+(2.*rx-1.)*0.25)
!         enddo
!         write(2,'(a)')datfil                        !Write to input file
!         read(1,'(a)')txt                                    !Read 1st line
!         don=1,19              !NO EXCLUSION="1,19": EXCLUSION="1,22"
!              read(1,'(a)')txt                                    !Loop to
!              write(2,'(a)')txt                             !create noise
!         enddo                                                  !input file
!!!!!!!!!!!!!!!!!!!!!!!!!!!!!!!!!!!!!!!!!!!!!!!!!!!!!!!!!!!!!!!!!!!!!!!!
!  Randomly adjust the assumed background for NMT
!!!!!!!!!!!!!!!!!!!!!!!!!!!!!!!!!!!!!!!!!!!!!!!!!!!!!!!!!!!!!!!!!!!!!!!!
         don=1,13              !NO EXCLUSION="1,13": EXCLUSION="1,16"
              read(1,'(a)')txt
              write(2,'(a)')txt
         enddo
        read(1,*)bkg
        bkgout=bkg*(1.+(2.*ran(iseed)-1.)*0.25)
        write(*,*)bkgout
        write(2,*)bkgout
```

```
          dom=1,6
79              read(1,'(a)')txt
                write(2,'(a)')txt
81         enddo
!!!!!!!!!!!!!!!!!!!!!!!!!!!!!!!!!!!!!!!!!!!!!!!!!!!!!!!!!!!!!!!!!!!!!!!!!!!!!!!
83        close(1)
          close(2)
85        close(4)
          close(5)
87!!!!!!!!!!!!!!!!!!!!!!!!!!!!!!!!!!!!!!!!!!!!!!!!!!!!!!!!!!!!!!!!!!!!!!!!!!!!!!!
!   Make a description file for qsub
89!!!!!!!!!!!!!!!!!!!!!!!!!!!!!!!!!!!!!!!!!!!!!!!!!!!!!!!!!!!!!!!!!!!!!!!!!!!!!!!
          open(3,file=sge)
91        write(3,'("#$ -N Job",a14)') sge
          write(3,'(a12)')'#$ -q short*'
93        write(3,'(a7)')'#$ -cwd'
          write(3,'(a10)')'#$ -o null'
95        write(3,'(a10)')'#$ -e null'
          write(3,'(4a)')'mpirun ./NelderMead.mpi <',varfil,' >',outfil
97        close(3)
!!!!!!!!!!!!!!!!!!!!!!!!!!!!!!!!!!!!!!!!!!!!!!!!!!!!!!!!!!!!!!!!!!!!!!!!!!!!!!!
99        write(command,'(3a)')'qsub ',sge
           call system(command)              !Submit description file
101       enddo
!!!!!!!!!!!!!!!!!!!!!!!!!!!!!!!!!!!!!!!!!!!!!!!!!!!!!!!!!!!!!!!!!!!!!!!!!!!!!!!
103       call system(' qstat >Queue')              !Check completion
          inquire(file='Queue', size=bytes)
105       do while(bytes.ne.0)                              !Wait until
            call system(' qstat >Queue')             !job is finished
107         inquire(file='Queue', size=bytes)
          enddo
109!!!!!!!!!!!!!!!!!!!!!!!!!!!!!!!!!!!!!!!!!!!!!!!!!!!!!!!!!!!!!!!!!!!!!!!!!!!!!!!
          write(command2,'(3a)')'cat F*.dat >> ',resfil
111       call system(command2) !Put TempResults into a file
```

```
        call system(' rm F*.dat') !Remove individual TempResults
113     enddo
        end
```

The above program is written to perform one thousand iterations of the fitting routine on fifty experimentally obtained spectra, as the variable `i` is summed over the number of experimental files and `j` over the number of iterations of the fitting routine. As the code is written, it will randomly select a baseline offset as a fitting input parameter within 25 % of its best fitting value for each iteration. The code can readily be altered to randomly adjust each pixel of an experimentally obtained spectrum by removing the `c`'s preceding the lines of the corresponding block of code. By doing this and then commenting out the block of code altering the baseline offset, the program will perform one thousand iterations of the fitting routine on the experimental spectra with simulated noise. This is particularly useful in analyzing LIBS measurements resulting from a single laser pulse.

The code is written so that no spectral region of the experimental file is excluded from the fitting routine. However, it is possible to modify the code such that there is an exclusion region. To do this, the input file (`1.inp`) must be written to provide the fitting routine with the wavelength range for the exclusion region. Also, the above code must be modified as indicated in the commented sections of the code.

The files generated by this program containing input and output for the Nelder-Mead algorithm follow specific naming conventions. These conventions are chosen so that when the program has finished it is obvious which input and output files belong with one another. For instance, the first experimentally obtained spectrum will be in a file named `1.txt`. The file containing the previously determined best fitting input parameters will be titled `1.inp`. If the program is to find error associated with varying the baseline offset, the baseline input parameter will be arbitrarily adjusted for each fitting iteration. The file providing this adjusted baseline along with the best fitting input parameters to the Nelder-Mead program will be named `1inp.0001`, for

the first iteration. Likewise, the corresponding output will be in a file `1out.0001`. A two column list of the assumed baselines and corresponding inferred temperatures for all the iterations performed using the first experimental spectrum will be located in a file named `TempResults1.txt`. If the program is to find the error associated with a noisy spectrum, each pixel of the experimental spectrum will be arbitrarily adjusted within a specified percentage of its actual value. For the first iteration of the first experimental spectrum, the file containing the noisy spectrum will be named `1dat.0001`.

The last eleven lines of code check to see if the submitted jobs have been submitted to a node from the queue. This step is important when submitting jobs by the thousands. The Newton cluster restricts each user to the number of jobs which that user may have waiting in the queue at any given time. In this section, `command2` places the assumed baselines and inferred temperatures of each iteration into a single folder for the experimental spectrum. Then the files containing results of individual iterations are removed.

C.2 Analysis of Results

The goal of this procedure is to quantify the error involved with a temperature inference from each measured spectrum. To accomplish this, the collection of temperatures inferred by adjusting the spectral baseline is treated as a normal distribution. The three-sigma rule is then used to determine the standard deviation of the inferred temperatures for each measured spectrum. The resulting output of the FORTRAN code above will consist of a file containing one thousand baselines and their corresponding inferred temperatures for each of the fifty measured spectra. Thus, it is again useful to perform these computations in batch.

First a program is written to determine the standard deviation for each measurement. The three-sigma rule states that approximately 68.27 % of the values in a normal distribution will be within one standard deviation of the mean. Likewise,

95.45 % and 99.73 % will be within two and three standard deviations of the mean, respectively. Recall the inferred temperatures correspond to a spectral baseline randomly chosen within a specified range of the measured baseline. Thus, the mean value for the temperature will be chosen to be the temperature inferred assuming the measured baseline offset. Using the three-sigma rule to determine the standard deviation requires the program to find the temperature range for which 68.27 % of the inferred temperatures reside. For this, a python code is used.

```
import numpy as np
from scipy.stats import norm
import matplotlib.pyplot as plt
import matplotlib.mlab as mlab

################################ WHAT FILE CONTAINS TEMPERATURE MEASUREMENT
print('Provide an Input file name:')
inpfil = raw_input()
###################### WHAT FILE CONTAINS INFERRED TEMPERATURES/BASELINES
print('Provide a TempResults name:')
resfil = raw_input()
################################## NAME THE OUTPUT FILES CONTAINING ANALYSIS
anafil = 'Analysis' + resfil
s = list(resfil)
s[-3] = 'p'
s[-2] = 'n'
s[-1] = 'g'
pltfil = "".join(s)
######################################### INITIALIZE THE COUNTING VARIABLES
count = 0
j = 0
k = 0
l = 0
############################################ READ FILES AND ASSIGN VARIABLES
measure = np.loadtxt(inpfil, dtype=str, unpack=True)
measurement = float(measure[-2])
```

```
T, b0 = np.loadtxt(resfil, unpack=True)
Temp = abs(T)
Tmax = max(Temp)
Tmin = min(Temp)
############################ FIND 1-SIGMA, 2-SIGMA, and 3-SIGMA BY COUNTING
while count < 682.7:
    count = 0
    for i in range(len(Temp)):
        if Temp[i] <= measurement+j and Temp[i] >= measurement-j:
            count = count + 1
    j = j + 1

count = 0
while count < 954.5:
    count = 0
    for b in range(len(Temp)):
        if Temp[b] <= measurement+k and Temp[b] >= measurement-k:
            count = count + 1
    k = k + 1

count = 0
while count < 997.3:
    count = 0
    for c in range(len(Temp)):
        if Temp[c] <= measurement+l and Temp[c] >= measurement-l:
            count = count + 1
    l = l + 1
############################################ WRITE RESULTS IN OUTPUT FILE
w = open(anafil, 'w+')
w.write('For a measured temperature of %i K: 1-sigma p/m %i K, 2-sigma p
    /m %i K, 3-sigma p/m %i K' % (measurement, j, k, l))
w.close()
########################################################## MAKE A HISTOGRAM
```

```
m, bins, patches = plt.hist(Temp, 100, normed=True, facecolor='g', alpha
    =0.75)

(mu, sigma) = norm.fit(Temp)
y = mlab.normpdf( bins, mu, sigma)
l = plt.plot(bins, y, 'r--', linewidth=2)

plt.xlabel('Temperature (K)')
#plt.ylabel('Percentage')
plt.title('Temperature Analysis: $\mu=%.3f,\ \sigma=%.3f$' % (mu, sigma)
    )
#plt.axis([Tmin-100, Tmax+100, 0, 1.5])
plt.grid(True)
plt.savefig(pltfil, bbox_inches=0)
#plt.show()
```

The output of the python code above will produce a `.txt` file containing the temperature values representing the 1-σ, 2-σ, and 3-σ ranges. Also, the program will produce a `.png` file containing a histogram of the inferred temperatures over all of the iterations. An example of such a histogram is shown as Figure C.2.

In order to efficiently analyze the temperature distributions for multiple spectral measurements, it is useful to write another code responsible for repeatedly calling the program for analysis and providing it with the necessary files. For this, a FORTRAN code is written.

```
      program pycon
      character*10 varfil
      character*17 resfil
      doj=1,50
       if(j.le.9)then
        write(varfil,10)j,'inp.0001'
        write(resfil,'("TempResults",I1.1,".txt")')j
       else
        write(varfil,101)j,'inp.0001'
```

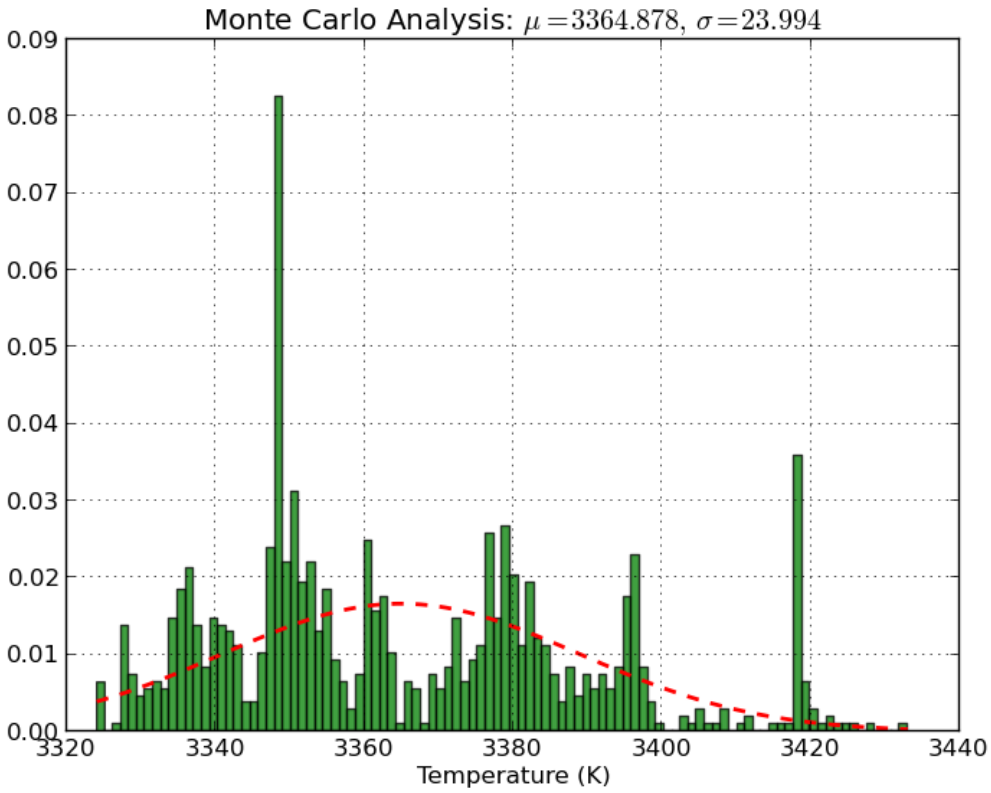

Figure C.2: Sample `.png` output of temperature analysis program.

```
          write(resfil,'("TempResults",I2.2,".txt")')j
11        endif
10        format(I1,a)
13  101   format(I2,a)
          open(1,file='doc')                    !Make an input file with
15        write(1,'(a)')varfil                  !measured temperature
          write(1,'(a)')resfil                  !and inferred temp/baseline
17        close(1)
          call system(' python Analysis.py <doc')       !Call analysis
19      enddo
        end
```

Appendix D

Andor iStar ICCD Analysis

In this research, an Andor iStar ICCD camera is implemented as a means of gated detection for LIBS. The ICCD is fixed to the aperture at the exit of the Jobin-Yvon spectrograph. Thus, the ICCD serves to capture a time-gated spectroscopic image of the laser-induced event. The iStar communicates via a USB cable to a computer operating the Andor iStar software dedicated to both controlling the ICCD and organizing the output from the ICCD. A typical image produced by the Andor iStar consists of 1024×1024 pixels. However, the acquisition settings for the camera allow for the binning of regions of the detector. By binning, the 1024 horizontal tracks may be grouped into a smaller number of tracks in which the counts at each pixel will be vertically summed for each member of a group. For example, the detector may be organized into one track, causing the ICCD to behave as a linear diode array.

The image compiled by the Andor software can be exported as an ASCII file for further analysis. Each horizontal track of the image is represented as a column in the ASCII file. For multiple images gathered over a single series of collection times, the output of every image will be contained in a single ASCII file. A Python program is used to organize the content of the ASCII files provided by the Andor software. This program is responsible for reading the ASCII file, separating each track into a corresponding Python list, wavelength and sensitivity correcting each track, and

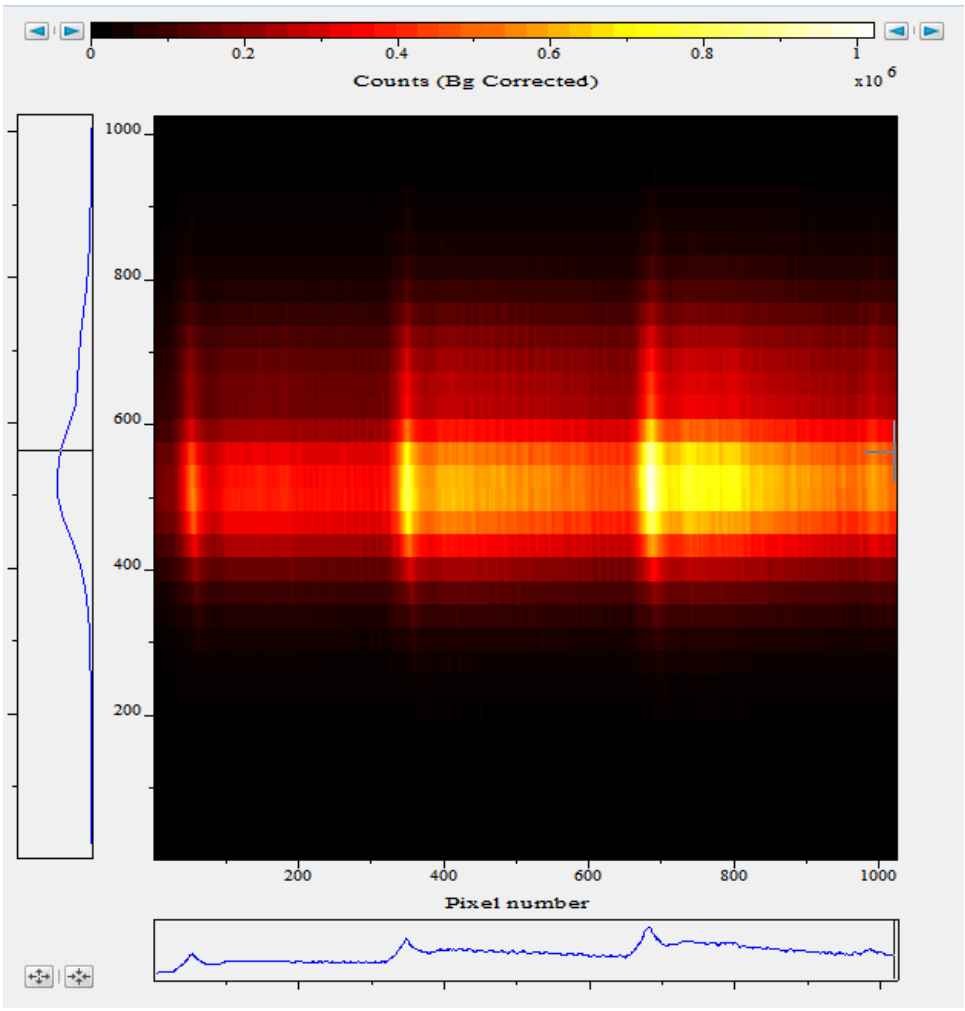

Figure D.1: Andor iStar image of TiO $A^3\Phi \rightarrow X^3\Delta$ at 705-715 nm 100 μs after laser-induced breakdown. The image is binned into 32 horizontal tracks with a height of 32 pixels.

generating new files containing each track. Thus, the Python program is responsible for providing files containing calibrated experimental data for each vertical region of the detector for every measurement in a data collection series.

In this research, these files are analyzed differently depending on the purpose of each experimental run. Collected spectra displaying diatomic molecular transitions will be analyzed by means of a Nelder-Mead fitting routine. Atomic spectral transitions, gathered to infer electron density, will be fit with a Lorentzian profile by means of least square fitting. In both cases, the ICCD is often programmed to bin

regions into multiple tracks. Thus, the analysis of both types of measurements lends itself to batch processing.

D.1 Organizing and Calibrating Data

D.1.1 Reading Data

The Python code written to organize the content of the ASCII files provided by the Andor software begins by reading the ASCII file. If the user has selected to append information regarding the ICCD acquisition settings, as available when exporting an ASCII file with the Andor software, the Python program will read this appended portion to get the number of tracks and the height of each track. If the user chooses not to append this information, the Python program will infer the number of tracks and track height by the dimensions of the columns of data in the ASCII file. The program will then create a matrix containing the counts for each horizontal pixel of every track. A separate list will also be created containing the pixel numbers (i.e. 1,2,...1024).

D.1.2 Wavelength Calibration

The wavelength dispersion provided by the Jobin-Yvon spectrometer will vary as a function of height along the detector attached at its exit aperture. Therefore, for an accurate wavelength calibration along the height of the iStar image, each track must be calibrated individually. This can be achieved by imaging a calibration lamp, appropriately chosen for the wavelength region of the measurement, using the same binning settings as used to capture the experimental image. Using the documented location of the spectral lines of the lamp, the horizontal pixels of the image can be represented by their corresponding wavelength. Since the dispersion varies as a function of height, the horizontal pixel location of a given transition line may vary with height for multi-track images. While the horizontal wavelength dispersion of the

Jobin-Yvon spectrometer is nearly linear, a cubic interpolation is often used to assign a wavelength to individual pixels.

In practice, there are two methods of achieving a wavelength calibration along the height of an image. For every track of the image, the wavelength calibration process may be performed by using the spectral calibration lamp to assign wavelengths to the pixel locations of observed spectral lines and then interpolating to assign a wavelength to each horizontal pixel. Alternatively, the spectral lamp can be used to assign a wavelength to each horizontal pixel of a single track and the wavelength dispersion as a function of height can be used to apply this calibration to the other tracks. In order to use the second method, the variation of the wavelength dispersion as a function of height along the detector must first be determined. To determine this variation, structural features in the spectra of adjacent tracks are compared to one another. By noting the horizontal pixel location of the common features in adjacent tracks, the variation in wavelength dispersion along the height of the detector can be determined. This procedure can be performed by imaging the output of a spectral calibration lamp or it can be performed on the experimental data itself, as outlined in the next section.

In most cases of experimental data, the brightest track will correspond to the center of the laser-induced plasma being observed. By summing the number of counts across each track, the program will determine which track is the brightest. The wavelength calibration will initially be performed on the brightest track. This track will then serve as a reference for determining the variation of the wavelength dispersion of the spectrometer as a function of height. The counts for the pixels of the brightest track are compared with its adjacent tracks by means of linear least squares fitting. This fitting will determine if the features of the reference track appear shifted in an adjacent track, and if so by what extent. If necessary, a correction will be applied in the conversion of the horizontal pixels to wavelengths. This process is repeated for all adjacent tracks comprising an image. While spectra of adjacent tracks are not expected to be equal, in many instances their structure is expected to display similar

features on the whole. Exceptions to this will most often occur for the dimmest of tracks, which image regions beyond the plasma.

Due to the many transition lines present in the emission spectra of diatomic molecules, an accurate wavelength calibration is required if spectra computed from theory is to be fit to the experimentally obtained spectra. While the use of calibration lamps are the preferred approach to wavelength calibrating spectra, there are some wavelength regions of interest where the appropriate calibration lamp may only have one or two spectral lines. In this scenario, the spectral region can be incrementally adjusted by the spectrometer, as the line or lines from the calibration lamp are tracked by capturing images of their location within each spectral region. By keeping track of how the pixel location of each line changes as the spectrometer is swept across a spectral region, the wavelength dispersion of the spectrometer for a given spectral range can be obtained. Because this process can be time consuming, another method for wavelength calibrating such a precarious region has been incorporated into the Python code for handling the ASCII files.

This alternative method for wavelength calibrating spectra containing diatomic transitions involves using computed diatomic spectra as a reference. This is achieved by first generating a diatomic spectrum from theory over the observed spectral region. Then, the positions of the transition lines of the measured spectra are fit to those of the computed spectrum. While the values of parameters used for generating the computed spectrum should be chosen as the values expected to be characteristic of the experimental measurement, the accuracy of the assumed parameters has not been seen to alter the effectiveness of the calibration method.

D.1.3 Sensitivity Correction

If the user chooses to perform a sensitivity calibration for the data contained in the ASCII file, an intensity calibration lamp must be observed with the iStar using the same binning settings as the data to be analyzed. The ASCII file corresponding to

the image of the calibration lamp must be provided to the Python program as well as either a blackbody curve computed from the measured temperature of the lamp or the lamp's calibration data provided by the manufacturer.

The sensitivity correction will be performed by first gathering the data from the ASCII file corresponding to the observed lamp in the same manner as described above for the ASCII file containing experimental data. As the program goes through each track of the experimental data to perform the wavelength calibration, the spectrum for each corresponding track of the lamp's image will be compared to either the blackbody curve or lamp's calibration data provided. The comparison is done by determining the intensity ratio for each pixel of the spectrum when compared to the calibration curve. These ratios are then applied to the corresponding track of the experimental data, resulting in the sensitivity correction of that track.

D.1.4 Example Code

An example of the Python code responsible for preparing the information contained in an Andor iStar ASCII file is presented below. The main function of this code is to read the Andor ASCII file and put each track into an individual file. However, this code also contains options regarding all the bells and whistles associated with using the iStar for diatomic spectral analysis. The options available within the code include a sensitivity correction provided an ASCII file measuring the intensity calibration lamp and a wavelength calibration either by using measured lines from a spectral lamp or a computed diatomic spectrum covering the region observed. The code will also produce an figure of the image with the intensity profile as a function of height on the detector plotted to the left of the image. Additionally, if the data has already been analyzed for temperature inferences, the code will read in the information from the file containing the temperature results and plot them to the left of the image. This code was used to produce figures such as Figures 4.15-4.24.

```
# -*- coding: utf-8 -*-
```

```
"""
Created on Thu Dec 05 15:04:37 2013

@author: Woods
"""

import numpy as np
from scipy.optimize import leastsq
from scipy.optimize import minimize
from scipy import interpolate
import matplotlib.pyplot as plt
import matplotlib.gridspec as gridspec
from math import log10, floor

goodfile = 'Track17.txt'
calib, intens = np.loadtxt(goodfile,unpack=True)

w00=0
for p00 in range(1,2):
    for q00 in range(1,11):
        w00 = w00 + 1
        if q00 < 10:
################################################## NAME OF ANDOR ASCII FILE
            ascfil = 'Ti712nm3072gain200scan20-200mics000%i.asc' %q00
        else:
################################################## NAME OF ANDOR ASCII FILE
            ascfil = 'Ti712nm3072gain200scan20-200mics00%i.asc' %q00
################################### NAME OF DIATOMIC FILE FOR CALIBRATION
        #fit = 'TiO704-7-716-5.txt'
################################### =True to calibrate      =False otherwise
        IntensityCalibrate = True

        if (IntensityCalibrate == True):
################################################## NAME OF MEASURED LAMP FILE
```

```
36              bkgfile = '712nm3072gain200scan1milliLAMP.asc'
    ################################################ NAME OF CALIBRATION FILE
38              LSfile = 'Blackbodypix487=712.0.txt'
                meas = bkgfile[:-4]
40              LSx, LSy = np.loadtxt(LSfile, unpack=True)
                z = [None]*1024
42              lampy = [None]*1024
            def resid(p0, yew, n0):
44              fact = p0
                err0 = yew - fact * n0
46              return err0

48          fil = ascfil[:-4]
            i=0
50          j=0
            n=0
52          g = [None]*1024
            pix = [None]*1024
54          y = [None]*1024
            xp1 = [None]*1024
56  ########################################################## OPEN ASCII FILE
            f = open(ascfil, 'r')
58          h = f.readlines()
            f.close()
60          for i in range(len(h)):
                h[i] = str(h[i])
62          if (IntensityCalibrate == True):
                ff = open(bkgfile, 'r')
64              k = ff.readlines()
                ff.close()
66              for i in range(len(k)):
                    k[i] = str(k[i])
68  ############################################## GET NUMBER OF TRACKS/HEIGHT
            l1 = [s for s in h if 'Number of Tracks:' in s]
```

```
70          if l1:
                l1 = str(l1[0])
72              l2 = [s for s in h if 'Track Height:' in s]
                if l2:
74                  l2 = str(l2[0])
                    height = int(l2[-6:-1])
76                  print(height)
                tracks = int(l1[-6:-1])
78              print(tracks)
#################################################################### FILL MATRIX
80          for i in range(1024):
                g[i] = h[i].split('\t')
82              if '\n' in g[i]: g[i].remove('\n')
                g[i] = map(float, g[i])
84          d = [g[i] for i in range(1024)]
            if (IntensityCalibrate == True):
86              for i in range(1024):
                    z[i] = k[i].split('\t')
88                  if '\n' in z[i]: z[i].remove('\n')
                    z[i] = map(float, z[i])
90              e = [z[i] for i in range(1024)]
#################################################################### GET PIXELS
92          for j in range(1,len(g[i])):
                for i in range(1024):
94                  pix[i] = int(d[i][0])
                    d[i][j] = int(d[i][j])
96          if (IntensityCalibrate == True):
                for j in range(1,len(z[i])):
98                  for i in range(1024):
                        e[i][j] = float(e[i][j])
100 ################################################## FIND THE BRIGHTEST TRACK
            a = [sum(x) for x in zip(*d)]
102         center = a.index(max(a))
            print(center)
```

```
104         xpx = [None]*1024
            xpy = [None]*1024
106         for i in range(len(g)):
                y[i] = d[i][center]
108 ##########################################################################
    #                       WAVELENGTH CALIBRATE CENTER ROW
110 ##########################################################################
    ######################################## READ BESP PLOT FOR WAVELENGTH REGION
112 #           fitx, fity = np.loadtxt(fit, delimiter=',',unpack=True)
    #           minwave = float(min(fitx))
114 #           maxwave = float(max(fitx))
    ############################################ DEFINE FUNCTION TO GET RESIDUALS
116         def Wavelength(region,fix,fiy,exy):
                res = [None]*1024
118             x = [None]*1024
                wavemin = min(fix)
120             wavemax = max(fix)
    ###################################### ADD ZEROS TO ENDS OF THEORY SPECTRUM
122             dx = np.arange(wavemin-2,wavemin+1,1)
                ex = np.arange(wavemax,wavemax+2,1)
124             for i in range(len(dx)):
                    fx = np.insert(fix,0,dx[-i-1])
126                 fy = np.insert(fiy,0,0)
                    #np.append(fix,ex)
128             for i in range(len(ex)):
                    fx = np.append(fix,ex[i])
130                 fy = np.append(fiy,0)
    ################################################## SETUP CUBIC FOR FITTING
132             for i in range(1024):
                    x[i] = region[0]*i**3 + region[1]*i**2 + region[2]*i +
    region[3]
134 ############################################################ FIND RESIDUALS
                tck = interpolate.splrep(fx,fy,k=1)
136             yu = interpolate.splev(x,tck,der=0)
```

```
            res = (yu - exy)**2
138         sm = sum(res)
            return sm
140 ############################ DEFINE FUNCTION TO DETERMINE SLOPE SEED VALUE
#       def linear(m,b,expy,fity):
142 #           x = [None]*1024
#           q = [None]*1024
144 #           for j in range(len(x)):
#               x = m*j + b
146 #           tck = interpolate.splrep(fitx,fity,k=1)
#           yu = interpolate.splev(x,tck,der=0)
148 #           q = (yu - expy)**2
#           return q
150 ################################################## GET ESTIMATE FOR SLOPE
#       step = (maxwave-minwave)/1024
152 #       print(step)
    ################################################## FIT TO LINE TO FIND SLOPE
154 #       slope, cov = leastsq(linear, step, args=(minwave,y,fity))
#       print(slope)
156 ######################################## FIT TO FIND WAVELENGTH MIN AND MAX
#       region = [0.0,0.0,slope[0],minwave,maxwave]
158 #       #print(len(fitx) !=len(set(fitx)))
#       #print(len(fity) !=len(set(fity)))
160 #       #print(len(y) !=len(set(y)))
#       length = minimize(Wavelength,region,args=(fitx,fity,y),method='
    nelder-mead',options={'xtol': 1e-8, 'disp': True})
162 #       done = [None]*5
#       done = length.x
164 #       print(done)
    ################################################## REPLACE EXP FILE X-VALUES
166 #       calib = [None]*1024
#       for i in range(1024):
168 #           calib[i] = done[0]*i**3 + done[1]*i**2 + done[2]*i + done
    [3]
```

```
##############################################################################
#                WAVELENGTH CALIBRATE THE OTHER TRACKS
##############################################################################
########################## DEFINE FUNCTION TO LINEARLY FIT ADJACENT TRACKS
        def residuals(m,b,expy,fitty):
            x = [None]*1024
            q = [None]*1024
            for j in range(len(x)):
                x = m*j + b
            tck = interpolate.splrep(pix,fitty,k=1)
            why = interpolate.splev(x,tck,der=0)
            q = (why - expy)**2
            return q
        step1 = (float(max(pix))-float(min(pix)))/len(pix)
################################ COMPARE PIXEL DISPERSION OF ADJACENT TRACKS
##################################### AND APPLY TO WAVELENGTH CALIBRATION
        if (IntensityCalibrate == True):
            dcal = d
        for n in range(1,len(g[0])):
        #    m=0
            if (n<center):
                for i in range(1024):
                    xpy[i] = d[i][n]
                    xp1[i] = d[i][n+1]
                    if (IntensityCalibrate == True):
                        if (e[i][n]==0.0):
                            e[i][n] = 0.000001
                        lampy[i] = e[i][n]
                sl, cov = leastsq(residuals, step1, args=(min(pix),xpy,
    xp1))
                for i in range(len(pix)):
                    xpx[i] = sl[0] * i + min(pix)
                tck = interpolate.splrep(pix,calib,k=3)
                newx = interpolate.splev(xpx,tck,der=0)
```

```
202 #                 newx, dum = np.loadtxt('Track%i.txt' %n,unpack=True)
                    datout = np.column_stack((newx, xpy))
204                 saveAS = fil +'Track%i.txt' % n
                    np.savetxt(saveAS, datout)
206                 if (IntensityCalibrate == True):
                        wck = interpolate.splrep(LSx,LSy,k=3)
208                     ynew = interpolate.splev(newx,wck,der=0)
                        resi = leastsq(resid, 250, args=(lampy, ynew))
210                     BB = resi[0] * ynew
                        cal = BB / lampy
212                     calibrated = xpy * cal
                        for i in range(1024):
214                         dcal[i][n] = calibrated[i]
                        dataout2 = np.column_stack((newx, calibrated))
216                     saveAS2 = fil + 'IntCal%i.txt' % n
                        np.savetxt(saveAS2, dataout2)
218                     datout3 = np.column_stack((newx, lampy))
                        saveAS3 = meas +'Track%i.txt' % n
220                     np.savetxt(saveAS3, datout3)
                if (n==center):
222                 for i in range(1024):
                        xpy[i] = d[i][n]
224                     if (IntensityCalibrate == True):
                            if (e[i][n]==0.0):
226                             e[i][n] = 0.000001
                            lampy[i] = e[i][n]
228 #                newx, dum = np.loadtxt('Track%i.txt' %n,unpack=True)
    #                 calib = newx
230                 datout = np.column_stack((calib, xpy))
                    saveAS = fil +'Track%i.txt' % n
232                 np.savetxt(saveAS, datout)
                    if (IntensityCalibrate == True):
234                     jck = interpolate.splrep(LSx,LSy,k=3)
                        ynew = interpolate.splev(calib,jck,der=0)
```

```
                    resi = leastsq(resid, 250, args=(lampy, ynew))
                    BB = resi[0] * ynew
                    cal = BB / lampy
                    calibrated = xpy * cal
                    for i in range(1024):
                        dcal[i][n] = calibrated[i]
                    dataout2 = np.column_stack((calib, calibrated))
                    saveAS2 = fil + 'IntCal%i.txt' % n
                    np.savetxt(saveAS2, dataout2)
                    datout3 = np.column_stack((calib, lampy))
                    saveAS3 = meas +'Track%i.txt' % n
                    np.savetxt(saveAS3, datout3)
            if (n>center):
                for i in range(1024):
                    xpy[i] = d[i][n]
                    xp1[i] = d[i][n-1]
                    if (IntensityCalibrate == True):
                        if (e[i][n]==0.0):
                            e[i][n] = 0.000001
                        lampy[i] = e[i][n]
                sl, cov = leastsq(residuals, step1, args=(min(pix),xpy,
    xp1))
                for i in range(1024):
                    xpx[i] = sl[0] * i + min(pix)
                ick = interpolate.splrep(pix,calib,k=3)
                newx = interpolate.splev(xpx,ick,der=0)
#                newx, dum = np.loadtxt('Track%i.txt' %n,unpack=True)
                datout = np.column_stack((newx, xpy))
                saveAS = fil +'Track%i.txt' % n
                np.savetxt(saveAS, datout)
                if (IntensityCalibrate == True):
                    pck = interpolate.splrep(LSx,LSy,k=3)
                    ynew = interpolate.splev(newx,pck,der=0)
                    resi = leastsq(resid, 250, args=(lampy, ynew))
```

```
                    BB = resi[0] * ynew
                    cal = BB / lampy
                    calibrated = xpy * cal
                    for i in range(1024):
                        dcal[i][n] = calibrated[i]
                    dataout2 = np.column_stack((newx, calibrated))
                    saveAS2 = fil + 'IntCal%i.txt' % n
                    np.savetxt(saveAS2, dataout2)
                    datout3 = np.column_stack((newx, lampy))
                    saveAS3 = meas +'Track%i.txt' % n
                    np.savetxt(saveAS3, datout3)
#             print(n)
############################################################################ PLOTTING
#         import matplotlib.pyplot as plt
#         import matplotlib.gridspec as gridspec
#         from math import log10, floor

        def round_to_1(x):
            return round(x, -int(floor(log10(x))))

        if (IntensityCalibrate == False):
            im = zip(*d)
            im.pop(0)
            ok=np.array(im)
        if (IntensityCalibrate == True):
            im = zip(*dcal)
            im.pop(0)
            ok=np.array(im)
        #print(ok)
        dx = ok.sum(axis=0)
        dy = ok.sum(axis=1)
        hei = [k*(13.3/len(dy)) for k in range(1,len(dy)+1)]
        plt.figure(w00)
```

```
302         gs = gridspec.GridSpec(2, 2, width_ratios=[1,3], height_ratios
    =[3,1])
            ax1 = plt.subplot(gs[0])
304         ax1.plot(dy, hei)
            ax1.set_xlabel('Counts')
306         ax1.set_xticks([0,round_to_1(((max(dy)-min(dy))/2)+min(dy)),
    round_to_1(max(dy))])
            ax1.ticklabel_format(style='sci', scilimits=(0,0), axis='x')
308         plt.ylim([0,max(hei)])
            ax2 = plt.subplot(gs[1])
310         cax=ax2.imshow(im, aspect='auto', origin='lower', extent=[min(
    calib),max(calib),0,13.3])


312         ax1.set_ylabel('Height on Detector (mm)')
            ax4 = plt.subplot(gs[3])
314         ax4.plot(calib, dx)
            ax4.set_ylabel('Counts')
316         ax4.set_yticks([0,round_to_1(min(dx)),round_to_1(((max(dx)-min(
    dx))/2)+min(dx)),round_to_1(max(dx))])
            ax4.ticklabel_format(style='sci', scilimits=(0,0), axis='y')
318         ax4.set_xlabel('Wavelength (nm)')
            plt.xlim([min(calib),max(calib)])
320         #plt.suptitle(fil, fontsize=20)
            plt.savefig(fil + '.png', transparent = True, bbox_inches=0)
322         #plt.show()
            print(fil)
```

D.2 Analysis of Diatomic Spectra

The output of the Python code above consists of a two column `.txt` file for each track. The first column of the file represents wavelength and the second column the intensity as measured by the detector. For our investigations concerning diatomic molecules, these files are to be fit with computed spectra representing the relevant

molecular transitions. Because each image may contain numerous tracks and an experimental run may collect spectra over a range of time delays after laser-induced optical breakdown, the fitting procedure has been developed for batch processing.

The methods used for the batch processing of multiple tracks over multiple images are very similar to those discussed in the previous appendix regarding parallel computing on the Newton High Performance Computing cluster. A FORTRAN code is used to generate user input for the Nelder-Mead fitting program, create a job definition, and submit the job definition file to the cluster for multiple tracks in an image and multiple images in an experimental data set. In fact, the codes previously used for the Monte-Carlo type error analysis are simply modified as follows.

```
      program controlax
      integer bytes
      character*15 txt
      character*16 sge
      character*12 inpfil, varfil, outfil, expfil, datfil
      character*12 fitfil, prnfil
!      character*19 resfil
      character*100 command, command2
      iseed = 1
      call gettim(ihr,im,is,ihs)
      iseed=60*im+is
      if(iseed/2*2.eq.iseed)iseed=iseed+1
      do j=1,32       !Number of experimental files
      do i=1,4        !Number of iterations
!       i=0
       if(i.gt.1051.or.j.gt.1051)Stop 'i or j too large!'
!!!!!!!!!!!!!!!!!!!!!!!!!!!!!!!!!!!!!!!!!!!!!!!!!!!!!!!!!!!
!   Prepare files
!!!!!!!!!!!!!!!!!!!!!!!!!!!!!!!!!!!!!!!!!!!!!!!!!!!!!!!!!!!
       if(j.le.9)then
         write(inpfil,10)j,'.inp'
         write(expfil,10)j,'.txt'
```

```
23              write(fitfil,10)j,'.fit'
                write(prnfil,10)j,'.prn'
25              write(sge,'("NMT",I1.1,"i0000.sge")')j
                write(varfil,10)j,'inp.0000'
27              write(datfil,10)j,'dat.0000'
                write(outfil,10)j,'out.0000'
29 !             write(resfil,'("TempResults",I1.1,".txt")') j
            elseif(j.ge.10.and.j.le.99)then
31              write(inpfil,101)j,'.inp'
                write(expfil,101)j,'.txt'
33              write(fitfil,101)j,'.fit'
                write(prnfil,101)j,'.prn'
35              write(sge,'("NMT",I2.2,"i0000.sge")')j
                write(varfil,101)j,'inp.0000'
37              write(datfil,101)j,'dat.0000'
                write(outfil,101)j,'out.0000'
39 !             write(resfil,'("TempResults",I2.2,".txt")')j
            elseif(j.ge.100.and.j.le.999)then
41              write(inpfil,1001)j,'.inp'
                write(expfil,1001)j,'.txt'
43              write(fitfil,1001)j,'.fit'
                write(prnfil,1001)j,'.prn'
45              write(sge,'("NMT",I3.3,"i0000.sge")')j
                write(varfil,1001)j,'inp.0000'
47              write(datfil,1001)j,'dat.0000'
                write(outfil,1001)j,'out.0000'
49 !             write(resfil,'("TempResults",I3.3,".txt")')j
            else
51              write(inpfil,1002)j,'.inp'
                write(expfil,1002)j,'.txt'
53              write(fitfil,1002)j,'.fit'
                write(prnfil,1002)j,'.prn'
55              write(sge,'("NMT",I4.4,"i0000.sge")')j
                write(varfil,1002)j,'inp.0000'
```

```
57              write(datfil,1002)j,'dat.0000'
                write(outfil,1002)j,'out.0000'
59  !            write(resfil,'("TempResults",I4.4,".txt")')j
            endif
61          if(j.le.9)then
              write(datfil(6:9),'(I4.4)')i
63            write(varfil(6:9),'(I4.4)')i
              write(outfil(6:9),'(I4.4)')i
65            write(sge(6:9),'(I4.4)')i
            elseif(j.ge.10.and.j.le.99)then
67            write(datfil(7:10),'(I4.4)')i
              write(varfil(7:10),'(I4.4)')i
69            write(outfil(7:10),'(I4.4)')i
              write(sge(7:10),'(I4.4)')i
71          elseif(j.ge.100.and.j.le.999)then
              write(datfil(8:11),'(I4.4)')i
73            write(varfil(8:11),'(I4.4)')i
              write(outfil(8:11),'(I4.4)')i
75            write(sge(8:11),'(I4.4)')i
            else
77            write(datfil(9:12),'(I4.4)')i
              write(varfil(9:12),'(I4.4)')i
79            write(outfil(9:12),'(I4.4)')i
              write(sge(9:12),'(I4.4)')i
81          endif
!!!!!!!!!!!!!!!!!!!!!!!!!!!!!!!!!!!!!!!!!!!!!!!!!!!!!!!!!!!!!!!!!!!!!!!!
83          open(1,file=inpfil)
!            open(2,file=varfil)
85  !        open(4,file=expfil)
!            open(5,file=datfil)
87          open(7,file='GUI.inp')
 10         format(I1,a)
89  101     format(I2,a)
 1001       format(I3,a)
```

```
 1002     format(I4,a)
!!!!!!!!!!!!!!!!!!!!!!!!!!!!!!!!!!!!!!!!!!!!!!!!!!!!!!!!!!!!!!!!!!!!!!!
!  Rewrite the GUI.inp file
!!!!!!!!!!!!!!!!!!!!!!!!!!!!!!!!!!!!!!!!!!!!!!!!!!!!!!!!!!!!!!!!!!!!!!!
!          read(7,'(a)')ex
!          write(1,'(a)')expfil
!           don=1,6
!                 read(7,'(a)')txt
!                 write(1,'(a)')txt
!           enddo
!          read(7,'(a)')fit
!          write(1,'(a)')fitfil
!          read(7,'(a)')prn
!          write(1,'(a)')prnfil
!           dom=1,11
!                 read(7,'(a)')txt
!                 write(1,'(a)')txt
!           enddo
!!!!!!!!!!!!!!!!!!!!!!!!!!!!!!!!!!!!!!!!!!!!!!!!!!!!!!!!!!!!!!!!!!!!!!!!
!  Adjust Initial Temperature
!!!!!!!!!!!!!!!!!!!!!!!!!!!!!!!!!!!!!!!!!!!!!!!!!!!!!!!!!!!!!!!!!!!!!!!!
          read(7,'(a)')ex
          write(1,'(a)')expfil
           don=1,6
                 read(7,'(a)')txt
                 write(1,'(a)')txt
           enddo
          read(7,'(a)')fit
          write(1,'(a)')fitfil
          read(7,'(a)')prn
          write(1,'(a)')prnfil
           dom=1,8
                 read(7,'(a)')txt
                 write(1,'(a)')txt
```

```
125             enddo
               read(7,*)T
127            Temp=T+(1000*i)
               write(1,*)Temp
129             dok=1,2
                     read(7,'(a)')txt
131                  write(1,'(a)')txt
                enddo
133 !!!!!!!!!!!!!!!!!!!!!!!!!!!!!!!!!!!!!!!!!!!!!!!!!!!!!!!!!!!!!!!!!!!!!!!
!  Add noise to the experimental file
135 !!!!!!!!!!!!!!!!!!!!!!!!!!!!!!!!!!!!!!!!!!!!!!!!!!!!!!!!!!!!!!!!!!!!!!!
!           don=1,1024                              !Loop to
137 !           rx=ran(iseed)                         !generate
!           read(4,*)x,y                            !noise
139 !           write(5,*)x,y*(1.+(2.*rx-1.)*0.25)
!           enddo
141 !           write(2,'(a)')datfil      !Write to input file
!           read(1,'(a)')txt            !Read 1st line
143 !           don=1,19   !NO EXCLUSION="1,19": EXCLUSION="1,22"
!                read(1,'(a)')txt       !Loop to
145 !                write(2,'(a)')txt     !creat noise
!           enddo                       !input file
147 !!!!!!!!!!!!!!!!!!!!!!!!!!!!!!!!!!!!!!!!!!!!!!!!!!!!!!!!!!!!!!!!!!!!!!!
!  Randomly adjust the assumed background for NMT
149 !!!!!!!!!!!!!!!!!!!!!!!!!!!!!!!!!!!!!!!!!!!!!!!!!!!!!!!!!!!!!!!!!!!!!!!
!           don=1,13  !NO EXCLUSION="1,13": EXCLUSION="1,16"
151 !                read(1,'(a)')txt
!                write(2,'(a)')txt
153 !           enddo
!          read(1,*)bkg
155 !          bkgout=bkg*(1.+(2.*ran(iseed)-1.)*0.25)
!          write(*,*)bkgout
157 !          write(2,*)bkgout
!           dom=1,6
```

```
!                read(1,'(a)')txt
!                write(2,'(a)')txt
!             enddo
!!!!!!!!!!!!!!!!!!!!!!!!!!!!!!!!!!!!!!!!!!!!!!!!!!!!!!!!!!!!!!!!!!!!!!!
          close(1)
!          close(2)
!          close(4)
!          close(5)
          close(7)
!!!!!!!!!!!!!!!!!!!!!!!!!!!!!!!!!!!!!!!!!!!!!!!!!!!!!!!!!!!!!!!!!!!!!!!
!   Make a description file for qsub
!!!!!!!!!!!!!!!!!!!!!!!!!!!!!!!!!!!!!!!!!!!!!!!!!!!!!!!!!!!!!!!!!!!!!!!
          open(3,file=sge)
          write(3,'("#$ -N Job",a16)') sge
          write(3,'(a12)')'#$ -q short*'
          write(3,'(a7)')'#$ -cwd'
          write(3,'(a10)')'#$ -o null'
          write(3,'(a10)')'#$ -e null'
          write(3,'(4a)')'mpirun ./NelderMead.mpi <',inpfil,' >',outfil
          close(3)
!!!!!!!!!!!!!!!!!!!!!!!!!!!!!!!!!!!!!!!!!!!!!!!!!!!!!!!!!!!!!!!!!!!!!!!
          write(command,'(3a)')'qsub ',sge
          call system(command)    !Submit description file
         enddo
!!!!!!!!!!!!!!!!!!!!!!!!!!!!!!!!!!!!!!!!!!!!!!!!!!!!!!!!!!!!!!!!!!!!!!!
!         call system(' qstat >Queue')    !Check completion
!         inquire(file='Queue', size=bytes)
!         do while(bytes.ne.0)             !Wait until
!           call system(' qstat >Queue')  !job is finished
!           inquire(file='Queue', size=bytes)
!         enddo
!!!!!!!!!!!!!!!!!!!!!!!!!!!!!!!!!!!!!!!!!!!!!!!!!!!!!!!!!!!!!!!!!!!!!!!
!         write(command2,'(3a)')'cat F*.dat >> ',resfil
!         write(command2,'(a)')'cat F*.dat >> TempResults.txt'
```

```
193 !         call system(command2) !Put TempResults into a file
    !         call system(' rm F*.dat') !Remove individual TempResults
195         enddo
            end
```

When compared to the code developed for the purposes of error analysis using a Nelder-Mead fitting routine to infer parameters by comparing computed to experimental spectra, the above code is a bit more simplistic. The code for error analysis repeatedly submits a single data set multiple times, while arbitrarily adjusting already determined best fitting parameters within a specified range. The error analysis code will then move on to the next data set and repeat the procedure. In contrast, the code for analyzing multi-track images creates only one set of input commands for each track to be submitted to the fitting algorithm. The parameter values used as input to initialize the Nelder-Mead routine represent the experimentalist's educated guess rather than the result of previous fitting. The code can be further modified to submit multiple educated guesses, one after the other. Since the Nelder-Mead fitting routine is susceptible to returning local minima as results, this additional procedure is beneficial.

D.3 Analysis of Atomic Spectra

Typically, our analysis of atomic transition lines in spectra consists of measuring the intensity along with the Stark width of each transition line of interest. The intensities of multiple atomic lines contained in a single spectrum can be used in a Boltzmann plot method to infer the temperature of the plasma, while the Stark widths are used to infer the electron density. In some instances, the Stark shift of an atomic line may be measured by analyzing spectra collected within the first hundred nanoseconds after the laser event.

If the collected spectra contain atomic transition lines of interest, the analysis is typically performed by a series of two Python programs. The first program serves to

determine and subtract the baseline of each track of an image. For each track, the second program will attempt to fit a Lorentzian profile to the observed atomic line shapes.

The code for the initial program requires the user to provide the wavelength ranges where each atomic line shape should be found. The program will then narrow the range for each transition line by determining where the wings of the observed line shape are no longer discernible from the spectral baseline. This process is aided by the use of a Savitzky-Golay or low-pass filter. The filter allows for spectral transitions to become more distinguishable in the presence of a noisy baseline. The low-pass filter also serves to provide a baseline to be subtracted from the experimental data. A linear interpolation is used to represent this baseline over the spectral regions where the program determines the atomic line shapes to be. Below is an example code for this procedure.

```
# -*- coding: utf-8 -*-
"""
Created on Thu Mar 08 14:30:24 2012

@author: Woods
"""
from scipy import *
import numpy as np
import matplotlib.pyplot as plt
from scipy import interpolate

for n in range(1, 129):
    expfile = 'Ti_240-5_200scan_200ns_6gateIntCal%i.txt' %n
    #fitfile = 'f159pt.txt'
    #rotfile = 'f00136pts2rot(1).fit'
    #vibfile = 'VibFitTable3.txt'

    x, y = loadtxt(str(expfile), unpack=True)
    #fitx, fity = loadtxt(str(fitfile), unpack=True)
```

```
    #rotx, roty = loadtxt(str(rotfile), unpack=True)
    #vibx, viby = loadtxt(str(vibfile), unpack=True)
    wl_min = min(x)
    wl_max = max(x)
    maximum = max(y)
    minimum = min(y)
############################################################ DEFINE SG FILTER
    def savitzky_golay(y, window_size, order, deriv=0):

        try:
            window_size = np.abs(np.int(window_size))
            order = np.abs(np.int(order))
        except ValueError, msg:
            raise ValueError("window_size and order have to be of type
    int")
        if window_size % 2 != 1 or window_size < 1:
            raise TypeError("window_size size must be a positive odd
    number")
        if window_size < order + 2:
            raise TypeError("window_size is too small for the
    polynomials order")
        order_range = range(order+1)
        half_window = (window_size -1) // 2
# precompute coefficients
        b = np.mat([[k**i for i in order_range] for k in range(-
    half_window, half_window+1)])
        m = np.linalg.pinv(b).A[deriv]
# pad the signal at the extremes with
# values taken from the signal itself
        firstvals = y[0] - np.abs( y[1:half_window+1][::-1] - y[0] )
        lastvals = y[-1] + np.abs(y[-half_window-1:-1][::-1] - y[-1])
        y = np.concatenate((firstvals, y, lastvals))
        return np.convolve( m, y, mode='valid')
```

```
    ysg = savitzky_golay(y, window_size=31, order=1)
#     sub = y - ysg
    datx     = [None] *len(x)
    daty     = [None] *len(x)
    j = 0
################################################ REGIONS TO APPLY SG FILTER
    for i in range(len(x)):
        if (i>0 and i<136):
            datx[j] = x[i]
            daty[j] = ysg[i]
            j = j+1
        if (i>291 and i<362):
            datx[j] = x[i]
            daty[j] = ysg[i]
            j = j+1
        if (i>466 and i<626):
            datx[j] = x[i]
            daty[j] = ysg[i]
            j = j+1
        if (i>719 and i<723):
            datx[j] = x[i]
            daty[j] = ysg[i]
            j = j+1
        if (i>747 and i<820):
            datx[j] = x[i]
            daty[j] = ysg[i]
            j = j+1
        if (i>863 and i<878):
            datx[j] = x[i]
            daty[j] = ysg[i]
            j = j+1
        if (i>935 and i<1024):
            datx[j] = x[i]
            daty[j] = ysg[i]
```

```
84              j = j+1
    datx = filter(None,datx)
86  daty = filter(None,daty)
    #print(x)
88  #exclude = set(range(240.5, 242))
    #[n for n in datx if n not in exclude]
90  tck = interpolate.splrep(datx,daty,k=1)
    ynew = interpolate.splev(x,tck,der=0)
92  dax  = [None] *len(x)
    day  = [None] *len(x)
94  jj=0
    for i in range(len(x)):
96      if (i>0 and i<20):
            dax[jj] = x[i]
98          day[jj] = ysg[i]
            jj = jj+1
100     if (i>953):
            dax[jj] = x[i]
102         day[jj] = ysg[i]
            jj = jj+1
104 dax = filter(None,dax)
    day = filter(None,day)
106 yck = interpolate.splrep(dax,day,k=1)
    new = interpolate.splev(x,yck,der=0)
108 ############################################################ FIND HEIGHT OF PEAKS
    sub = y - ynew
110 #h1 = max(sub[137:291])
    h2 = max(sub[362:466])
112 h3 = max(sub[626:719])
    h4 = max(sub[723:747])
114 h5 = max(sub[820:863])
    h6 = max(sub[878:935])
116 #print(h1)
    ############################################################## COMPARE HEIGHTS
```

```
    subsg = savitzky_golay(sub, window_size=31, order=6)
    #print(subsg)
    #q1 = max(subsg[137:291])
    q2 = max(subsg[362:466])
    q3 = max(subsg[626:719])
    q4 = max(subsg[723:747])
    q5 = max(subsg[820:863])
    q6 = max(subsg[878:935])
    #d1 = h1-q1
    d2 = h2-q2
    d3 = h3-q3
    d4 = h4-q4
    d5 = h5-q5
    d6 = h6-q6
    #print(d1)
    print(d2)
    print(d3)
    print(d4)
    print(d5)
    print(d6)
########################################################## MAKE LINE AT FWHM
    #l1     = [None] *len(subsg[137:291])
    l2     = [None] *len(subsg[362:466])
    l3     = [None] *len(subsg[626:719])
    l4     = [None] *len(subsg[723:747])
    l5     = [None] *len(subsg[820:863])
    l6     = [None] *len(subsg[878:935])
    #x1     = [None] *len(subsg[137:291])
    x2     = [None] *len(subsg[362:466])
    x3     = [None] *len(subsg[626:719])
    x4     = [None] *len(subsg[723:747])
    x5     = [None] *len(subsg[820:863])
    x6     = [None] *len(subsg[878:935])
    a=0
```

```
    b=0
    c=0
    d=0
    e=0
    f=0
    for i in range(len(x)):
        #if (i>137 and i<291):
            #if (subsg[i] >= .5*h1):
                #l1[a] = .5 * h1
                #x1[a] = x[i]
                #a = a + 1
        if (i>362 and i<466):
            if (subsg[i] >= .5*h2):
                l2[b] = .5 * h2
                x2[b] = x[i]
                b = b + 1
        if (i>626 and i<719):
            if (subsg[i] >= .5*h3):
                l3[c] = .5 * h3
                x3[c] = x[i]
                c = c + 1
        if (i>723 and i<747):
            if (subsg[i] >= .5*h4):
                l4[d] = .5 * h4
                x4[d] = x[i]
                d = d + 1
        if (i>820 and i<863):
            if (subsg[i] >= .5*h5):
                l5[e] = .5 * h5
                x5[e] = x[i]
                e = e + 1
        if (i>878 and i<935):
            if (subsg[i] >= .5*h6):
                l6[f] = .5 * h6
```

```
                x6[f] = x[i]
                f = f + 1
    #l1 = filter(None,l1)
    l2 = filter(None,l2)
    l3 = filter(None,l3)
    l4 = filter(None,l4)
    l5 = filter(None,l5)
    l6 = filter(None,l6)
    #x1 = filter(None,x1)
    x2 = filter(None,x2)
    x3 = filter(None,x3)
    x4 = filter(None,x4)
    x5 = filter(None,x5)
    x6 = filter(None,x6)

    #if x1:
        #w1 = x1[-1]-x1[0]
    if x2:
        w2 = x2[-1]-x2[0]
    if x3:
        w3 = x3[-1]-x3[0]
    if x4:
        w4 = x4[-1]-x4[0]
    if x5:
        w5 = x5[-1]-x5[0]
    if x6:
        w6 = x6[-1]-x6[0]
    #dataout = column_stack((x2,l2))
    #savetxt('%iwidth.txt' %n, dataout)
##########################################################################PLOT
    plt.figure(n)
    plt.plot(x, y, 'k', lw=1.5, label='Original signal')
    plt.plot(x, ysg, 'g', lw=1.75, label='Filtered')
    plt.plot(x, new, 'r', label='Baseline')
```

```
    plt.plot(x, sub, label='Baseline Subtracted')
    #plt.plot(x[50:1000], subsg, '-', label='Filtered')
    #if x1:
        #plt.plot(x1, l1, label=r'$\omega_{1}$ = %.4f nm' %w1)
    if x2:
        plt.plot(x2, l2, label=r'$\omega_{2}$ = %.4f nm' %w2)
    if x3:
        plt.plot(x3, l3, label=r'$\omega_{3}$ = %.4f nm' %w3)
    if x4:
        plt.plot(x4, l4, label=r'$\omega_{4}$ = %.4f nm' %w4)
    if x5:
        plt.plot(x5, l5, label=r'$\omega_{5}$ = %.4f nm' %w5)
    if x6:
        plt.plot(x6, l6, label=r'$\omega_{6}$ = %.4f nm' %w6)
    plt.xlabel('Wavelength (nm)', fontsize=12)
    plt.ylabel('Relative Intensity', fontsize=12)
    plt.xlim([wl_min, wl_max])
    plt.legend(loc='best', fancybox=True)
    leg = plt.legend(loc='best', fancybox=True)
    leg.get_frame().set_alpha(0.5)
    #plt.show()
    plt.savefig('%iFWHM.png' %n, transparent = True, bbox_inches=0)
    dataout = column_stack((x,new))
    subtract = column_stack((x,sub))
    savetxt('%iBase.txt' %n, dataout)
    savetxt('%iSub.txt' %n, subtract)
```

The output of the program will be a `.txt` file for each track containing the background subtracted data along with a `.txt` file containing the assumed background that was subtracted from the original signal. The program also produces a plot of the original signal along side the assumed background and the background subtracted data. Figure D.2 displays a characteristic plot produced by the program.

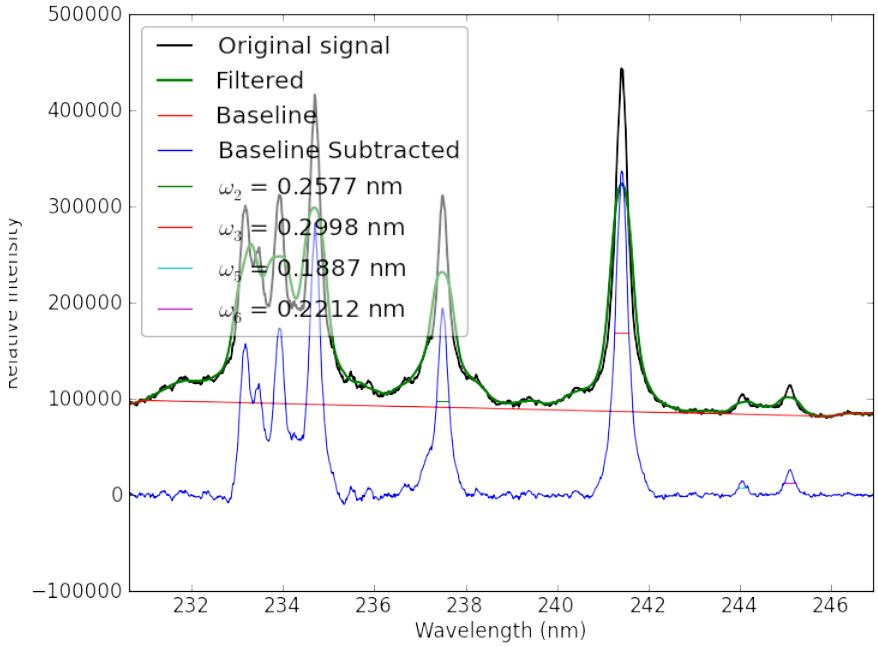

Figure D.2: An example of the resulting plot from the first of two Python programs for analyzing atomic spectral line shapes. The figure represents experimentally obtained Ti III and Ti II lines corresponding to Figure 4.13.

The second program uses the `.txt` file containing the background subtracted data as input. Within the code, the user must again specify the regions where the line shapes are located. When executed, the program will attempt to fit a Lorentzian profile to the data contained in each specified region. The output of the program provides a `.txt` file containing the FWHM and integrated intensity of each Lorentzian along with a plot of the Lorentzian profiles superposed to the background subtracted spectrum for each track of an image.

The integrated intensities of the resulting `.txt` file will then be used to infer temperature by the Boltzmann plot method or Saha-Boltzmann plot method, while the FWHM measurements will be used to infer electron density. As seen in Figure D.3, the program does quite well to fit every atomic line in a spectrum. The spectrum of Fig. D.3 illustrates a typical challenge, as the lines often contribute to one another. The delay time of the measurement was specifically chosen in order to detect both the

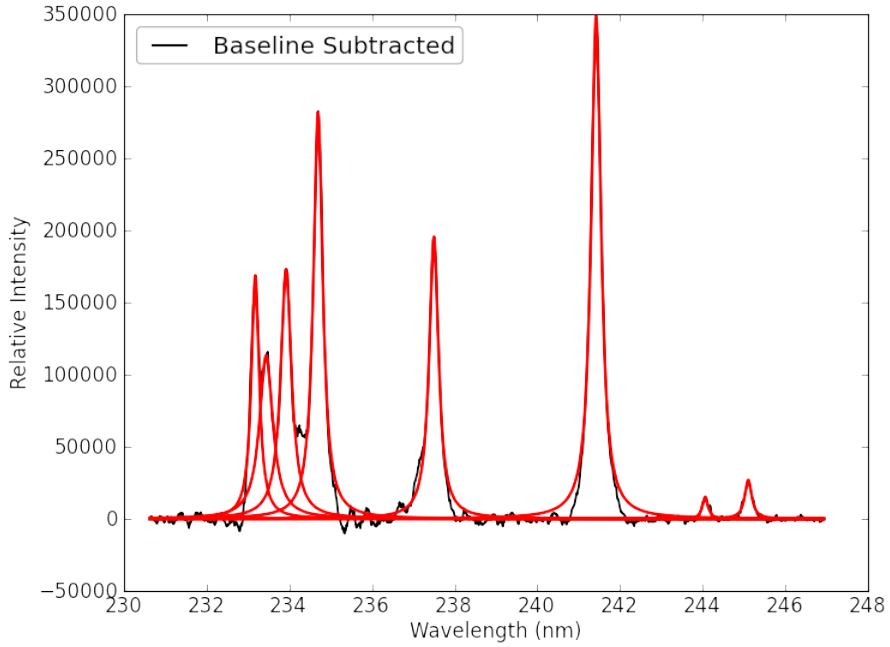

Figure D.3: An example of the plot resulting from the second of two Python programs for analyzing atomic spectral line shapes. This plot corresponds to the same data as the previous Figure D.2.

Ti III and Ti II species. Even though the Lorentzian fitting routine successfully fit both species, a Boltzmann plot method is used rather than the Saha-Boltzmann method for the data analysis. Below is an example of the code used to fit the Lorentzian profiles to the spectral line shapes.

```
1  # -*- coding: utf-8 -*-
   """
3  Created on Tue Dec 17 23:19:58 2013

5  @author: woods
   """
7


9  ############################################### IMPORTING REQUIRED MODULES

11 import numpy as np
```

```
from scipy import *
from scipy.integrate import quad
from scipy.optimize import leastsq # Levenberg-Marquadt Algorithm #
import matplotlib.pyplot as plt

################################################################ LOADING DATA
for n in range(1, 129):
    expfile = '%iSub.txt' %n
    a = np.loadtxt(expfile)
    x = a[:,0]
    y = a[:,1]
    fil = expfile[:-4]

########################################################## DEFINING FUNCTIONS

    def lorentzian(x,p):
        numerator =  (p[0]**2 )
        denominator = ( x - (p[1]) )**2 + p[0]**2
        y = p[2]*(numerator/denominator)
        return y

    def residuals(p,y,x):
        err = y - lorentzian(x,p)
        return err

##################################################### BACKGROUND SUBTRACTION

# defining the 'background' part of the spectrum #
#ind_bg_low = (x > min(x)) & (x < 450.0)
#ind_bg_high = (x > 590.0) & (x < max(x))

#x_bg = numpy.concatenate((x[ind_bg_low],x[ind_bg_high]))
#y_bg = numpy.concatenate((y[ind_bg_low],y[ind_bg_high]))
#pylab.plot(x_bg,y_bg)
```

```
47 # fitting the background to a line #
   #m, c = numpy.polyfit(x_bg, y_bg, 1)
49
   # removing fitted background #
51 #background = m*x + c
   #y_bg_corr = y - background
53 #pylab.plot(x,y_bg_corr)

55 ########################################################################## FITTING DATA

57 # initial values #
       p = [0.5,233.166,12e3]  # [hwhm, peak center, intensity] #
59     f = lambda x: p[2]*((p[0]**2 )/(( x - (p[1]) )**2 + p[0]**2))


61
       pbest1 = leastsq(residuals,p,args=(y[120:167],x[120:167]),
      full_output=1)
63     best_parameters1 = pbest1[0]
   #print(best_parameters)
65     p = best_parameters1

67     fit1 = lorentzian(x,best_parameters1)
       integral1, error1 = quad(f, x[0], x[1023])
69     print "area =", integral1

71     p = [0.5,233.434,12e3]  # [hwhm, peak center, intensity] #
       f = lambda x: p[2]*((p[0]**2 )/(( x - (p[1]) )**2 + p[0]**2))
73     pbest2 = leastsq(residuals,p,args=(y[169:187],x[169:187]),
      full_output=1)
       best_parameters2 = pbest2[0]
75 #print(best_parameters)
       p = best_parameters2
77
```

```
    fit2 = lorentzian(x,best_parameters2)
    integral2, error2 = quad(f, x[0], x[1023])
    print "area =", integral2

    p = [0.5,233.9,12e3]  # [hwhm, peak center, intensity] #
    f = lambda x: p[2]*((p[0]**2 )/(( x - (p[1]) )**2 + p[0]**2))
    pbest3 = leastsq(residuals,p,args=(y[190:225],x[190:225]),
    full_output=1)
    best_parameters3 = pbest3[0]
#print(best_parameters)
    p = best_parameters3

    fit3 = lorentzian(x,best_parameters3)
    integral3, error3 = quad(f, x[0], x[1023])
    print "area =", integral3

# optimization #
    p = [0.5,234.6786,12e3]
    pbest4 = leastsq(residuals,p,args=(y[229:291],x[229:291]),
    full_output=1)
    best_parameters4 = pbest4[0]
#print(best_parameters)
    p = best_parameters4

# fit to data #
    fit4 = lorentzian(x,best_parameters4)
    integral4, error4 = quad(f, x[0], x[1023])
    print "area =", integral4

    p = [0.5,237.4986,12e3]
    pbest5 = leastsq(residuals,p,args=(y[362:466],x[362:466]),
    full_output=1)
    best_parameters5 = pbest5[0]
#print(best_parameters)
```

```
109     p = best_parameters5

111     fit5 = lorentzian(x,best_parameters5)
        integral5, error5 = quad(f, x[0], x[1023])
113     print "area =", integral5

115     p = [0.5,241.3989,12e3]  # [hwhm, peak center, intensity] #
        f = lambda x: p[2]*((p[0]**2 )/(( x - (p[1]) )**2 + p[0]**2))
117     pbest6 = leastsq(residuals,p,args=(y[626:719],x[626:719]),
        full_output=1)
        best_parameters6 = pbest6[0]
119 #print(best_parameters)
        p = best_parameters6
121

        fit6 = lorentzian(x,best_parameters6)
123     integral6, error6 = quad(f, x[0], x[1023])
        print "area =", integral6
125

        p = [0.5,244.01647,12e6]  # [hwhm, peak center, intensity] #
127     f = lambda x: p[2]*((p[0]**2 )/(( x - (p[1]) )**2 + p[0]**2))
        pbest7 = leastsq(residuals,p,args=(y[820:863],x[820:863]),
        full_output=1)
129     best_parameters7 = pbest7[0]
    #print(best_parameters)
131     p = best_parameters7

133     fit7 = lorentzian(x,best_parameters7)
        integral7, error7 = quad(f, x[0], x[1023])
135     print "area =", integral7

137     p = [0.5,245.04347,12e6]  # [hwhm, peak center, intensity] #
        f = lambda x: p[2]*((p[0]**2 )/(( x - (p[1]) )**2 + p[0]**2))
139     pbest8 = leastsq(residuals,p,args=(y[878:935],x[878:935]),
        full_output=1)
```

```
    best_parameters8 = pbest8[0]
#print(best_parameters)
    p = best_parameters8

    fit8 = lorentzian(x,best_parameters8)
    integral8, error8 = quad(f, x[0], x[1023])
    print "area =", integral8

    if (n == 1):
        w = open('TiAreas.txt', 'w')
        w.write('%i      %.3f      %.3f      %.3f      %.3f      %.3f      %.3
    f      %.3f      %.3f \n' % (n, integral1, integral2, integral3,
    integral4, integral5, integral6, integral7, integral8))
        w.close()
    else:
        w = open('TiAreas.txt', 'a')
        w.write('%i      %.3f      %.3f      %.3f      %.3f      %.3f      %.3
    f      %.3f      %.3f \n' % (n, integral1, integral2, integral3,
    integral4, integral5, integral6, integral7, integral8))
        w.close()
################################################################ PLOTTING

    plt.figure(n)
    plt.plot(x, y, 'k', lw=1.5, label='Baseline Subtracted')
    plt.plot(x,fit1,'r-',lw=2)
    plt.plot(x,fit2,'r-',lw=2)
    plt.plot(x,fit3,'r-',lw=2)
    plt.plot(x,fit4,'r-',lw=2)
    plt.plot(x,fit5,'r-',lw=2)
    plt.plot(x,fit6,'r-',lw=2)
    plt.plot(x,fit7,'r-',lw=2)
    plt.plot(x,fit8,'r-',lw=2)
    plt.xlabel('Wavelength (nm)', fontsize=12)
    plt.ylabel('Relative Intensity', fontsize=12)
```

```
#     plt.xlim([wl_min, wl_max])
    plt.legend(loc='best', fancybox=True)
    leg = plt.legend(loc='best', fancybox=True)
    leg.get_frame().set_alpha(0.5)
    #plt.show()
    plt.savefig('%iLor.png' %n, transparent = True, bbox_inches=0)
    dataout1 = column_stack((x,fit1))
    savetxt(fil + 'lor1.txt', dataout1)
    dataout2 = column_stack((x,fit2))
    savetxt(fil + 'lor2.txt', dataout2)
    dataout3 = column_stack((x,fit3))
    savetxt(fil + 'lor3.txt', dataout3)
    dataout4 = column_stack((x,fit4))
    savetxt(fil + 'lor4.txt', dataout4)
    dataout5 = column_stack((x,fit5))
    savetxt(fil + 'lor5.txt', dataout5)
    dataout6 = column_stack((x,fit6))
    savetxt(fil + 'lor6.txt', dataout6)
    dataout7 = column_stack((x,fit7))
    savetxt(fil + 'lor7.txt', dataout7)
    dataout8 = column_stack((x,fit8))
    savetxt(fil + 'lor8.txt', dataout8)
```

Appendix E

Python NMT

A crucial tool for this research is the Nelder-Mead fitting program used to infer microplasma parameters from experimentally obtained data. The program represents tables of line-strengths for a given diatomic molecular transition as a spectrum by assuming various parameters such as temperature, intensity, and resolution. This spectrum, generated according to computed line strengths, is then fit to an experimentally obtained spectrum by means of a Nelder-Mead simplex routine. This routine provides a nonlinear, multi-parameter fitting method, allowing for one or more best-fitting parameters to be obtained.

The version of this fitting program most widely used at the University of Tennessee Space Institute is developed by James Hornkohl. The program, entitled NMT, has been coded in various languages such as Visual Basic and FORTRAN. While producing consistent fitting results, different program versions offer unique features such as a graphical user interface, real-time visualization of the fit by means of plot, and various different forms of output for fitting results. In this research, preference was given to the FORTRAN rendition. While lacking a stunning GUI and real-time visualizations, the FORTRAN version is presumably the fastest. It also is the most readily adaptable for both Windows and Linux operating systems, which makes it attractive for use on many computing clusters.

However optimized the FORTRAN version may allow itself to become, sometimes a nice GUI and real-time fitting are well worth the extra computing time. For instance, in many cases of purely speculative analysis, a user might want to run the fitting program repeatedly, each time changing maybe just one parameter based on the outcome of the previous result. In which case, the ability to change only one input cell in a program window before clicking the "Run" button would be quite useful when compared to repetitively typing all of the input into command line.

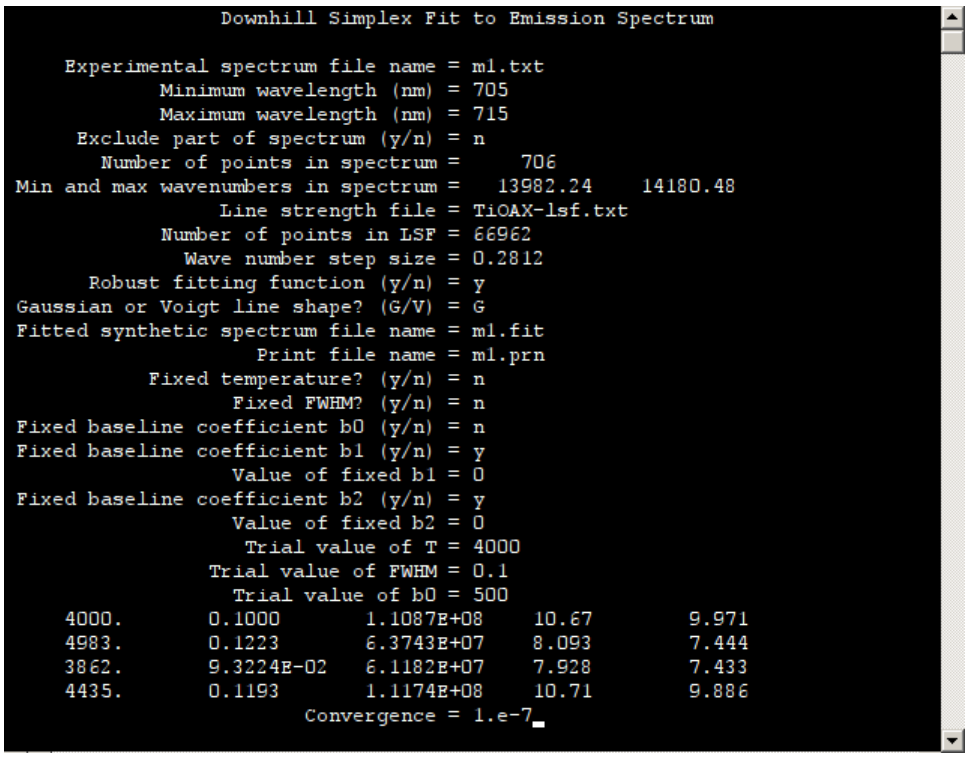

Figure E.1: Example of user input for the NMT program designed in FORTRAN

With these features in mind, I decided to rewrite the NMT program offering a GUI, using a language that would be compatible with both Windows and Linux. At the time, I was splitting my time between coding in java and coding in Python. Python was chosen due to my familiarity creating a graphical user interface with the language. Also, there are readily available Python libraries such as SciPy which offer a wide selection of built in functions such as a Nelder-Mead fitting routine. However, it became clear that in order to decrease the runtime and overall size of the program,

it would be ideal to use Python libraries such as SciPy sparingly. Even with this revision, the code I created was proving to be prohibitively slow.

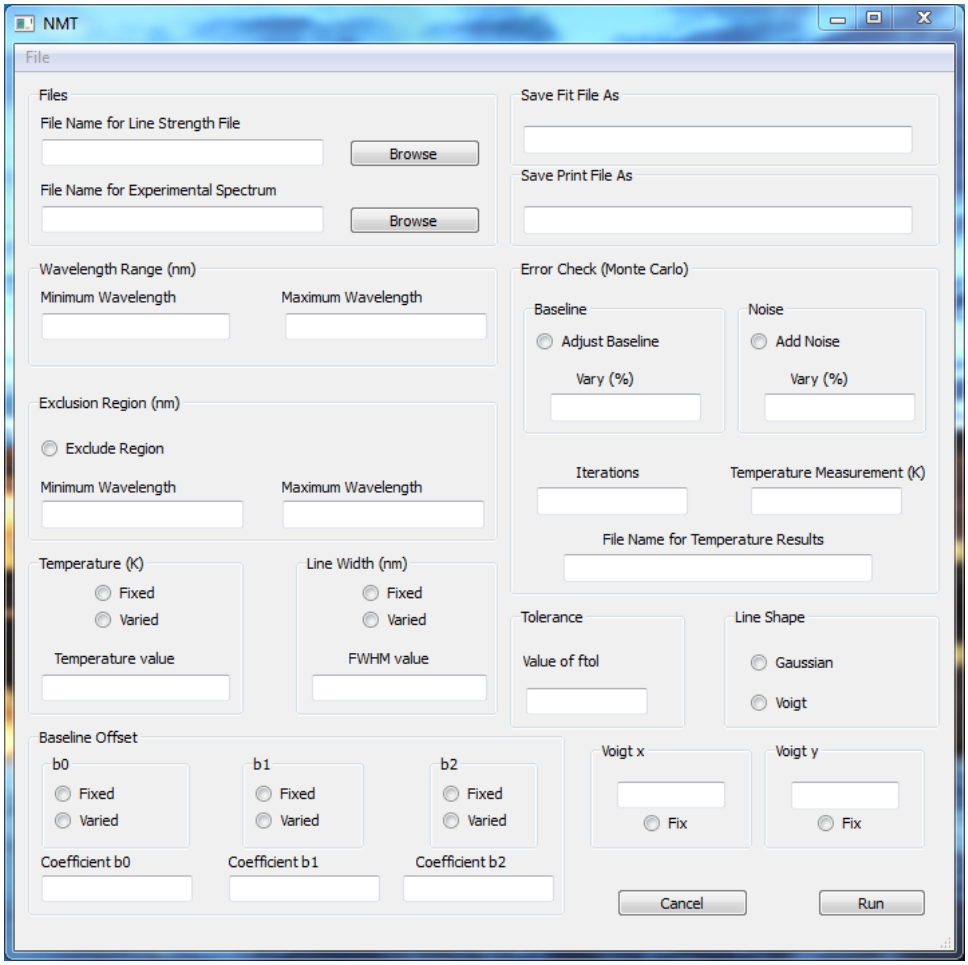

Figure E.2: The graphical user interface for the NMT program designed in Python

While the initial attempt at creating a Python version of the NMT program was disappointing, there was a simple solution. The interface I created using Python would serve to generate user input and call the original FORTRAN version. Due to the differing terminology for calling a program in Windows and Linux, two different version of the code would have to be written, but the only difference would be the system commands used to call the NMT program.

Since the Python program serves only to get input from the user and call the original FORTRAN program, with only minor additions the program was constructed

to run in a Monte-Carlo like manor, meaning that the program could be iteratively executed with randomly varied user input. The program then serves not only as a tool for inferring micro-plasma parameters, but also as a tool for error analysis, as outlined in Appendix A.

Vita

Alexander Woods was born in Nashville, TN, to the parents of Larry and Elizabeth Woods. He has one older sister, Michelle Woods. He attended Sylvan Park Elementary School then Meigs Magnet School before attending Father Ryan High School. After graduating from Father Ryan, Alexander attended California State Polytechnic University in San Luis Obispo, CA, and began studying Aerospace Engineering. During his first year of college, he realized he was much more interested in the fundamental science aspects of his course work and decided to major in Physics closer to home, at the University of Tennessee in Knoxville. He earned his Bachelor of Science degree from the University of Tennessee in December of 2008, with a major in Physics and minors in Mathematics and Astronomy. In the Fall of 2009, he accepted a teaching assistantship as a Physics graduate student at the University of Tennessee. In August of 2011, he earned his Master of Science degree, concentrating in Atomic, Molecular, Optical, and Low-temperature Physics with a minor concentration in Aerospace Engineering. At that time, Alexander accepted a graduate research assistantship at the Center for Laser Applications on the campus of the University of Tennessee Space Institute in Tullahoma, TN. In February of 2015, Alexander will marry the love of his life, Bailey Strickland.